Dijet Photoproduction At High Transverse Energies with the ZEUS detector at HERA

Andreas H. Ochs

Department of Physics
McGill University, Montreal
July 2002

A thesis submitted to the Faculty of Graduate Studies and Research in partial fulfillment of the requirements for the degree of Doctor of Philosophy

Abstract

Photoproduction events in ep collisions with photon virtuality Q^2, the negative squared four-momentum of the exchanged photon, less than 1 GeV^2, and at least two jets of high transverse energy have been studied in the photon and proton center-of-mass range $W_{\gamma p}$ of 134< $W_{\gamma p}$ <277 GeV with the ZEUS detector at HERA. The data sample was collected during the 1996 and 1997 running periods with an integrated luminosity of 38.7 pb^{-1} allowing for a precise measurement of differential cross sections in a kinematic regime unreachable for experiments at current e^+e^- colliders. For the determination of these differential cross sections, both jets were required to have a transverse energy larger than 11 GeV with at least one having more than 14 GeV. Differential hadron cross sections were extracted for these dijet events using separate resolved and direct enhanced subsamples. The cross sections have been compared to NLO QCD calculations using several different parametrisations of the photon structure functions within these calculations. The achieved sensitivity of the data at the photon structure functions allows to test the validity of the used parametrisations of the photon structure functions. This test shows the need for improvements of those parametrisations in the kinematical range under investigation. The extracted data at low x_γ^{OBS} constrains the parton densities in the photon which can be exploited in future parametrisations of the photonic parton densities.

Résumé

Les processus de photoproduction ayant au moins deux jets de grande impulsion transverse sont étudiés à l'aide du détecteur ZEUS à HERA. L'espace de phase décrit par $Q^2 <$ 1 GeV^2 et 134 < W_{γ_p} <277 GeV est étudié. L'ensemble de données, recueilli entre 1996 et 1997, correspond à une luminosité intégrée de 38.7 pb^{-1}. Ces données permettent de mesurer des sections efficaces différentielles dans un régime cinématique inaccessible aux collisionneurs e^+e^-. Ces sections efficaces sont mesurées à l'aide d'événements pour lesquels chaque jet a une impulsion transverse supérieure à 11 GeV et dont au moins un a une impulsion transverse supérieure à 14 GeV. Les sections efficaces hadroniques sont extraites pour une classe d'événements choisis correspondant principalement soit au processus direct soit au processus résolu. Les résultats sont comparés à des prédictions QCD-NLO utilisant différentes paramétrisations de la structure du photon.

Contents

Acknowledgements

Many people have contributed to the production of these thesis in many ways; to those not mentioned individually by name I apologise.

I am deeply grateful to my supervisor Prof. François Corriveau for his guidance and support throughout the whole period of my studies at Montreal and at DESY, Hamburg. I am grateful to Dr. Matthew Wing for his endless help and patience in the completion of this thesis. I want to thank the members of the QCD working group, particularly the member of the High E_T subgroup Prof. Juan Terron, Prof. Jon Butterworth, once more Matthew Wing and Eileen Heaphy, for interesting discussions and suggestions during the development of this analysis. I want to thank all members of the Canadian High Energy Physics group at ZEUS which have been great colleagues and friends, especially my old flat mates Raphael Galea and Ali Sabet-Fakhri.

Chapter 1

Theoretical Overview of the Strong Interaction and Photoproduction

1.1 Historical Review

To use scattering of particles for the investigation of the structure of matter has a long history. In 1913 Frank and Hertz [1] used electron scattering on gases to show the discrete energy level structure of the gas atoms. In 1953, Hofstadter et al. [2] scattered electrons on nucleons to examine the internal structure of the proton and the neutron. The measured values for the electric and magnetic elastic form factors as a function of the momentum transfer deviated from the expectations assuming point-like nucleons.

The results were consistent with a diffuse nucleon structure with an estimated radius of 0.8 fm. In 1961 Gell-Mann and Ne'eman set up a model to classify the abundance of hadrons, which had been discovered in the 1960's, into multiplets. Hadrons of the same spin and parity were classified according to their charge and strangeness with an underlying SU(3) symmetry group named isospin. In 1964 Gell-Mann [3] and Zweig [4] independently showed that all known hadrons could be explained as states made of three fractionally charged spin-$\frac{1}{2}$ particles, named quarks (by Gell-Mann) as a fundamental representation of the SU(3) symmetry group. The symmetry had to be broken to explain the mass splitting of hadrons belonging to the same irreducible representation. The discovery of the Ω particle [5] with the quantum number as predicted was a first success

for the quark model while introducing a new puzzle. Being a spin-$\frac{3}{2}$ particle and having a quark content of three quarks of the same flavour, the wave function is symmetric under exchange of two quarks, thus violating the Pauli exclusion principle for fermions. The model was rescued by introducing a new quantum number which is assumed to obey an exact SU(3) symmetry. The new quantum number, colour, acts as a new charge similarly to the electric charge in electromagnetism, but with three instead of two fundamental states named red, blue and green. As for Quantum Electrodynamics (QED), being the dynamical quantum field theory of electromagnetism with the electrical charge as the source of the force field, the new quantum number, colour, can be taken as the source of a new quantum field. The formulation of this idea led to the introduction of Quantum Chromodynamics [6] (QCD) which after more than 25 years is firmly believed to be the theory of the strong interactions. In the following section a short review of the basic general features of QCD is given, followed by an overview of the application of QCD to processes at the Hadron Electron Ring Accelerator (HERA), the electron proton collider located at Hamburg, Germany at which the measurements for this thesis have been performed.

1.2 Basic Features of Quantum Chromodynamics

Quantum Chromodynamics is the quantum field theory of the strong interaction describing the interaction between the coloured quarks via the exchange of coloured bosons named gluons. Like QED, QCD is a gauge theory. While QED is based on an abelian U(1) symmetry, the underlying symmetry of QCD is a non-abelian SU(3) causing significant differences in the theory when compared to the QED case. One of these differences is the behaviour in the change of the coupling constant of the theory, α_s, as a function of the momentum involved in the process under consideration. The coupling constant of an interaction is related to its strength. While the fine structure constant, $\alpha_{em}(\mu^2)$, increases with higher momentum values from 1/137 at a momentum scale of $\mu^2 \approx 0$ GeV^2 to about 1/128 at a momentum scale of the Z^0 rest mass, the strong coupling constant has the opposite behaviour. In lowest order the running of the coupling constant α_s is given by

$$\alpha_s\left(\mu^2\right) = \frac{12\pi}{(33 - 2N_f)\ln\frac{\mu^2}{\Lambda^2_{QCD}}} \tag{1.1}$$

where N_f is the number of active quark flavour at this scale, μ^2 is the renormalisation scale usually taken as the momentum scale being probed and Λ_{QCD} is a free parameter of QCD which has to be determined experimentally. The formula shows that the standard techniques in quantum field theory based on perturbation theory will only work in the regime of high energies (or short distances) where $\mu^2 \gg \Lambda_{QCD}$. At longer distances the perturbative approach breaks down. The physical picture behind this is expressed in terms of charge screening. The vacuum polarisation caused by an electron leads to the fact that the effective charge of the probed electron and hence the effective coupling increases when shorter and shorter distances are probed. In case of QCD this is replaced by an anti-screening effect. The reasons are additional graphs in the calculation. These additional terms originate from the assumed SU(3) symmetry, causing the coupling of the gluon to gluons. Carrying the colour quantum number, gluons are not only the exchange boson of the strong interaction force but also act themselves as sources of the field. The resulting anti-screening is referred to as asymptotic freedom. It is only in this asymptotic limit that perturbative QCD calculations hold and the quarks can be treated as quasi-free particles within the calculations of scattering processes. The increase of the coupling constant at the low momentum scale and the breakdown of the perturbation technique at the scale Λ_{QCD} is believed to be the reason that quarks cannot be seen as free particles but are bound within hadrons. This property is called confinement.

The use of perturbation theory results in a truncated series of the quantity considered. The divergences arising during this calculations have to be regularised in a consistent way resulting in the introduction of a free parameter μ, called renormalisation scale. Various schemes for this regularisation exist. The fundamental theorem of renormalisation states that physical quantities, if calculated to all orders in perturbative QCD, are independent of the renormalisation scheme used. Nevertheless the truncated series do depend on the renormalisation scheme. Usually the scale is chosen to be of the order of the energy taking part in the process.

Since perturbative QCD (pQCD) can only be performed at high momentum transfer, it seems at first sight impossible to perform any calculation involving quarks, which are bound inside hadrons, since this introduces non-perturbative, long-range physics. It is the factorisation theorem which states that any cross section can be factorised as a convolution of partonic cross sections calculated in pQCD with functions containing the non-calculable information about the parton distribution within the hadrons. The term parton historically was introduced to name the constituents which form the proton before their exact nature was known. The parton distribution functions inside the hadron incorporate the physics below the factorisation scale. It is common to choose in general cases the same scale for both factorisation and renormalisation.

The final state partons as used within these cross section calculations are not the detected particles. The transition of the scattered partons to the observed hadrons is a non-perturbative process labeled hadronisation, which cannot be calculated from first principles. Several phenomenologically based hadronisation models exist, the description of those used in this analysis will be given in chapter 4. A strong correlation exists between the scattered partons and the hadrons originating from the scattering process, as experimentally found, since most of the produced hadrons seem to go about the direction of their initiating parton. It was found that if the initial scattered parton was of high energy and transverse momentum, a pronounced stream of hadrons can be found around the axis of motion of the parton. These streams of hadrons are called jets. The analysis of jet production played a major role in the confirmation of QCD as the theory of the strong interactions. It was for example the analysis of the angular distribution of three-jet production at the electron positron collider PETRA which proved the existence and the spin of the gluons [7].

1.3 QCD at HERA

The basic process in lowest order at HERA for ep scattering is mediated by the exchange of a photon, γ or Z^0, called neutral current, or by the exchange of $W^\pm$, called charged

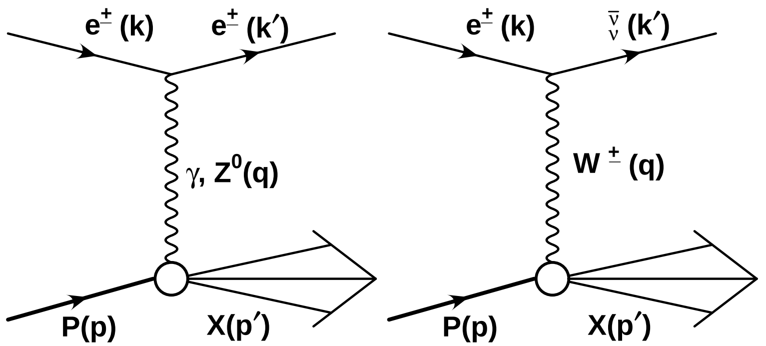

Figure 1.1: *Leading order deep inelastic scattering processes. On the left side, neutral current and on the right side, charged current diagram. Given in brackets are the four-momenta. X stands for any hadronic final state system.*

current. Figure 1.1 shows the leading order diagrams with the nomenclature for the momenta used in the following. The commonly used variables to describe the kinematics of the scattering are the following. The negative squared four-momentum transfer Q^2, also referred to as the virtuality of the exchanged photon, is given by

$$Q^2 = -q^2 = -(k - k')^2. \tag{1.2}$$

The relative energy transfer y, commonly called elasticity, from electron to proton as seen in the rest frame of the proton is

$$y = \frac{p \cdot q}{p \cdot k}. \tag{1.3}$$

The fractional momentum x of the proton carried by the scattering particle taking part in the interaction as seen in the limit of infinite momentum of the proton, where transverse momenta are neglected, is

$$x = \frac{Q^2}{2p \cdot q}. \tag{1.4}$$

For both variables, y and x, the range of possible values is between zero and one. The value 0 for the variable y corresponds to an elastic scattering of the electron, for higher values the process is called inelastic scattering.

Using the fixed value for the center-of-mass energy $\sqrt{s}$ of the initial electron proton system

$$s = (p + k)^2 = M^2_{proton} + M^2_{electron} + \frac{Q^2}{x \cdot y} \approx \frac{Q^2}{x \cdot y}, \tag{1.5}$$

where in the last step the masses have been neglected. The kinematics can therefore be described using any two of the three variables Q^2, x and y. In the calculation of the differential ep cross section, the above diagrams contribute differently depending on the Q^2 range under investigation. The photon propagator, which is proportional to $1/Q^2$, enhances the cross section for photon exchange at low Q^2. In contrast, the propagator for the Z^0 and $W^\pm$, with masses of 91 GeV and 80 GeV respectively, are proportional to $Q^2/(Q^2 + M^2)^2$ where M^2 is the squared mass of the boson under consideration. Hence it is only for large Q^2 that contributions from these diagrams start to become as important as contributions from the photon exchange diagram. Since the Z^0 and $W^\pm$ contributions originating from the electroweak interactions are not important for this thesis, they will not be considered any further in the text. Events where the momentum transfer Q^2 is large compared to the QCD parameter Λ_{QCD}, which is in the order of 100 to 300 MeV, are referred to as deep inelastic scattering (DIS) events. Historically, it was in the regime of deep inelastic scattering that so much about the strong interaction was learned and concepts which led to the formulation of QCD were formed.

1.3.1 Deep Inelastic Scattering

The generalised differential cross section for $ep \to eX$ based only on the photon exchange diagram also depends on the nature of the proton. In an approach by Feynman [8], the proton is assumed to consist of quasi-free particles named partons. This approach is today justified by the asymptotic freedom in QCD. The cross section is then calculated as an incoherent sum of the individual electron parton diagrams. Depending on the assumed spin of these partons, the calculated differential cross section as a function of the scattering angle has a different angle dependence. From comparison of these differential cross sections to experimental data, the spin-$\frac{1}{2}$ nature of the partons taking part in the interaction was concluded. Identifying these partons with the quarks proposed by Gell-

Mann led to the quark-parton model. The cross section can be written as

$$\frac{d\sigma^{ep}}{dQ^2dx} = \frac{4\pi\alpha^2}{Q^4}\left(1-y+\frac{y^2}{2}\right)\cdot\sum_q e_q^2 f_q^p\left(x,Q^2\right) \tag{1.6}$$

where $f_q^p(x,Q^2)$ is defined as the probability to find a parton of type q inside the proton with fractional momentum x at the probed scale Q^2 of the total proton momentum, the sum running over all charged partons. The functions f_q^p are named parton density functions. Usually these are rewritten using new functions F_1 and F_2, called structure functions, which are related to the parton density functions by

$$F_2\left(x,Q^2\right) = \sum_q e_q^2 x f_q^p\left(x,Q^2\right) \tag{1.7}$$

and

$$F_1\left(x,Q^2\right) = \frac{1}{2x}F_2\left(x,Q^2\right). \tag{1.8}$$

A similar structure function F_3 exists for the proton which is only needed for the description of scattering through the exchange of Z^0 and $W^\pm$. As already mentioned these processes do not play a role in the used kinematic range. Hence F_3 will not be considered further here.

The relation in equation 1.8 is known as the Callan-Gross Relation. It is based on the assumption that the partons inside the proton are spin-$\frac{1}{2}$ point-like particles which have no transverse momentum with respect to the scattering axis. QCD processes, as described later, modify this picture, giving rise to transverse momentum for the partons involved in the scattering. Having a transverse component the partons can also interact with photons having a longitudinally polarisation. Using these functions F_1 and F_2, equation 1.6 can be transformed into

$$\frac{d\sigma^{ep}}{dQ^2dx} = \frac{4\pi\alpha^2}{xQ^4}\left(xy^2F_1\left(x,Q^2\right)+(1-y)\,F_2\left(x,Q^2\right)\right), \tag{1.9}$$

or introducing the so-called longitudinal structure function

$$F_L\left(x,Q^2\right) = F_2 - 2xF_1 = \frac{Q^2}{4\pi^2\alpha}\cdot\sigma_L, \tag{1.10}$$

which is thus related to the cross section for longitudinally polarised photons, as

$$\frac{d\sigma^{ep}}{dQ^2dx} = \frac{2\pi\alpha^2}{xQ^4}\left[\left(1+(1-y)^2\right)F_2\left(x,Q^2\right)+2\,(1-y)\,F_L\left(x,Q^2\right)\right]. \tag{1.11}$$

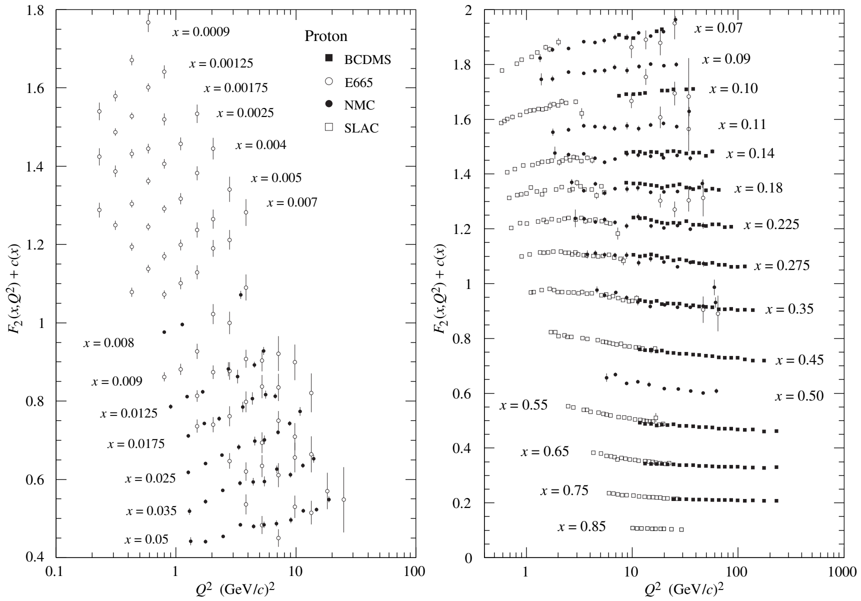

Figure 1.2: *Compilation of the proton structure function F_2^p results using data from SLAC and BCDMS, E665 and NMC shown as a function of Q^2 for bins of fixed x. Only statistical errors are shown. For the purpose of plotting, a constant $c(x) = 0.1\cdot i_x$ is added to F_2^p where i_x is the number of the x bin, ranging from 1(x = 0.05) to 14 (x=0.0009) on the left-hand figure of the picture, and from 1(x=0.85) to 15(x=0.07) on the right-hand figure. The picture is taken from [11].*

Starting from different functions $W^1(\nu,Q^2)$ and $W^2(\nu,Q^2)$, where ν is given by

$$\nu = \frac{p\cdot q}{M_{proton}}, \tag{1.12}$$

Bjorken showed [9] that in the limit of $Q^2,\nu\to\infty$ while keeping Q^2/ν fixed, the functions W^1 and W^2 become a function of only one variable x_{Bj} with the relation

$$x_{Bj} = \frac{Q^2}{2M_{proton}\nu}, \tag{1.13}$$

which corresponds to the variable x already defined above. This property of the structure functions is referred to as scaling and was shown at the Stanford Linear Accelerator (SLAC) [10] to hold in a wide range of the x, Q^2 kinematic plane. The relation between

W_1, W_2 and F_1, F_2 is

$$\nu W_2\left(\nu, Q^2\right) \equiv F_2(x) \tag{1.14}$$

and

$$M_{proton} W_1\left(\nu, Q^2\right) \equiv F_1(x)\,. \tag{1.15}$$

The experimental verification of this relation can be seen on the right hand side of figure 1.2 where measurements of the F_2 structure function are plotted as function of Q^2 for different x values used in the measurements. Looking at one of the lines in the center of the plot and taking a minimum Q^2 large enough to be in the perturbative regime (≈ 1 GeV or higher) one can see that with increasing Q^2 the value of F_2 at the given x changes at the percent level. Perfect scaling would result in a line with slope zero.

1.3.2 QCD and Quark Parton Model

Together with the obvious question of how quasi-free charged quarks bind together and form the proton, experimental violation of the proton sum rule, the probability integral over all momenta of the partons of the proton, was observed such that,

$$\sum_q \int_0^1 x f_q^p(x) dx \approx 0.5, \tag{1.16}$$

for a fixed value of Q^2 at any value of Q^2 measured, instead of the expected value of 1, which led to the discovery of neutral partons inside the proton. The neutral partons were believed to be the carrier of the strong force and named gluons. The introduction of gluons later, via the formulation of QCD, led to a modification of the naive quark-parton model. The radiation and absorption of gluons by the quarks and the splitting of gluons into gluon pairs or quark-antiquark pairs result in a transverse momentum component of the interacting quark leading to the possibility to couple to transversely and longitudinally polarised photons. Hence the Callan-Gross relation no longer holds and the longitudinal structure function deviates from zero. The presence of $q \to qg$ and $g \to gg$ and $g \to q\bar{q}$ vertices in QCD gives rise to a logarithmic violation of the scaling property of the structure functions F_1, F_2 and F_3 as function of Q^2. Again the experimental verification can be

seen in figure 1.2, this time at the left hand side. This logarithmic violation causes the F_2 values for a given x using a logarithmic scale for the Q^2 axis to lie on a line with a slope significantly larger as those seen on the right hand side of the figure. Since the dominant part for this scaling violation originates from the gluon density of the proton being only significant at low x this explains the apparent contradiction between the left and right hand side plots of figure 1.2.

The physical picture of this scaling violation can be most easily envisaged by considering the photon as a microscope with a given resolution determined by the wavelength, λ, of the exchanged photon. The wavelength is given by

$$\lambda = \frac{h}{|\vec{q}|} \tag{1.17}$$

and the photon can resolve only objects which are about the size or larger than λ. The resolution of a low Q^2 photon is hence limited and it will see only the valence quark structure of the proton. As the wavelength shrinks (as Q^2 increases), the resolving power of the photon increases and additional structure originating from the inner dynamics of the proton can be resolved. A scattering quark which carries the fractional momentum x might have originated from a $g \to q\bar{q}$ or $q \to qg$ process where the initial emitter carried a fractional momentum x' with $x' > x$. Therefore in the calculations of a process involving a quark of given momentum fraction x one must take into account the quark and gluon distributions $f(x', Q^2)$ with $x' > x$.

1.3.3 Parton Distribution Evolution

The dependence of the parton density functions of the quarks and gluons of the proton on Q^2 can be calculated using the Dokshitzer-Gribov-Lipatov-Altarelli-Parisi [12] (DGLAP) equations. These equations describe the evolution of the parton densities as function of Q^2 as originating from the splitting of a parton into two partons folded with the parton density at the given Q^2. The splitting probabilities can be derived from pQCD to any order, the leading order splitting functions are pictured in figure 1.3. The equations are

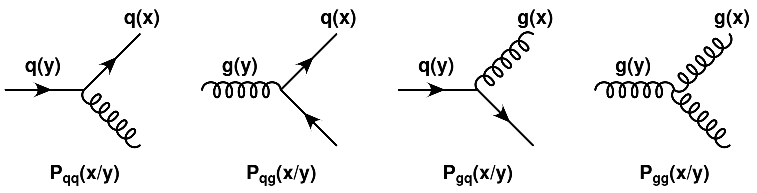

Figure 1.3: *Leading order splitting functions for the gluon and the quark.*

given by

$$\frac{dq_i\,(x,Q^2)}{d\log Q^2} = \frac{\alpha_s}{\pi}\int_x^1 \frac{dy}{y}\left[q_i(y,Q^2)P_{qq}\left(\frac{x}{y}\right)+g(y,Q^2)P_{qg}\left(\frac{x}{y}\right)\right] \quad (1.18)$$

$$\frac{dg\,(x,Q^2)}{d\log Q^2} = \frac{\alpha_s}{\pi}\int_x^1 \frac{dy}{y}\left[q_i(y,Q^2)P_{gq}\left(\frac{x}{y}\right)+g(y,Q^2)P_{gg}\left(\frac{x}{y}\right).\right] \quad (1.19)$$

where x, as already mentioned, is the fractional momentum of the parton originating in the splitting process from a parton with the fractional momentum y of the total proton momentum. The derivation of these equations is based on a leading log approximation, summing terms of the form $(\alpha_s \cdot \ln Q^2)^n$ to all orders, which give significant contributions for large Q^2 and large x. The solution of the DGLAP equations provides the evolution of the parton densities as function of Q^2. It was a major surprise at HERA to see that these equations still hold for low Q^2 and low x values [13, 14]. While the dependence of the parton distributions on Q^2 can be calculated, the initial parton distribution at the starting value Q_0^2 is not *a priori* calculable and has to be determined experimentally. Several parametrisations from different groups exist e.g. [15, 16], varying in the renormalisation scheme and basic assumptions about the used dependence on the terms in x and Q^2. All have in common that they fit their parametrisation to the existing experimental data to retrieve the values for their parton densities. Hence the differences between these sets arise more in the prediction of the parton distributions to non-measured ranges in x and Q^2. The data of this thesis lie in a kinematic range where the uncertainties coming from the proton parton distributions are minimal as will be discussed in section 2.5.2.

1.3.4 Photoproduction

The bulk of events in the measurement of the total ep cross section comes from the low Q^2 range as can be seen in equation 1.6. The interaction with an almost real photon can be thought of as a γp interaction and hence the ep interaction can be split into two parts. The first part deals with the emission of the quasi-real photon which can be calculated using basic QED diagrams. The electron beam can in this way be thought of a flux of quasi-real photons, $f_\gamma^e\,(y,Q^2)$, for a certain fractional energy, y, carried by the photon collinear to the electron beam and at a certain virtuality, Q^2. The photon flux is given by the emission probability and, taking the Equivalent Photon Approximation [89], can be written as

$$f_\gamma^e\left(y,Q^2\right) = \frac{\alpha}{2\pi Q^2}\left(\frac{1+(1-y)^2}{y} - 2\frac{1-y}{y}\frac{Q^2_{min}}{Q^2}\right) \quad (1.20)$$

where Q^2_{min} is the lowest possible virtuality and is given by

$$Q^2_{min} = m_e^2\frac{y^2}{1-y}. \quad (1.21)$$

Integrating the photon flux from the minimum Q^2_{min} to the maximum Q^2_{max} value yields the Weizsäcker-Williams Approximation [90] for the photon spectrum given by

$$f_\gamma^e\,(y) = \frac{\alpha}{2\pi}\left(\frac{1+(1-y)^2}{y}\ln\frac{Q^2_{max}}{Q^2_{min}} - 2\frac{1-y}{y}\left(1-\frac{Q^2_{min}}{Q^2_{max}}\right)\right). \quad (1.22)$$

The second part involves the calculation of the cross section for the photon-proton scattering.

In leading order (LO) QCD, the determination of the photon proton cross section for a two-parton final state is based on two contributions. While in the direct process, as pictured in figure 1.4, the direct coupling of the photon to the scattering parton of the proton is expected in QED, the resolved processes, as shown in figure 1.5, arise from the hadronic fluctuations of the photon into bound and unbound $q\bar{q}$ states as illustrated in figure 1.5. Depending on the lifetime of these fluctuations, the description of the state becomes rather complex, since due to QCD effects a complex hadronic structure can evolve. If the lifetime of the fluctuations is comparable or longer than the interaction time, the photon will not contribute as a whole but will act as a source of partons for the

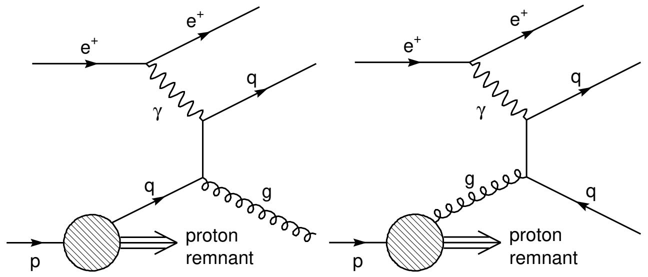

Figure 1.4: *Leading order direct processes in dijet photoproduction. The contributions differ mainly by the different propagator of the diagrams. Proton remnant refers to the debris of the proton not taking part in the interaction.*

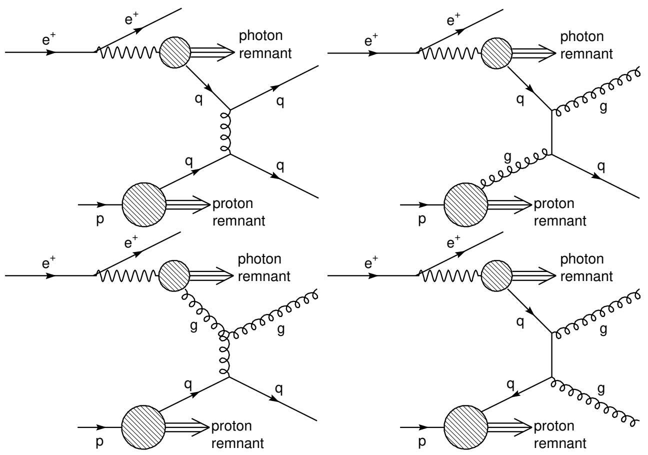

Figure 1.5: *Leading order resolved processes in dijet photoproduction. Photon remnant refers to the part of the photon not taking part in the interaction. In addition to the diagrams displayed two other processes exist, where the initial partons of the photon and proton are both gluons and the two final state partons are a quark-antiquark pair or a gluon pair.*

scattering process, hence giving rise to a hadronic component of the photon. It is only in leading order QCD that the definition of direct and resolved is unambiguous.

1.3.5 Hadronic Structure of the Photon

The fluctuation of the photon into a $q\bar{q}$ pair can proceed via the creation of a bound or an unbound state. In the first case the quantum numbers of the bound $q\bar{q}$ state have to be the same as those of the photon giving rise to the production of vector mesons, such as ρ, ω, ϕ. The small meson masses make it impossible to calculate, from first principles, the photon to vector meson fluctuations. A phenomenological model named Vector Meson Dominance Model (VDM) [17, 18] was introduced to describe this process. The photon-proton cross section in this model is given by

$$\sigma^{\gamma p}_{VDM}(W) = \sum_{V=\rho,\omega,\phi} \frac{4\pi\alpha}{f_V^2} \sigma^{Vp}(W), \tag{1.23}$$

where f_V are probability factors for the fluctuation of the photon to this meson type, W is the the mass of the photon-proton system and σ^{Vp} is the vector meson proton cross section. The lifetime of the vector meson is estimated to be

$$t_V = \frac{E_\gamma}{m_V^2 + Q^2}, \tag{1.24}$$

where E_γ is the energy of the photon and m_V the mass of the vector meson. It can be seen that the probability of the vector meson to interact with the proton increases as Q^2 approaches zero. The interaction of the vector meson with the proton can proceed in two ways, either as a soft hadron-hadron scattering with small momentum transfer or via a parton-parton interaction between a parton from the vector meson and a parton from the proton, in which case a hard scattering occurs. It is this process which provides a hard scale which can be used to perform pQCD calculations and will be used in the dijet analysis presented here.

The creation of unbound $q\bar{q}$ states with high virtuality can be calculated from first principles in QED and QCD. This contribution is referred to as the anomalous photon contribution and can be used as testing ground for pQCD calculations.

The hadronic structure of the photon as stated above can be used to introduce the concept of parton distribution functions and structure functions for the photon. These functions, $F_i^\gamma (i = 1, 2, 3)$, defined as the F_i^p in equation 1.7 and 1.8, are subject to evolution equations as in the case of the parton distribution functions of the proton, which were introduced in equation 1.18. In contrast to the proton distribution functions, however it was shown by Witten [19] in 1977 that in the asymptotic limit $Q^2 \to \infty$ where the VDM contribution plays no role, the photon parton distributions are completely determined by theory.

1.4 Status of the Photon Structure Functions

As in the case of the proton structure functions F_1, F_2 and F_3, F_1^γ can be expressed in terms of the F_2^γ structure function and F_3^γ originates from parity violating processes, which are of no importance in this analysis. Current knowledge of the photon structure function F_2^γ comes mainly from e^+e^- collider experiments studying deep inelastic $e\gamma$ scattering. A complete review of the topic of photon structure functions can be found elsewhere [20]. The structure function F_2^γ is related to the parton densities as is the case for the proton, F_2.

1.4.1 Measurements of F_2^γ from e^+e^- Experiments

The current status of F_2^γ measurements is presented in figures 1.6 and 1.7. The data shown cover the kinematic range of $Q^2 \approx 0.24$ GeV^2 up to $Q^2 \approx 706$ GeV^2 and $x_\gamma \approx 0.001$ up to $x_\gamma \approx 1$ where Q^2 is the hard scale used in the measurement and x_γ is relative fraction of momentum of the photon taking part in the interaction similar to the variable x already defined. As can be seen from figure 1.7, F_2^γ is not as well constrained for x_γ greater than 0.5. The structure function F_2^γ as measured by these experiments in deep inelastic $e\gamma$ interactions is, in leading order, only sensitive to the quark content of the photon. The gluon density which is expected to dominate the low x_γ range is not determined by these measurements. To overcome this problem, the experiments also look at $\gamma\gamma$ interactions [22, 23] where both photons are quasi-real. In the case that both photons fluctuate into a hadronic structure, the possibility of gluon-initiated resolved

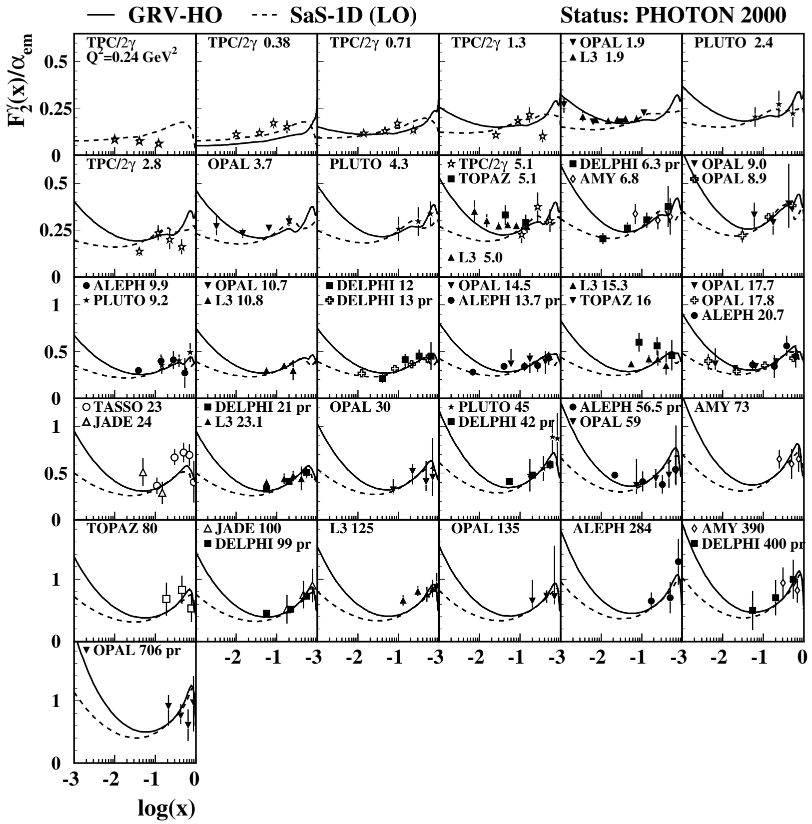

Figure 1.6: *Compilation of F_2^γ measurements as function of x_γ for different Q^2 values. The value at the top of each plot is the corresponding Q^2 value given in GeV^2. The abbreviation pr stands for preliminary data. Taken from [21].*

processes is given. In this type of event class, the gluon-initiated contribution is expected to be large, giving a possibility for a gluon distribution measurement.

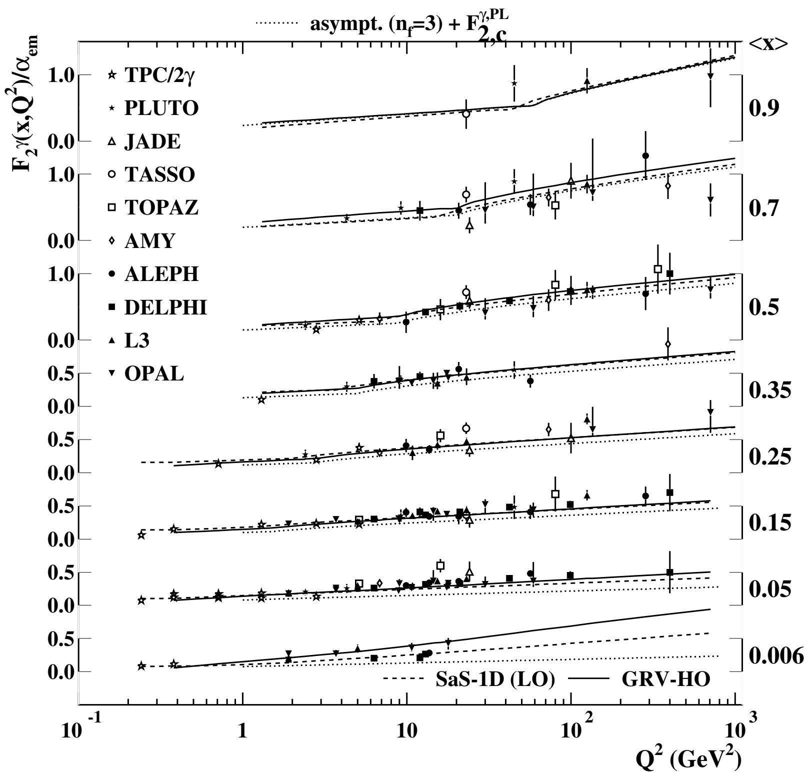

Figure 1.7: *Compilation of F_2^γ measurements as function of Q^2 for different x_γ values. Taken from [21].*

1.4.2 Photon Structure at HERA

It is the regime of two-jet or dijet production in γp scattering at HERA which has the potential to overcome this limitation on the determination of F_2^γ, being sensitive to the gluon at LO. Several publications exist, based on HERA data, which used jets or high E_T dijets in photoproduction at HERA to investigate certain features of the direct and resolved processes [24, 25, 26, 27, 28, 29]. Depending on the phase space investigated, these analysis focussed on testing pQCD or the photon structure. A short review on the

ZEUS publications will be given.

In [25] it was shown that in order to explain the transverse energy distributions, hard scattering in photoproduction was needed. This high E_T final state sample showed clear evidence for back-to-back dijet events. In addition, a subsample of these events contained energy deposits in the part of the detector which would be the direction of the electron propagation, which were consistent with Monte Carlo (MC) simulation as being a remnant of the photon due to resolved processes in $\mathcal{O}(\alpha\alpha_s)$. In [27], hard photoproduction events with center-of mass energies between 130 GeV and 250 GeV were used. The focus was the separation of the direct and resolved processes using the fractional photon momentum x_γ taking part in the hard interaction. This was used for a measurement of the $\gamma p \rightarrow X + 2\ jets$ cross section contributions of direct and resolved processes. In [28] the dijet angular cross section, $d\sigma/d|\cos\theta^*|$, in photoproduction, where θ^* is the jet scattering angle in the dijet center-of-mass system, was measured for jets of transverse energies E_T larger than 6 GeV, an invariant dijet mass, M_{JJ}, larger than 23 GeV with an average pseudorapidity $\bar{\eta}$ smaller than 0.5. The distributions, when separated into resolved and direct processes, showed a clear dependence on the propagator involved in the process. The dependences were in good agreement with Next-Leading-Order (NLO) QCD matrix element expectations. In [30], the measurement of dijet production containing a reconstructed $D^{*\pm}$ were used to investigate the charm content of the photon. Comparison of data to NLO calculations, based on massive charm calculations, showed the need to enhance the charm excitation of the photon in resolved processes. In [29], the analysis of dijet photoproduction at high-E_T using asymmetric transverse energies $E_{T,leading} > 14$ GeV and $E_{T,second} > 11$ GeV in the central detector region $-1 < \eta_{leading,second} < 2$ showed the possibility to distinguish between different photon parton distributions. A comparison of NLO theoretical predictions based on different NLO parton distribution parametrisations to corrected hadron-level cross section was performed. It was shown that an increase in statistics compared to the 1995 data set and an improvement in the understanding of the detector could make a differentiation possible. Indeed, the data sample used in this thesis corresponds to an integrated luminosity which is a factor of six higher than for the 1995 data sample.

As can be seen in figure 1.5 for the resolved processes the gluon density in the photon already contributes in LO. The cross section for resolved photoproduction is dominated at low x_γ by gluon-initiated events. The lowest x_γ values are reached for very forward going jets of low transverse momenta. The high cross section for dijet photoproduction at high x_γ at HERA allows an improved determination of F_2^γ in this kinematic regime, hence a better determination of quark densities at these high x_γ values. At HERA, higher transverse momentum jets can be reached within the dijet processes compared to the e^+e^- experiments. Since the transverse momentum of the jets is taken as the hard scale in the next-to-leading order (NLO) QCD calculations and α_s is decreasing as the scale increases, the uncertainties in the calculations for a given fixed order due to higher order terms decreases, leading to an improvement in comparison of the data to next-to-leading order (NLO) QCD calculations.

1.4.3 Parametrisations of the Photon Structure Functions

The goal of this thesis is to compare measurements of dijet photoproduction cross-sections with next-to-leading order QCD calculations using different NLO photon structure function parametrisations as input to the calculations. Up to the writing of this thesis three commonly used NLO parametrisations have been available.

1.4.3.1 The Glück, Reya and Vogt Parametrisations

The Glück, Reya and Vogt (GRV) [31, 32] parametrisation is based on the same strategy the group has used previously in the successful description of the proton and pion structure, which is to dynamically generate the parton distribution functions from an initial valence quark distribution. The parton distributions are provided in leading and next-to-leading order. The starting point of the evolution is given at a very low scale of $Q_0^2 = 0.25$ GeV^2 for the LO and $Q_0^2 = 0.35$ GeV^2 for the NLO distributions. The initial

distributions are hadron-like contributions based on the VMD model using parton distribution functions of the pion [33] based on the similarity between the ρ and the π. The anomalous contribution is taken to vanish at Q_0^2 and is created by the evolution equations. The distributions are hence taken to be $q_0^\gamma = \bar{q}_0^\gamma = \kappa \frac{4\pi\alpha}{f_\rho^2} f_\pi^q\left(x, Q_0^2\right)$ and $g_0^\gamma = \kappa \frac{4\pi\alpha}{f_\rho^2} f_\pi^g\left(x, Q_0^2\right)$ with $x f_\pi^{q,g}$ being of the form $x^b\left(1-x\right)^c$ and $b > 0$. The form factor squared f_ρ^2 is related to the probability of a $\gamma \to \rho$ transition with $1/f_\rho^2$ taken to be 2.2 [34]. The parameter κ is retrieved by fits to the data [35, 36, 37, 38, 39, 40, 41, 42, 43, 44, 45] in the kinematic range $0.71 < Q^2 < 100$ GeV^2 and incorporates the higher mass vector meson contributions. It is the only free parameter of the model, making it very predictive.

1.4.3.2 The Gordon and Storrow Parametrisations

The Gordon and Storrow GS96-HO [46, 47] parametrisation used a comparable ansatz to GRV but starting at a much higher Q_0^2 (initially at 5.3 GeV^2, now also at 3 GeV^2) for the evolution to avoid the problems related with a low scale in pQCD. At this scale, the anomalous part of the structure functions has already developed, making a more complex input to the evolution equations necessary. The photon quark distributions are given by

$$q_0^\gamma = \bar{q}_0^\gamma = \kappa \frac{4\pi\alpha}{f_\rho^2} f_\pi^q\left(x, Q_0^2\right) + q_{0,anomalous}^\gamma, \tag{1.25}$$

which is a sum of the quark distribution as in the pion and the calculable part. The masses of the light quarks, κ and the momentum fractions carried by gluons and quarks within the pion are free parameters in the fit. The data used to fit the parametrisation are published data taken from [35, 36, 37, 40, 42, 43, 44, 48, 49, 50, 51, 52, 53, 54].

1.4.3.3 The Aurenche, Fontannaz and Guillet Parametrisations

The Aurenche, Fontannaz and Guillet (AFG) parametrisation [55] uses a strategy similar to Glück, Reya and Vogt. The starting scale of the evolution is very low, $Q_0^2 = 0.5$ GeV^2, which is also obtained from the requirement of the anomalous contribution of the photon structure function to vanish at $Q^2 = Q_0^2$. The input is taken as purely hadronic-like, based on VMD arguments. The factorisation scheme used is the modified minimal subtraction scheme $\overline{MS}$. The use of this factorisation scheme is preferred due to universality and process independence of the parton distributions functions retrieved this way if an additional technical contribution is taken into account with the input distributions. The evolution is performed in the massless scheme using three flavours up to $Q^2 = 2$ GeV^2. For higher values of Q^2, four active flavours are used. An additional factor K is used to adjust the VMD contribution, with $K = 1$ in the standard parametrisation. Another parametrisation used K as a free parameter in the fit, with data taken from [35, 36, 37, 40, 42].

1.4.3.4 Comparison of Photon Structure Parametrisations

Shown in figure 1.8 are the next-to-leading NLO order parametrisations for the quark and gluon densities of the photon. Given are the parametrisations of the above mentioned groups, GRV-HO, GS96-HO and AFG-HO as function of x_γ at a factorisation scale of 225 GeV^2. This corresponds to a transverse energy of the jets of about 15 GeV, which is used in this thesis as the factorisation scale. The density are multiplied with a factor x_γ/α_{em}. The quark densities are quite similar for x_γ values below 0.5, corresponding to the regime where they are constrained by e^+e^- experiments. For the quark densities with $x_\gamma >$ 0.5 the quark parametrisations differ significantly. The gluon density parametrisations of GRV-HO and AFG-HO are quite comparable over the full x_γ range.The GS96-HO gluon parametrisation differ significantly from the GRV-HO and AFG-HO gluon parametrisations for x_γ values below ≈ 0.3. Again this is the kinematic range where the densities are not constrained by experiments.

1.5 Definition of Dijet Photoproduction Cross Sections

Using the outlined ingredients of γp scattering, proton and photon parton distributions and QCD, any cross section of $\gamma p \to cd$, where the relation from parton c, d to hadrons

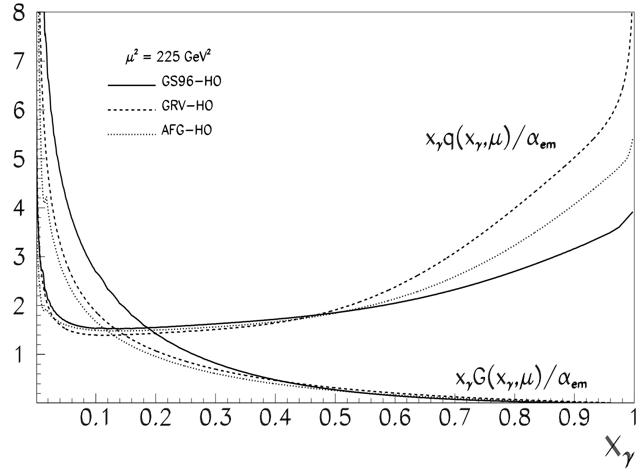

Figure 1.8: *Quark and gluon density distributions in the photon, given for three different parametrisations GS96-HO, GRV-HO and AFG-HO at a factorisation scale $\mu^2 = 225$ GeV^2. The parametrisations are given in $\overline{MS}$ factorisation scheme.*

will de defined experimentally using jets, can be expressed as

$$\begin{aligned} d\sigma_{\gamma p\to cd} &= \int_{x_p} f_{p\to b}\left(x_p,\mu^2\right)\ M_{\gamma b\to cd}\ dx_p \\ &+\sum_{ab}\int_{x_p}\int_{x_g} f_{p\to b}\left(x_p,\mu^2\right) f_{\gamma\to a}\left(x_\gamma,\mu^2\right)\ M_{ab\to cd}\ dx_\gamma dx_p, \end{aligned} \quad (1.26)$$

where the first line represents the direct and the second the resolved contribution. The functions $f_{\gamma\to a}(x_\gamma,\mu^2)$ and $f_{p\to b}(x_p,\mu^2)$ are the probabilities to find parton a in the photon or parton b in the proton with the given fractional momentum x_γ and x_p, respectively. The entities $M_{\gamma b\to cd}$ and $M_{ab\to cd}$ are the direct and resolved matrix elements from QCD calculations. Choosing a phase space of the measurement where the proton parton distributions are well measured, one uses this expression to determine the photon parton distributions.

1.6 Experimental measurement of $\gamma p \rightarrow 2$ partons

The experimental method to perform the measurement of the previously introduced cross section will use the strong correlation between the scattered partons and the detected jets: the outgoing partons will be identified by jets. To insure that the measurement is performed in a regime where the use of perturbative QCD is justified, allowing for comparisons of experimental and theoretical cross sections, a hard scale for the process is required. This is achieved using only events with jets of high transverse energies. The actual values are taken to be 14 for the first and 11 GeV for the second jet, respectively. The cross sections will be measured differentially in several variables like E_T^{jet} and x_γ to achieve a high sensitivity to the underlying physical process. Further constraints on the used events are imposed which are caused by background considerations and will hence be discussed in the appropriate chapter 6.

Chapter 2

Jets in Photoproduction

In this chapter a short introduction to the event and jet kinematic variables used in the analysis will be given. The definition of the jet algorithm will be stated and some theoretical aspects of the choice will be explained. The available NLO dijet photoproduction calculations will be shortly reviewed and the uncertainties of the comparison of data to these calculations will be discussed. The description of the measurement to be performed will be in given 2.4. A short summary of the remaining uncertainties limiting the comparison of data and theoretical calculations ends this chapter.

2.1 The Kinematic Variables

Within this thesis the kinematic variables of jets will be described using the variables as given in figure 2.1; the transverse energy, E_T^{jet}, the pseudorapidity[1], η^{jet}, and the azimuthal

[1] The pseudorapidity, $\eta = \ln(\tan(\theta/2))$ is an approximation of the rapidity y (not to be confused with the relative energy transfer y) in the limit of neglecting masses. Rapidity y is defined as $y = 1/2 \ln((E + P_z) / (E - P_z))$, where E is the energy and P_z the component of the momentum of a particle with respect to the beam axis, which is here taken to be the z-axis. The variable is of interest because the shape of the rapidity distribution dN/dy is invariant under a boost in the z-direction. For the limit of high energies rapidity becomes equivalent to the pseudorapidity where the polar angle θ is the angle of a particle with respect to the beam axis.

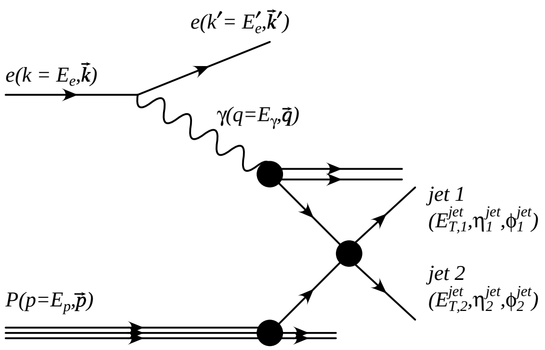

Figure 2.1: *Generic diagram of a resolved dijet photoproduction event.*

angle, ϕ^{jet}. The definition of the ZEUS coordinate system is given in section 3.2. The high momenta which are involved in the processes under study enable the masses of initial and final state particles to be neglected. The kinematics of the event will be described by Q^2 as given in equation 1.2,

$$Q^2 = -q^2 = -(k-k')^2,$$

which is the negative squared four-momentum of the photon and y as given in equation 1.3,

$$y = \frac{p \cdot q}{p \cdot k} = 1 - \frac{E'_e}{2E_e}\left(1 - \cos\left(\theta'_e\right)\right),$$

where E'_e is the energy of the scattered electron, E_e the energy of the initial electron, and θ'_e is the scattered polar electron angle as measured in the ZEUS coordinate system. Taking the limit of photoproduction with $Q^2 \rightarrow 0$ GeV^2, the scattered electron angle θ'_e approaches 180° and equation 2.1 can be rewritten as

$$y = \frac{E_e - E'_e}{E_e} = \frac{E_\gamma}{E_e}, \tag{2.1}$$

where E_γ is the energy of the exchanged quasi-real photon. In this limit of $\theta'_e \approx 180°$, the photon is collinear with the z-direction and the center-of-mass energy of the photon-proton system, $W_{\gamma p}$, can be written as

$$W_{\gamma p} = \sqrt{4E_\gamma E_p} = \sqrt{4yE_eE_p} = \sqrt{ys}, \tag{2.2}$$

with E_p being the initial proton energy and $\sqrt{s}$ the center-of-mass energy of the electron-proton system. In LO QCD the fraction of the photon energy involved in the hard scatter can be written as in [29], (for a derivation see appendix B,)

$$x_\gamma^{LO} = \frac{\sum_{partons} E_T^{parton} e^{-\eta^{parton}}}{2yE_e}, \tag{2.3}$$

which is a sum over the two final state partons. Since it is not possible to measure partons, an observable has to be introduced which is analogous to x_γ^{LO}. The definition used is

$$x_\gamma^{OBS} = \frac{\sum_{jets} E_T^{jet} e^{-\eta^{jet}}}{2yE_e}, \tag{2.4}$$

where the sum is taken over the two highest E_T^{jet} jets, assuming the already mentioned correlation between the scattered partons and the produced jets. At leading order direct photon events have $x_\gamma^{OBS} = 1$, whereas resolved processes have values $x_\gamma^{OBS} < 1$. The quantity is valid to all orders with direct events populating high x_γ^{OBS} and resolved events populating low x_γ^{OBS} being smeared due to higher order and hadronisation effects. In leading order, under the assumptions of massless partons and neglecting transverse momenta, the variable x_γ^{OBS} is therefore equivalent to the Bjorken x of the parton in the photon.

Also introduced, based on the same assumptions as above, is

$$x_p^{LO} = \frac{\sum_{partons} E_T^{parton} e^{\eta^{parton}}}{2E_p}, \tag{2.5}$$

which is the fractional energy of the proton involved in the hard scatter. The experimental approximation is similarly given by

$$x_p^{OBS} = \frac{\sum_{jets} E_T^{jet} e^{\eta^{jet}}}{2E_p}. \tag{2.6}$$

Again this is equivalent to the Bjorken x of the parton in the proton.

Dijet events can be characterised by a dijet invariant mass, which is calculated from E_T^{jet}, η^{jet} and ϕ^{jet} and the assumption of massless partons using

$$M_{jj} = \sqrt{2E_T^{jet1} E_T^{jet2}\left[\cosh(\eta^{jet1} - \eta^{jet2}) - \cos(\phi^{jet1} - \phi^{jet2})\right]}. \tag{2.7}$$

For two jets back to back in ϕ and with equal E_T^{jet} this can be approximated to be

$$M_{jj} \approx \frac{2E_T^{jet}}{\sqrt{1 - |\cos\theta^*|^2}}, \tag{2.8}$$

with $\cos\theta^*$ being the angle between the beam axis and the jets in the dijet center-of-mass system, calculated as

$$\cos\theta^* = \tanh\left(\frac{\eta^{jet1} - \eta^{jet2}}{2}\right). \tag{2.9}$$

This approximation holds for LO direct and resolved processes. Since the outgoing jets are indistinguishable only the absolute value of $\cos\theta^*$ can be determined. The variable $\cos\theta^*$ is proportional to the propagator of the process, having a angular dependence of $\propto (1-|\cos\theta^*|)^{-1}$ for processes with a quark propagator and $\propto (1-|\cos\theta^*|)^{-2}$ for processes involving a gluon propagator [56]. This feature can be used to test general features of pQCD.

2.2 The Jet Algorithm

An inherent problem of all comparisons of data to QCD calculations lies in the fact that the partons used in the calculation procedure are not the particles detected and measured. The transformation from partons to hadrons introduces transverse momenta with respect to the initial scattering axis and colour connection between the different final state partons leads to the creation of hadrons even far away from the scattering axis. Nevertheless there is a strong correlation between the hadrons seen in the detector and the underlying parton process. To reconstruct the final state parton momenta from these hadrons, a combination scheme is needed, which adds together hadrons originating from the same parton. These combination schemes are called jet algorithms and have to fulfill certain criteria to allow the comparison of measured distributions to theoretical predictions. The calculations of cross sections in pQCD at fixed order contain singularities for the emission of particles with very small energies or particles being parallel to the initial or final state partons [56]. These singularities are handled by cut-offs within these calculations. To be able to determine jets independently from the chosen cut-offs it is important that the

jet algorithm is insensitive to the variations of the final state configuration which arise from changes in these cut-offs. Also, due to the limited energy resolution and the given granularity of the detector, the experimental distinction between the different final state configurations mentioned above is impossible at the detector level. Hence a jet algorithm has to be used which obtains the same jets for a N and N+1 momenta configuration in two limits corresponding to the above mentioned singularities. The first limit is that the $(N+1)^{th}$ momentum becomes collinear to one of the other N momenta, while the second limit corresponds to the configuration where the energy of the $(N+1)^{th}$ particle tends to zero. For details about jet algorithms, see [57]. To avoid the above problems arising from the use of the common cone algorithm, the jet algorithm of choice was the so-called k_T-algorithm.

2.2.1 The k_T Algorithm

In the longitudinally invariant k_T-clustering algorithm [58], used in the inclusive mode [59], the jet combination is performed according to the following rules:

1. For each pair of objects (ij) (partons, hadrons or calorimeter cells and tracks) in the final state, a distance parameter is defined as

$$d_{ij} = \min(E_{T,i}^2, E_{T,j}^2)R_{ij}, \tag{2.10}$$

where $R_{ij}^2 = \Delta\eta_{ij}^2 + \Delta\phi_{ij}^2$ is the distance between these objects in the $\eta - \phi$ space.

2. The asymmetric beam energies cause most of the hadronic final state particles to be produced close to the beam line in the forward direction where also parts of the remnants of the initial proton can be detected. To handle this specific environment an extra beam distance parameter is introduced into the k_T-algorithm. For each object i, the distance to the beam is defined as

$$d_i = E_{T,i}^2 R^2, \tag{2.11}$$

where R is a free parameter of the jet algorithm. The parameter R was chosen to be 1 reflecting the fact that in the regions close to the beam the polar angle size of a calorimeter cells is already of this order. Hence a smaller value would not make sense. For increasing values of R the events would more and more look like single jet events.

3. From the list of all values d_{ij} and d_i the smallest value is searched. In the case where it relates the momenta k and l, the two momenta are combined and replaced by the new momenta. If the smallest value is d_k, the momentum k is removed from the list of objects and added to the list of jets.

4. The above given steps are repeated until for all momenta i: $d_i < \min(d_{ij})$.

The remaining momenta are considered as jets. When combining two momenta or energies (ij) to form a new momentum or energy k the following definitions are applied

$$E_T^k = E_T^i + E_T^j \tag{2.12}$$

$$\eta^k = \frac{\eta^i \cdot E_T^i + \eta^j \cdot E_T^j}{E_T^i + E_T^j} \tag{2.13}$$

$$\phi^k = \frac{\phi^i \cdot E_T^i + \phi^j \cdot E_T^j}{E_T^i + E_T^j}. \tag{2.14}$$

This ensures that the final jet properties E_T^{jet}, η^{jet} and ϕ^{jet} are calculated following the Snowmass convention [60]

$$E_T^{jet} = \sum_{i \in jet} E_T^i \tag{2.15}$$

$$\eta^{jet} = \frac{\sum_{i \in jet} \eta^i \cdot E_T^i}{\sum_{i \in jet} E_T^i} \tag{2.16}$$

$$\phi^{jet} = \frac{\sum_{i \in jet} \phi^i \cdot E_T^i}{\sum_{i \in jet} E_T^i}, \tag{2.17}$$

where the sum $i \in jet$ runs over all particles merged into the jet.

2.3 Next-to-leading Order Jet Calculations

Next-to-leading order QCD calculations of jet photoproduction cross sections are currently available from several different theoretical groups, M. Klasen *et al.* [61, 62], B. Harris *et al.* [63], S. Frixione *et al.* [64] and P. Aurenche *et al.* [65]. The calculations are performed up to NLO $\mathcal{O}(\alpha\alpha_s^2)$ by applying a jet algorithm to the final state partons. The renormalisation and factorisation scales within these calculations are taken to be the highest of the transverse jet energies. The parameter Λ_{QCD} is taken as the starting value of the input parton density distributions from the proton. Five quarks flavours are included in the calculations, and they are assumed to be massless. The calculations differ in the treatment of the divergences arising in fixed order expansion of the matrix elements calculations. While M. Klasen *et al.*, B. Harris *et al.* and P. Aurenche *et al.* employ the phase-space slicing method, S. Frixione *et al.* use the subtraction method. The phase-space slicing method separates non-singular from singular phase-space regions by introducing cut-off parameters used for the separation. The subtraction method cancels singularities in the calculation of cross sections by subtracting appropriate soft and collinear counter terms from the unintegrated cross sections. An investigation of the uncertainties in the prediction of theoretical cross sections due to the different approaches has been performed in [66] where agreement within 10% was found.

2.4 The Cross Section Definitions

To enable the comparison between the above mentioned next-to-leading order calculations and the measured data, the criteria for the measurements performed must be chosen in a way to minimise the uncertainties arising from non-perturbative QCD. This can be done requiring a hard scale in the process, which is provided here by the high transverse energy E_T^{jet} of the jets produced. Nevertheless non-perturbative effects might change significantly the measured cross sections compared to the initial parton cross sections due to the fragmentation process, the transformation of partons into hadrons (hadronisation) and the possibility of an underlying event. Underlying event is the name for processes where in addition to the hard scattering, soft interactions between partons of the initial state hadrons are present and hence a multiple interaction occurs. The definition of the cross section avoids these sensitivities when enforcing the conditions below, which have been developed in previous analyses [28, 29, 67, 68, 69] and in theoretical discussions [58, 61, 63, 64, 65].

The required conditions on the dijet photoproduction events for the determination of the cross sections are;

- There have to be at least two jets in the event. The transverse energies E_T^{jet} of the two highest transverse E_T^{jet} jets have to be greater than 11 GeV. It was shown in a previous analysis [67] that the experimental measured dijet cross sections agree within errors with the NLO QCD calculations under this condition, while for lower transverse energies the measured cross sections were significantly above the calculations when $x_\gamma^{OBS} < 0.75$. Comparing the required minimum E_T^{jet} with a similar analysis using $E_T^{jet} > 6$ GeV, the E_T^{jet} increase results in a harder scale suitable for pQCD calculations. In addition, the neglect of masses becomes less important.

- The phase space is selected using two different minimum E_T^{jet} values for the highest (in the following also denoted leading or first jet) and second highest transverse energy jet, $E_{T,leading} > 14$ GeV and $E_{T,second} > 11$ GeV. This is referred to as an asymmetric cut and improves the stability of NLO QCD calculations in the case that both jets just meet the minimum transverse energy criteria. A symmetric cut, if applied the same way in the theoretical calculations, would inhibit the emission of gluons from the higher order diagrams in the low transverse energy phase space, resulting in differences in the cross sections when compared to data which includes process to all order.

- The jets are defined using the longitudinally invariant k_T-clustering algorithm in the inclusive mode to avoid the problems discussed in section 2.2.

- The differential cross sections as a function of the pseudorapidity of the two highest transverse energy jets are symmetrised with respect to this variable. While in leading order processes the transverse energies of the jets are equal, in next-to-leading order the jets do not balance any more. The equality in the transverse jet energies is approached in events where one of the partons is soft. Hence the assignment of which jet is the hardest depends on the soft partons of the events and is not infrared safe.

  By symmetrisation of the cross sections in η, by interchanging the η values of the dijet system, effectively counting each event twice, this problem can be overcome [70].

- The two jets fulfilling the above criteria are required to have pseudorapidities in the range of -1 to $+2.4$. While the lower limit is due to a lack of events in the backward direction, the upper limit is dictated from the detector geometry and trigger used in this analysis and will be discussed in detail later. Using the definition of the variables x_γ^{OBS} and x_p^{OBS} given in equation 2.4 and equation 2.6 and the limits on E_T^{jet} and η^{jet} one can calculate the minimum and maximum fractional momentum at which partons of the photons and partons of the proton can be probed. The range for x_γ^{OBS} lies between $5 \cdot 10^{-2}$ and 1, while the range for x_p^{OBS} is nominally from 10^{-3} to 1. The bulk of the x_p^{OBS} is predominantly in the range from 10^{-2} to 10^{-1} as can be deduced from the definition of x_p^{OBS} given in 2.6, the fact that the cross sections fall steeply as function of increasing E_T of the jets and the used η range. In this region the parton densities of the proton are precisely measured and well constrained by measurements of the structure function F_2^p in deep inelastic ep scattering.

- The kinematic region is taken to be $Q^2 < 1$ GeV^2 and $0.20 < y < 0.85$. The limitation in the kinematic range y is caused by the DIS background as will be described in 6.3.

The dijet photoproduction cross sections determined are the differential cross section in pseudorapidity η, $d\sigma/d\eta$, the differential cross section in the highest transverse jet energy $E_T^{leading}$, $d\sigma/dE_T^{leading}$, the differential cross section in the angle determined in the dijet center-of-mass θ^*, $d\sigma/d|\cos\theta^*|$, and the differential cross section in the fractional momentum x_γ^{OBS}, $d\sigma/dx_\gamma^{OBS}$. The cross sections will be given for two separate regions in x_γ^{OBS}, a resolved enhanced sample with the requirement $0 < x_\gamma^{OBS} < 0.75$ and a direct enhanced sample with $0.75 < x_\gamma^{OBS} < 1$. The resolved enhanced sample clearly depends more strongly on the photon parton densities and can be used to study these, while the direct enhanced sample is used to test the pQCD features of the calculations.

2.5 Theoretical Uncertainties

Uncertainties in the comparison of measured cross sections to next-to-leading order predictions arise from two main sources. The first are uncertainties within the calculations itself, the second arise from the determination of corrections factors for the effects of hadronisation, which will introduce some dependence on the event generator used.

2.5.1 Intrinsic NLO Uncertainties

In performing perturbative calculations to a given order, uncertainties remain which are due to the missing higher orders. To get an estimate on the size of these contributions, the dependence of the calculated expressions on the renormalisation and factorisation scales is studied. The dependence of the cross sections on the variation of the scales within a physical meaningful range is then used to estimate the higher order contributions. The scale dependence for the presented cross sections was found to be less than 15% for a variation of the renormalisation and factorisation scales between half and twice the nominal value.

2.5.2 Parton Densities Uncertainties

The numerical NLO calculations have the parton density functions of the proton and the photon as inputs. The latter are not well constrained over the probed range of x_γ^{OBS} and are the focus of the analysis presented and so are not discussed here. In contrast, the parton density functions of the proton are well constrained from measurements of the structure function F_2^p in deep inelastic scattering. The remaining uncertainty originates from the knowledge of the gluon density of the proton. Their dependence on the calculated cross sections has been studied in [71]. Using different gluon parametrisations from the MRST group with high, central and low gluon density for the high x range (greater than 0.2) in the NLO calculations, the variations of the cross sections have been studied. It was found in all comparisons that the variations due to the choice of the gluon density

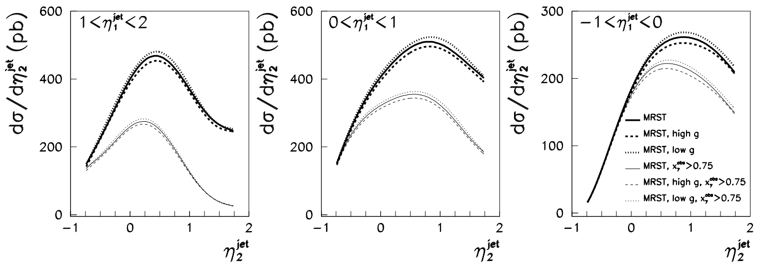

Figure 2.2: *Examples for dijet photoproduction cross sections, calculated in NLO QCD using the MRST central, high and low gluon parametrisation of the proton structure. Shown are the cross sections for the full x_γ^{OBS} range and for a region with x_γ^{OBS} > 0.75. Taken from [71].*

were less than 6 %. Figure 2.2 shows examples for the variations of the cross sections as function of the chosen parametrisation.

2.5.3 Hadronisation Uncertainties

While the NLO calculations are performed with partons, the measured cross sections will only be corrected for detector effects, hence the corrected measured cross sections are those for jets of hadrons. To close the gap between hadrons and partons, the influence on the cross sections coming from the fragmentation and hadronisation process has been studied using two different models to describe the fragmentation process. Details about the models used can be found in chapter 4. The resulting differences in the parton and hadron cross sections were found to be less than 10% in most of the kinematic regions. The only exceptions were events with one or more jets in the very backward region of this analysis ($\eta^{jet} < -0.5$), where the hadron cross sections were found to decrease by up to 40% due to fragmentation effects [66]. A comparable study was performed in [72] using a similar approach for the remaining fragmentation uncertainties.

Chapter 3

HERA and the ZEUS Detector

3.1 HERA

The Hadron Elektron Ring Anlage (HERA) is an electron[1]-proton (ep) collider located at the Deutsches Elektronen Synchrotron (DESY) site in Hamburg, Germany. A sketch of the layout of the collider is given in figure 3.1.

The HERA ring is approximately circular with a circumference of 6.34 km and a tunnel diameter of 5.6 m, located 10-25 m underground. The electron and proton beams are stored in separate synchrotron rings. Four experimental areas are distributed along the ring. In two of them (North and South Halls), housing the general purpose detectors H1 and ZEUS, the beams intersect head on. The remaining two areas (East and West Halls) are used by the fixed target experiments HERMES and HERA-B. HERMES is currently designed to examine the spin structure of the proton by scattering longitudinally polarised electrons off stationary polarised targets (hydrogen, deuterium or helium) and hence uses only the electron beam while HERA-B investigates CP violation in the $B^0\bar{B}^0$ system by scattering beam halo protons off wire targets. The nominal design values for the beam energies are 30 GeV for the electron and 820 GeV for the proton beams resulting in a center-of-mass energy of $\sqrt{s} = 314$ GeV. HERA was commissioned in 1991 with the first

[1] Unless otherwise stated the term electron refers to electrons and positrons throughout the text.

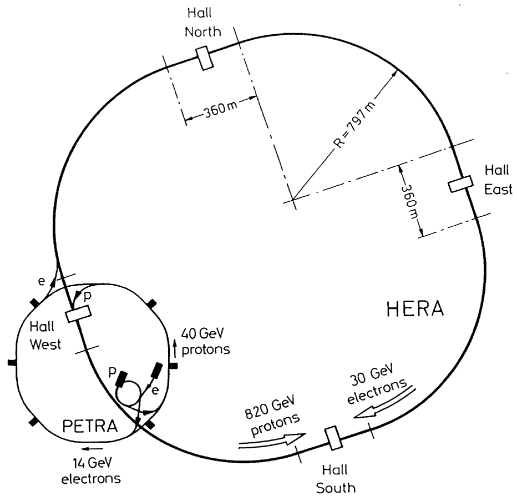

Figure 3.1: *The layout of the ep collider facility at DESY. The main collider ring, HERA, and the preaccelerator systems are shown. ZEUS is situated in the South Hall.*

ep collisions observed by ZEUS and H1 in the spring of 1992. Table 3.1 summarises the design values of HERA. After an initial period of electron-proton collisions it was decided to switch to positron-proton collision mode. This was motivated by the short lifetime and limited current of the electron beam caused by interactions with residual positively charged dust particles in the beam pipe. Starting from 1994 and up to 1997 HERA collided 820 GeV protons and 27.5 GeV positrons, yielding a center-of-mass energy $\sqrt{s} \approx 300$ GeV. In 1998, the proton beam energy was raised to 920 GeV, resulting in a center-of-mass energy of $\sqrt{s} \approx 318$ GeV .

The acceleration process of the beams is divided into several stages using older machines which already existed at DESY. Electrons from a 220 MeV and a 450 MeV linear accelerator, LINAC II and LINAC III, are injected into the DESY II synchrotron. There they are accelerated to 7.5 GeV and injected into the Positron Electron Tandem Ring Accelerator PETRA , accelerated further up to 14 GeV and then injected into HERA.

HERA Parameters	electron	proton
Nominal Energy (GeV)	30(27.5)	820(920)
Luminosity ($\mathrm{cm}^{-2}\mathrm{s}^{-1}$)	$1.5 \cdot 10^{31}$	
Circumference (m)	6336	
Magnetic Field (T)	0.165	4.65
Energy Range (GeV)	10-33	300-820(920)
Injection Energy (GeV)	14	40
Circulating Current (mA)	58	163
Number of Colliding Bunches	220	
Time between Crossings (ns)	96	
Horizontal Beam Size σ_x (mm)	0.26	0.29
Vertical Beam Size σ_y (mm)	0.07	0.07
Longitudinal Beam Size σ_z (cm)	0.8	11
z-Vertex width $\sigma_{z-Vertex}$ (cm)	6	
Filling Time (hours)	0.25	0.3
Life Time (hours)	8	100

Table 3.1: *Design values for the main HERA parameters. In parenthesis are the current values for the energies of the beams.*

Inside HERA they reach their final operating energy of 27.5 GeV. The average lifetime of the electron is about eight hours, after which the electron beam is usually dumped and refilled to achieve high luminosities. The protons start off as negatively charged hydrogen ions. Using a 50 MeV linear accelerator their electrons are stripped off and the protons are injected into a small proton synchrotron. Here they are accelerated up to 7.5 GeV before being injected into PETRA. About 70 bunches are accumulated in PETRA and accelerated to 40 GeV before being transferred to HERA where they reach their final energy of 820(920) GeV. To reach the high field strength needed to bend the proton beam, superconducting magnets are used which operate at 4 K and produce a magnetic field of

Year	$\mathcal{L}(e^-p)$ (pb^{-1})	$\mathcal{L}(e^+p)$ (pb^{-1}	E_e (GeV)	E_p (GeV)
1992	0.03	-	26.7	820
1993	1.1	-	26.7	820
1994	1.1	5.1	27.5	820
1995	-	12.3	27.5	820
1996	-	17.2	27.5	820
1997	-	36.4	27.5	820
1998	8.1	-	27.5	920
1999	17.1	28.5	27.5	920
2000	-	66.4	27.5	920

Table 3.2: *Overview of the integrated delivered luminosity by HERA from 1992 to 2000. Given are the values split into e^-p and e^+p luminosity and the used beam energies.*

4.7 T.

The particle beams in HERA consist of packets of 96 ns spaced particle bunches up to a maximum of 210 packets. Some of the electron and proton bunches are not paired. These pairs are used to monitor the rate of events caused by background due to cosmic rays and beam-gas interactions. In 1996 and 1997, 174 *ep* and 21 unpaired positron and proton bunches were used. Using the background rate as determined by these unpaired bunches one can perform a background subtraction in the experimental determination of a cross sections. For this thesis the expected beam gas background being significantly smaller than the statistical error caused no problem and hence no background subtraction was performed.

Table 3.2 summarises the lepton type and beam energies used by HERA as well as the overall performance of HERA since the startup in 1992 in terms of integrated delivered luminosity.

3.2 ZEUS Detector

The variety of possible physics processes to be studied at HERA places strong requirements on the ZEUS detector. The experiment has to be able to precisely measure and detect expected known *ep* interactions as well as enable the search for new processes by identification of the decay products of these reactions. To reconstruct physics events, accurate measurements of the energies, momenta and trajectories of the final state particles are required. The energies of the particles should be measured with an excellent resolution independent of the charge or type of particle. A fine segmentation of the apparatus is needed to provide good angular resolution. The detector should cover the whole solid angle in order to have the possibility to measure all particles of interest. The imbalance in the beam energies leads to higher particle fluxes in the direction of the proton, which also has to be considered. To fulfill these requirements, a number of different types of detector are used. The components most significant to this analysis will be discussed in more detail later. For an in-depth description of the ZEUS detector, see [73].

A view of the longitudinal cross section of the ZEUS detector is shown in figure 3.2. The origin of the right-handed ZEUS coordinate system is taken as the nominal interaction point. The positive z-axis points in the proton beam direction, the x-axis into the center of the HERA ring and the y-axis upwards. Polar angles θ are measured with respect to the proton direction and azimuthal angles ϕ with respect to the x-axis in the xy-plane.

According to the trajectory of a particle from the nominal interaction point outwards, the following detector components are traversed.

The innermost detector used to be the vertex detector taken out at the end of the 1995 data-taking period. During the shutdown for the HERA luminosity upgrade in 2000-2001 a silicon microvertex detector has been installed to improve the vertex and track finding performance. Next are the tracking devices called the central tracking detector (CTD) the forward detector and the rear tracking detector. The forward detector consists of the forward tracking detector and the transition radiation detector. During the HERA luminosity upgrade programme, the transition radiation detector has been replaced by

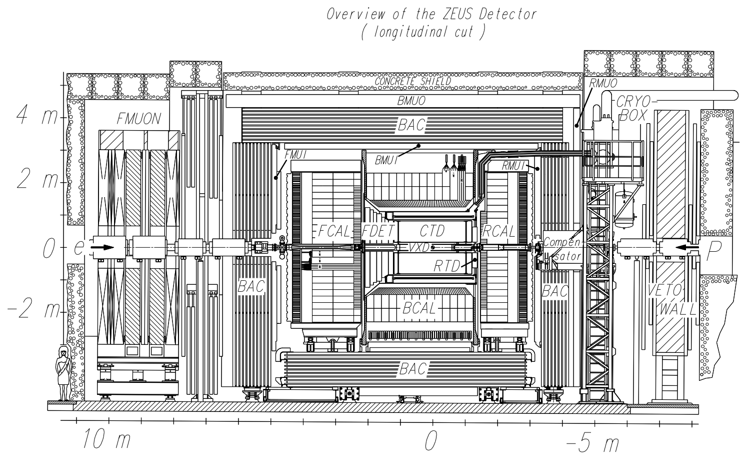

Figure 3.2: *The layout of the ZEUS detector*

a new component, the straw tube tracker. In the rear direction, the small angle rear tracking detector (SRTD) was installed to improve the position measurement for particles, particularly the scattered electron, in this direction. The tracking devices are surrounded by a superconducting solenoid magnet providing a magnetic field up to 1.8 T, currently operated at 1.4 T.

The main calorimeter, used for the measurement of particle energies, surrounds the solenoid. It is divided into forward, barrel and rear calorimeter sections (FCAL, BCAL, RCAL). Implemented in the RCAL and FCAL at a depth of 3 radiation lengths is the hadron electron separator (HES), consisting of silicon diodes. The purpose of the HES is to discriminate between electromagnetic and hadronic particles by measurement of shower profiles at a specific depth. In front of the different calorimeter sections are presampler detectors which measure shower multiplicities of particles initiated by interactions with material in front of the calorimeter. The main calorimeter is enclosed by a backing calorimeter built in the field return yoke structure.

Surrounding the calorimeter and before the iron yoke, muon identification chambers are installed. Further muon chambers surround the iron yoke. The visible asymmetry in the distribution of the detector components reflects the imbalance in the beam energies.

To detect particles emerging with very small scattering angles with respect to the beam directions, additional detectors are installed downstream of the electron and proton direction. The luminosity monitor (LUMI) and beam-pipe calorimeter are in the direction of the electron beam and measure low angle scattered electrons. The luminosity monitor additionally measures photons which are used to determine the HERA luminosity. In the opposite direction, the leading proton spectrometer and the forward neutron calorimeter measure energetic protons and neutrons, respectively. To improve the position resolution of hadronic showers two layers of scintillator strips were implemented in the forward neutron calorimeter in 1998 at a depth of 1 interaction length, replacing one lead and one scintillator layer. Additional components needed for the rejection of background events are the C5 counter (C5) and the veto wall. The C5 is located 3.15 m in negative z-direction along the beam line and measures the timing of the positron and proton bunches. The timing information of the C5 signal is used to reject beam-gas interactions produced downstream in the proton direction. The veto wall is a protective shield stopping particles in the beam halo which accompanies the proton beam from entering the main detector. In the following, only the three components, CTD, CAL and LUMI, relevant to the analysis presented in this thesis will be discussed in more detail.

3.2.1 The Central Tracking Detector

The CTD measures the trajectories and momenta of charged particles [74]. It is a cylindrical drift chamber of 205 cm in length, with an inner radius of 18.2 cm and an outer radius of 79.4 cm. A cross section view of the CTD is given in figure 3.3. It is divided into 9 layers called superlayers with further division into drift cells of eight sense wires each. The total number of sense wires is 4608 covering polar angles in the range from 15° to 164°. The odd numbered superlayers are called axial superlayers and have wires parallel to the z-axis; the even numbered superlayers are called stereo superlayers and have a small stereo angle of alternating ±5° with respect to the z-axis. The stereo angle

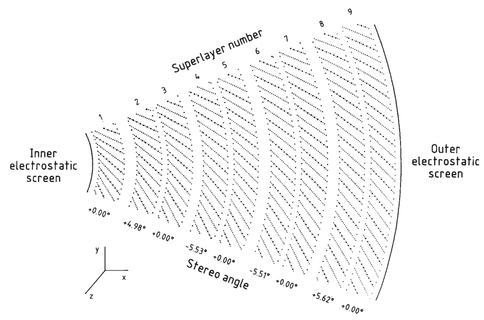

Figure 3.3: *A cross sectional view of a part of the CTD showing the wires of the different superlayers*

is chosen as such to give approximately the same resolution in polar and azimuthal angles. The stereo angle allows the measurement of the z-coordinate of tracks with a resolution of 1.4 mm. Sense wires in superlayers one, three and five are read out on both sides. The time difference of the two signals gives a fast[2] z-measurement called z-by-timing with a resolution of 3 cm which can be used to trigger events.

Charged particles penetrating the CTD ionise the gas molecules of the filled chamber. The gas composition is 85% argon, 13% carbon dioxide and 2% ethane bubbled through ethanol. The ionisation electrons drift along the electric field and collect at the sense wires resulting in a pulse which is read out at the end of the wire. Pulses exceeding a given threshold are considered hits. The hit pattern and the drift times are used to reconstruct the path of charged particles. The resolution in the hit measurement is about 230 μm in $r-\phi$. The measurement of the curvature of the tracks in the magnetic field of the solenoid can be used to determine the transverse momenta p_T of the particles, which combined with the polar angle measurement allows the determination of the particle momenta. The resolution of the transverse momentum measurement for particles of momenta greater

[2] to use the stereo z-measurement, a 3D reconstruction is needed which is only done during the reprocessing of the data offline

than 150 MeV passing all nine superlayers is

$$\frac{\sigma_{p_T}}{p_T} = 0.0065 \oplus 0.0058 p_T \oplus \frac{0.0014}{p_T}, \tag{3.1}$$

with p_T given in GeV/c. The first term is the main statistical term, the second term originates from the geometrical resolution of the hits and the last term arises from multiple Coulomb scattering.

3.2.2 The Calorimeter

To reconstruct the full event, the measurement of the energy of all particles, charged or neutral, is needed. For neutral particles and for charged particles with high transverse momenta or small polar angle (i.e. eluding the CTD), the energy measurement is performed using the calorimeter [75]. The calorimeter absorbs energy and transforms a fraction of it into light.

The energy loss in material can be classified into different types depending on the nature of the incident particle. High-energy electrons lose energy predominantly by photon radiation in the electromagnetic field of the nuclei, a process called bremsstrahlung and high-energy photons do so principally by e^+e^- pair production. The mean distance over which the initial energy of the electron falls by a factor $1/e$ by bremsstrahlung is called the radiation length X_0. The mean free path length λ^c for energetic photons before conversion is related to the radiation length X_0 with $\lambda^c = \frac{7}{9} X_0$. Through these two processes a cascade of secondary electrons and photons is initiated. Eventually the electron energies fall below the critical energy at which the cross section for ionisation becomes about the same as the bremsstrahlung cross section and the energy is then predominantly dissipated by ionisation and nuclear excitation at which point the cascade rapidly collapses. Low-energy photons lose energy predominately by the photoelectric effect with additional contributions due to Compton scattering, Rayleigh scattering and photonuclear absorption. For heavier charged particles the energy loss is primarily by ionisation and the mean rate of energy loss is given by the Bethe-Bloch equation [76].

Hadronic particles interact with the nuclei producing more secondary hadrons or causing a nuclear decay. These secondary hadrons initiate a hadronic cascade of particles with a longer longitudinal and broader transverse profile than in the electromagnetic cascade. For the typical interaction length λ the following approximation $\lambda \approx 25\ X_0$ holds for the ZEUS Calorimeter. A hadronic shower also contains an electromagnetic part mainly due to the production of π^0 mesons decaying to photons.

An important entity is the e/h ratio which is the ratio of the measured energy in the calorimeter for electrons and hadrons entering with the same initial energy. The large fluctuations in the ratio of electromagnetic to hadronic components in hadronic showers would result in a large uncertainty of the calorimeter energy measurement if this e/h ratio is not 1 or close to 1. The ZEUS calorimeter overcomes this problem by use of a compensation technique. The absorber material is depleted uranium U^{238} interleaved with hydrogenous scintillating material (SCSN-38) which samples the shower activity. Extra energy released by fast neutrons originating from fission processes of the U^{238} and neutron-proton scattering processes compensate for energy losses due to nuclear breakups. The thickness of the absorber and scintillator foils is chosen in a way to obtain equal energy response to electromagnetic and hadronic showers within 1-2%. Hence the e/h ratio is given by $e/h = 1.00 \pm 0.02$ for energies greater then 3 GeV. The relative energy resolution obtained by this compensation method is given by

$$\frac{\sigma}{E} = \frac{0.18}{\sqrt{E}} \oplus 0.01 \qquad \text{for electrons,} \tag{3.2}$$

$$\frac{\sigma}{E} = \frac{0.35}{\sqrt{E}} \oplus 0.02 \qquad \text{for hadrons,} \tag{3.3}$$

as seen in test beam measurements [77] where the energy is given in GeV. While the first term given in the equation above originates from the statistical nature of the energy deposition, the second term reflects the limit in the resolution due to the e/h ratio.

The main ZEUS calorimeter is divided into three components FCAL, BCAL and RCAL with small overlapping regions. The geometrical setup is such that it covers 99.7% of the total solid angle. The polar angle regions covered by the three components are $2.6^\circ < \theta < 39.9^\circ$ (FCAL), $36.7^\circ < \theta < 129.1^\circ$ (BCAL) and $128.1^\circ < \theta < 176.5^\circ$ (RCAL)

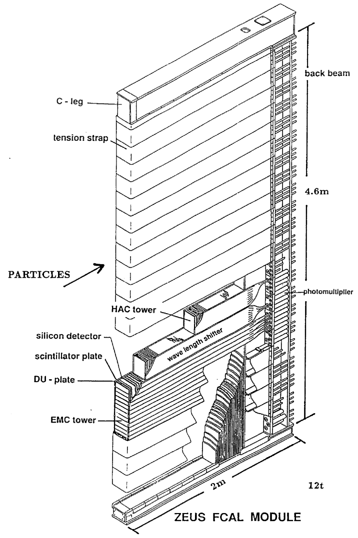

Figure 3.4: *A sketch of a FCAL module*

corresponding to pseudorapidity[3] ranges of $3.95 < \eta < 1.01$ (FCAL), $1.10 < \eta < -0.74$ (BCAL) and $-0.72 < \eta < -3.49$ (RCAL). The components are divided vertically (FCAL, RCAL) or radially (BCAL) into segments known as modules. A FCAL module is shown in figure 3.4. The F/RCAL modules are subdivided into towers with 20×20 cm^2 surface area. Each tower is longitudinal segmented into an inner electromagnetic (EMC) and two outer hadronic (HAC1/HAC2) towers. In the RCAL only one hadronic tower exists. The depth of the EMC tower is about one interaction length λ while the HAC towers are about 3-6 λ deep. The variation in the thickness of the hadronic calorimeter is governed by the expected flux of high energy particles, such that the HAC calorimeter is 6 λ in the FCAL and 3 λ in the RCAL. The position resolution in the calorimeter is determined by the area size of calorimeter cells being read out. Since electromagnetic showers are transversely very collimated, a finer granularity can be chosen. The typical cell area for an EMC cell is 5×20 cm^2. The broader hadronic showers lead to larger HAC sizes of

[3] Pseudorapidity η is defined as $\eta = -\ln\left(\tan\left(\frac{\theta}{2}\right)\right)$

20×20 cm^2. A total of 5918 cells are read out. The BCAL is set up similar to the F/RCAL but with a projective geometry. The light emerging from the scintillator travels by internal reflection to the sides of the cells where wavelength shifting light guides are connected to photomultiplier tubes (PMT) . Each cell is read out by two photomultipliers for redundancy and improved position determination. The short rise time of the PMT signal allows a good time measurement with a resolution better than 1 ns for particle energies above 4.5 GeV.

The uranium noise (UNO), the natural radioactivity from the uranium, gives a permanent current from the PMTs which is used to monitor and calibrate continuously the photomultiplier gain to a precision of about 0.2%. Using the signal integrated over 20 ms and comparing the result to test beam measurements an absolute calibration of the energy scale can be performed over the whole life time of ZEUS.

The overall design of the ZEUS calorimeter is optimised to hadronic energy measurements with the goal to get the best possible measurement of jets over the whole angular range. In contrast to this, the calorimeter design of the H1 collaboration focuses on the reconstruction of electrons and muons. The H1 main calorimeter is a liquid argon sampling calorimeter using lead plates as absorber. Its energy resolution is stated as $\sigma_e/E \sim 0.12/\sqrt{E} \oplus 0.01$ (where E is given in GeV) for electrons and $\sigma_h/E \sim 0.50/\sqrt{E} \oplus 0.02$ for hadrons. The granularity is significantly better than for the ZEUS calorimeter with typical cell area sizes of 10 cm^2 for the electromagnetic cells and 50 cm^2 for the hadronic cells. The worse resolution of the hadronic energy measurement compared to ZEUS originates in the lack of a intrinsic compensation method. H1 applies an offline shower profile based compensation algorithm to overcome part of this problem. In addition to this, the absolute calorimeter energy scale cannot be determined within the data taking environment but has to be retrieved by calibration methods which either rely on physics processes to be measured (the peak of the scattered electron energy distribution) or using external radioactive sources when the detector is not taking data.

The better energy resolution of the ZEUS calorimeter when compared to the H1 calorimeter allows for a better reconstruction of events with a high-energetic neutrino.

Due to the nature of the neutrino, these events are identified by a large amount of missing transverse momentum. Obviously a better energy resolution leads to better distinction of events with and without a high-energetic neutrino.

3.2.3 The Luminosity Measurement

The luminosity in ZEUS is measured using the electron-proton bremsstrahlung or Bethe-Heitler process $ep \to ep\gamma$ [78]. The cross section of this process is known to a high precision and is given by

$$\frac{d\sigma}{dE_\gamma} = 4\alpha_e r_e^2 \frac{E'_e}{E_\gamma E_e}\left(\frac{E_e}{E'_e} + \frac{E'_e}{E_e} - \frac{2}{3}\right)\left(\ln\frac{4E_p E_e E'_e}{M_p m_e E_\gamma} - \frac{1}{2}\right), \tag{3.4}$$

using the following definitions: fine structure constant α_e, classical electron radius r_e, energy of the photon E_γ, energy of the incoming and scattered electrons E_e and E'_e, respectively, energy of the proton E_p and masses of the proton and electron M_p and m_e, respectively.

The luminosity monitor [79] consists of a photon calorimeter and an electron calorimeter in the direction of the electron beam as shown in figure 3.5. The luminosity is determined from the rate of photons R_γ above a certain threshold, E_γ^{th}, in the photon calorimeter and the known bremsstrahlung cross section;

$$\mathcal{L} = \frac{R_\gamma\left(E_\gamma > E_\gamma^{th}\right)}{\sigma_{ep\to ep\gamma}\left(E_\gamma > E_\gamma^{th}\right)}, \tag{3.5}$$

with $\sigma_{ep\to ep\gamma}\left(E_\gamma > E_\gamma^{th}\right)$ being the cross section for photons with energy above the energy threshold. The photon calorimeter is a lead-scintillator sampling calorimeter with a carbon filter of one radiation length in front to protect it from direct synchrotron radiation. A presampler in front of the carbon filter is used to correct the measured energies for losses in dead material. The precision achieved for the luminosity measurement was 1.1% in 1996 and 1.8% in 1997.

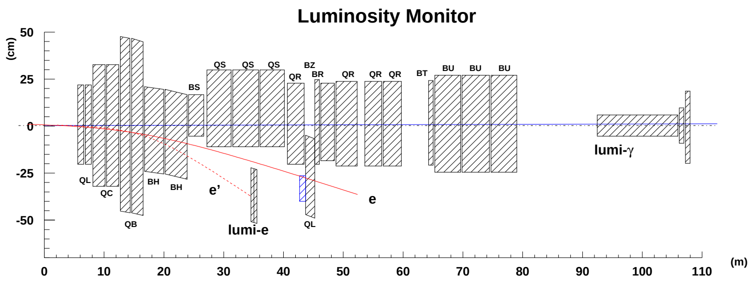

Figure 3.5: *A sketch of the luminosity monitor*

3.2.4 ZEUS Trigger

The majority of events which cause signals in the detectors originate from backgrounds to the ep collisions of interest. Sources of these are synchrotron radiation by the electron beams, bremsstrahlung of electrons in the beam pipe due to the beam gas particles, halo muons originating from the decay of pions produced in collisions of beam particles with the residual beam gas or with the beam pipe and cosmic ray initiated events. The dominant contribution is the proton-beam gas process. Since the amount of information for an event to be stored is of the order of 100 kB there are physical limitations on the number of events from the available space on storage devices and from the output frequency to disk of the acquisition system. At ZEUS, the data acquisition system can write events to disk at a rate of up to 10 Hz. To cope with these limitations and to keep only interesting events a trigger system was set up which is used to discriminate against background and the bulk of low Q^2 events. A layout of the trigger system is given in figure 3.6. Since individual components have signal times which are much longer than the bunch crossing time of 96 ns and hence cannot be part of a trigger decision within this time, a pipeline system has to be used. The ZEUS trigger system has a three-level pipelined trigger system. It consists of the first level trigger (FLT) using fast electronics mounted on the detector, the second level trigger (SLT) using parallel transputer computations on intermediate event information and the third level trigger (TLT) which performs an

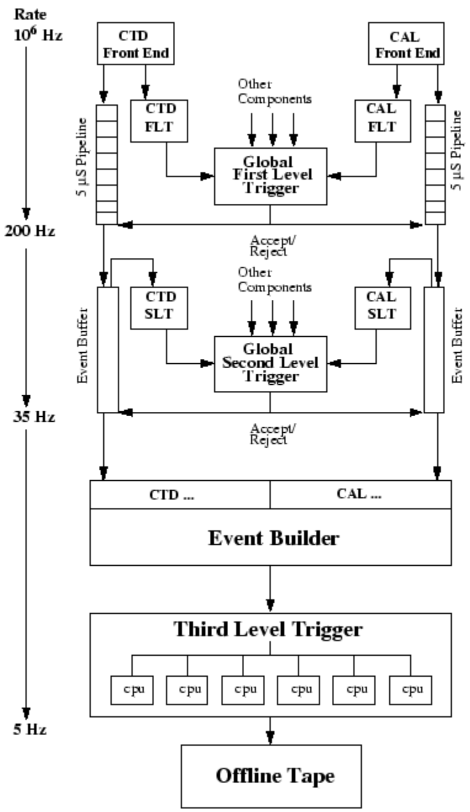

Figure 3.6: *Layout of the ZEUS trigger and data acquisition chain. The actual event rate after the FLT is about 1 kHz, after the SLT about 60 Hz and after the TLT about 10 Hz. The word offline tape stands for the disk mentioned in the text.*

almost full event reconstruction and makes the final trigger decision. The communication between second and third level trigger takes place via an intermediate data collection system (Event Builder) with input from all detector components.

3.2.4.1 First Level Trigger

HERA operates at 10.4 MHz, resulting in a bunch crossing each 96 ns. For 52 bunch crossings, all data are stored in a pipeline at any time, clocked at 96 ns, hence with a depth of about 5 μs while the first level trigger calculations are performed and the first level trigger signal is propagating back to the component. The component's FLT's calculate event observables such as local energy sums, track matching in the $r-z$ plane and timing information. Each component completes its internal trigger calculations and passes information for a particular crossing to the Global First Level Trigger (GFLT) between 1.0 and 2.5 μs after the crossing occurred. The GFLT calculations take about 20 crossings additional time after receiving information from the individual components. The GFLT decision is issued exactly 46 crossings, or 4.4 μs after the crossing that produced it. If a decision to accept is not issued for a crossing, the event is discarded. Otherwise the pipelines are stopped and the data is moved to the event buffer of the second level trigger and to the component second level triggers. The FLT cuts significantly on the beam gas and cosmic interactions rate by using energy sum thresholds in the different regions of the CAL and CTD z-by-timing information for the determination of the z-vertex of events. Using the C5 FLT timing information and the veto wall FLT coincidence signal halo muons and beam gas interactions can be further reduced. It is predominantly these timing cuts which reduce the FLT rate from an input of the order of MHz to a maximum output of $\sim$ 1 kHz.

3.2.4.2 Second Level Trigger

Each component has a second level trigger which is a network of parallel processing transputers connected to the global second level trigger. The data is again pipelined with a smaller depth of 16 buffers due to the lower input rate. At this stage the full information of the component is already digitised, leading to better precision in the determination of tracks or energy sums, such as E_T or $E-P_z$ as explained in 5.6.4.2, compared to the FLT where only a small fraction of the signal was used to determine these sums. A few milliseconds are available for the determination of these quantities, which are then sent to the Global Second Level Trigger for a decision. The maximum output rate of the SLT is 60 Hz.

3.2.4.3 Event Builder

The Global Second Level Trigger decision is not directly passed to the final third level trigger but to the event builder. The event builder collects the data from all ZEUS components and fills the standard data formats needed in the trigger decision calculations of the TLT and for the data storage. Having gathered all the information this block of data is then passed to one of the TLT processors.

3.2.4.4 Third Level Trigger

The third level trigger is a Silicon Graphics© computer farm which runs similar selection algorithms as used by the offline analysis of the data. At this stage several electron finding, jet finding and particle recognition algorithms are applied to the data. If an event fulfills the criteria for a given algorithm an appropriate flag is set. If at the end the events passes one of the physics criteria wanted the TLT issues a trigger decision and writes the data to tape. The event rate is reduced to about 10 Hz.

3.2.5 Offline Data Reconstruction

Data written to tape has to be reprocessed to apply the correct calibration constants for the detector components which differ for different runs. In addition to the calibration of the detector and the calculation of corrected signals, the reconstruction software also performs the tracking, calorimeter clustering and electron reconstruction, storing the information in the appropriate tables.

3.2.5.1 Tracking Reconstruction

The tracks as used in this analysis are based on the CTD information only. Compared to the other ZEUS tracking devices, the CTD performance is significantly better. The reconstruction for the CTD tracks starts with a pattern recognition applied to the hits [80] with the seed taken from the outer hits. The pattern recognition tries to fit a helix to the hits assuming a constant magnetic field using a five parameter helix parametrisation. In a first step a fit is performed using the $x-y$ plane to determine the curvature and reference point in x, y for a circle. In the second step the z coordinates are used to determine the θ angle and z reference point of the track. After the reconstruction of all possible tracks, these are used to determine a primary vertex. Tracks associated with this vertex are refitted using the additional vertex information. The overall efficiency to reconstruct tracks for charged particles is of the order of 95% for particles with transverse momentum larger than 0.2 GeV/c.

3.2.5.2 Calorimeter Reconstruction

The raw calorimeter data as stored is unpacked and calibrated using the calibration constants retrieved in test runs. Within these test runs, which are performed on a daily basis, the uranium noise signal is monitored and used to calibrate the calorimeter. Since the reconstruction of the calorimeter energies plays a key role in this analysis the detailed description is discussed separately in chapter 5.

Chapter 4

Monte Carlo Simulation

4.1 Monte Carlo Overview

Measurements performed with the ZEUS detector have to be corrected for acceptance and resolution effects due to the detector and the trigger systems. These effects have to be understood in order to extract detector independent experimental results and to estimate the related experimental uncertainties. The complex setup of the ZEUS detector with its many different components makes it impossible to calculate the acceptance and the resolution for given quantities from first principles based on the geometrical and internal structure of the detector. Instead a well established probabilistic method called Monte Carlo (MC) is used as in all high energy physics experiments.

The Monte Carlo method can be split into two main parts. The first part is the generation of an event starting from the initial scattering process and ending with the generation of the final state hadrons, performed by event generator programs. The second part is the complete simulation of the effects of the produced hadrons in the detector, its readout system and the offline event reconstruction.

Event generators are capable of the simulation of physics events under investigation. These programs, as used in this photoproduction analysis, are based on leading order perturbative QCD matrix element calculations to simulate the hard subprocess. The non-

perturbative parts of the event generation such as the formation of final state hadrons (hadronisation) or the fragmentation into more than two partons are produced using phenomenological models. The simulation of the detector response in the second part is done by passing the final state particles through a simulation of the ZEUS detector. The MOZART [73] software package, based on the GEANT 3.13 [81] program package from the CERN software group, contains a detailed database of the geometry and composition of all detector components. Using this information, each particle is traced trough the detector and its energy loss, tracking hits, decay interactions etc., are simulated and recorded. Part of the detector simulation is ZGANA [82], a program package to simulate the trigger decision and ZEPHYR, a program package which is the full offline reconstruction on the events.

The analysis as presented here uses two MC event generators for the simulation of the basic photoproduction physics processes, HERWIG 5.9 [83] and PYTHIA 6.1 [84]. Also used are the ARIADNE [85] Monte Carlo and HERWIG 5.9 for the simulation of deep inelastic scattering processes needed for the determination of the energy correction method which will be described in 5.6. The ARIADNE MC is only an hadronisation program and hence has to be used in connection with an event generator which was taken here to be DJANGO 1.1, an interface of the LEPTO 6.5 [86] event generator to HERACLES 4.6 [87], which performs radiative corrections. The ARIADNE model uses the same hadronisation model as PYTHIA. The reason not to use PYTHIA itself for the creation of DIS events for the correction method is its insufficient description of DIS events when compared to ZEUS data.

4.2 The HERWIG Event Generator

The HERWIG event generator is used in this analysis as the main MC. The program uses NLO matrix elements for the calculation of the photon flux from the electron beam in the case of direct photoproduction of order $\mathcal{O}(\alpha\alpha_s)$ (LO) and the equivalent photon approximation for resolved photoproduction. The hard parton scattering process is simulated using leading order QCD matrix elements. The final and initial partons go through a process of showering producing more partons by emission of additional partons, governed by the DGLAP equations as explained in section 1.3.3. The emitted partons are ordered by their opening angle, thus incorporating effects due to the coherence of multiple parton emission. However, interference terms between the initial and final state showers are neglected. The parton shower stops when the virtuality of the parton reaches the cut-off value of $Q_0 \simeq 1$ GeV which is about the scale at which the transition between perturbative and non-perturbative QCD occurs. The initial parton showers which evolve from the initial hadron to the partons of the hard scattering are created by backward evolution. The final state partons after the parton shower are combined into hadrons using a non-perturbative model called the cluster model. The model groups partons into colourless hadrons by splitting any gluon in the final state parton shower into $q\bar{q}$ pairs and recombining the quarks into clusters using the colour connections produced with the parton showers and the branching history. Each cluster is then decayed into two hadrons or the lightest hadron for its flavour in the case of missing mass. The last step is to simulate the decay of unstable hadrons. The factorisation scale used in the Monte Carlo is given by

$$\mu^2 = \frac{2stu}{s^2 + t^2 + u^2}, \tag{4.1}$$

where s, t and u are the Mandelstam variables. Any resulting cross section has divergences as the transverse momentum of the outgoing partons goes to zero, $p_T^2 \rightarrow 0$. The events were therefore generated requiring a minimum transverse momentum, p_T^{min}, as will be detailed later in section 4.5.

4.3 The PYTHIA Event Generator

The PYTHIA event generator shares conceptually many features with HERWIG. It is a general purpose event generator capable of simulating various physics processes in $p\bar{p}$, e^+e^- and ep collisions. It originates from the program JETSET [88] for the hadronic production in the e^+e^- annihilation process. The main differences compared to HERWIG are the

generation of the photon spectrum, the different choice of the factorisation scale μ^2 and the fragmentation model used. The photon spectrum for photoproduction events is generated using the Weizsäcker-Williams approximation [90] for both direct and resolved processes. The factorisation scale, μ^2, used is given by the transverse mass m_T^2 of the outgoing partons

$$\mu_T^2 = m_T^2 = \frac{1}{2}\left(m_1^2 + p_{T,1}^2 + m_2^2 + p_{T,2}^2\right) \tag{4.2}$$

The parton showering differs from the QCD cascade model as used in HERWIG. Instead of treating the partons as independent emitters, the gluon bremsstrahlung is described in terms of radiation from colour dipoles between partons, thus naturally incorporating QCD coherence effects, the model is hence named the Colour Dipole Model [91, 92, 93, 94]. The fragmentation model used for the hadronisation is the Lund string fragmentation model [95] which is based on the simple assumption that the potential between quark and antiquark is proportional to the separation r of the $q\bar{q}$ pair,

$$\phi(r) = \kappa r \tag{4.3}$$

where $\kappa \approx 1$ GeV/fm denotes the mass density per unit length. The "string" potential between the $q\bar{q}$ pair has a narrow transverse dimension of roughly the size of a hadron. The moving apart of the $q\bar{q}$ pair causes an increase in the energy stored in the string until it exceeds the threshold energy for the creation of another $q\bar{q}$ pair. The system is then split into two new strings. The direction of the strings is the direction of the original parton with a transverse smearing of the order of a hadron mass. Reaching a low enough invariant mass, the $q\bar{q}$ pair forms a hadron otherwise the process is repeated. Unstable hadrons are decayed as in HERWIG.

In addition to the above mentioned differences, the PYTHIA event generator was used in a mode allowing for multiple interactions (MI). Multiple interactions allow for more than one parton from each beam particle to interact within the same event. Figure 4.1 shows an example for a multiple interactions event. Since the direct process in photoproduction has no parton component inside the initial photon this can only occur for resolved photoproduction processes. Multiple interactions cause extra soft (*i.e.* low transverse energy) particles to be added between the photon remnant and the proton. With the

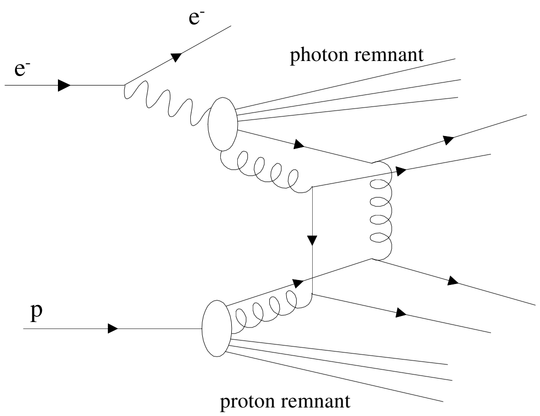

Figure 4.1: *An example of multiple interactions in γp collision*

center-of-mass frame moving forward with respect to the detector rest frame and the soft nature of the additional particles, the energy deposits tend to be distributed in the forward direction of the detector. In the reconstruction of the energies of the jets originating from the hard scattering partons, this extra energy causes a bias. This is especially pronounced in the forward direction and causes the jets from the hard scattering process to become too energetic when comparing the jet energy to the energy of the outgoing partons. The effect is to increase any jet cross sections with a minimum E_T cut especially in the forward direction. The improvement in the description of the energy flows around jets found in photoproduction events, particularly in the forward direction, might be a first sign of the possible presence of multiple interactions in dijet photoproduction ($Q^2 \approx 0$) as reported by the ZEUS experiment [67]. The introduction of the MI for PYTHIA is motivated by work published in [96], where the event generator was tuned using a χ^2-fit to the available photoproduction data. The free parameters within the fits were the photon structure function, the underlying event i.e. MI. and the p_T^{min} of the processes. In the high-E_T dijet analysis using the 1995 data and the same E_T cut criteria [97], it was shown that except at low x_γ^{OBS} the introduction of MI in the Monte Carlo event generator is not needed to describe the energy flow in dijet events as seen in the data. Since the agreement in

the overall description of the data using HERWIG is good, (see section 6.4.1), and the creation of additional Monte Carlo samples limited within the collaboration, no attempt was made to study effects of MI in HERWIG within this analysis.

4.4 DIS Monte Carlo Sample

In addition to the above mentioned photoproduction samples two sets of deep inelastic scattering Monte Carlo samples with $Q^2_{min} > 100$ GeV^2 were used in the study and the determination of the jet energy correction method as will be described in detail in chapter 5. To incorporate the same fragmentation and hadronisation model as the photoproduction Monte Carlo samples, HERWIG and ARIADNE [85] were used for the generation of DIS events. HERWIG allows the creation of DIS events by simply setting the appropriate switch to run in an *ep* mode. Anything after the creation of the hard process proceeds as described above.

The ARIADNE QCD cascade is based on the Colour Dipole Model as in PYTHIA hence this becomes the sample which will be used to determine the energy correction functions for PYTHIA. The proton structure functions used were CTEQ-4D for ARIADNE and GRV-HO for HERWIG. Since the PYTHIA sample was generated without a Q^2_{max} cut, it was used to study the DIS background for which the PYTHIA Monte Carlo is good enough.

4.5 Monte Carlo Samples

In order to minimise the number of events which have to be simulated by the CPU-consuming detector simulation, the generation of the HERWIG and PYTHIA Monte Carlo samples were filtered at the hadron-level of the event generation. Only events fulfilling certain E_T^{min} requirements of the first and/or second jet of hadrons and a $\eta^{jet} < 3.5$ condition were passed to the detector simulation. The given cuts reduce significantly the number of events to simulate without introducing a bias for the final event selection.

Furthermore, several samples using different E_T^{min} requirements were created to enhance the number of events with high E_T jets without the need to create millions of low E_T dijet events. The E_T^{min} requirement had to be fulfilled by the first and second highest E_T jets for the HERWIG sets 1, 2, 6, 7, 8 and 12 as given in table 4.1 while for the others only the highest E_T jet had to pass this cut. For the PYTHIA sets 1, 2, 4 and 5 (see table 4.2) the two highest E_T jet had to fulfill the criteria while again for set 3 and 6 only the highest E_T jet was demanded to pass the cut.

The different samples were then combined by using appropriate event weights calculated by requiring a continuous and smooth distribution in E_T of the jets. Figure 4.2 shows the effect of the reweighting on the E_T spectrum of the highest E_T jet of the events passing the dijet cuts at the hadron-level.

The divergence of the cross section at low p_T for the two outgoing scattering partons made it necessary to require a variable p_T^{min} cut on the partons which is chosen in loose correlation with the E_T^{min} cut of the sample created. In addition, all but two (set 6 and set 12) of the HERWIG samples were restricted to have a Q^2_{max} cut of less than 4 GeV^2 while a separate higher Q^2 sample was generated to study the dijet backgrounds originating from deep inelastic scattering. No Q^2_{max} cut was applied to the PYTHIA samples which made it possible to study the deep inelastic scattering background using the same samples. Tables 4.1 and 4.2 list the Monte Carlo samples used in this analysis with their cross sections, type of process, number of events generated, E_T^{min} and p_T^{min} requirements.

The proton and photon structure functions taken were of leading order. For PYTHIA the parton density function for the photon was SaS-2D [98, 99] and for the proton GRV-94 LO [100], which were seen to describe best the data in the investigation mentioned above. The HERWIG sample was generated using CTEQ-3 [101] as proton and GRV-G [102] as photon parton density function. The choice of the proton structure function should not have a significant impact on the cross section considered since the analysis is performed in a range where the proton parton density functions are experimentally well constrained.

Herwig 5.9	Process	σ [nb]	Events	E_T^{min} [GeV]	p_T^{min} [GeV]	Q^2_{max} [GeV]
Set 1	resolved	14.41	117867	7	6	4
Set 2	resolved	1.726	29798	11	6	4
Set 3	resolved	0.247	19817	21	8	4
Set 4	resolved	0.0353	9900	29	10	4
Set 5	resolved	0.00445	4988	40	20	4
Set 6	resolved	1.1275	9930	7	6	-
Set 7	direct	6.14	45976	7	6	4
Set 8	direct	1.177	29991	11	6	4
Set 9	direct	0.184	19833	21	8	4
Set 10	direct	0.0375	9913	29	10	4
Set 11	direct	0.00648	4924	40	20	4
Set 12	direct	0.4760	9918	7	6	-

Table 4.1: *List of generated HERWIG Monte Carlo samples used in this analysis. The definitions of the variables are given in the text.*

Pythia 5.7	Process	σ [nb]	Events	E_T^{min} [GeV]	p_T^{min} [GeV]	Q^2_{max} [GeV]
Set 1	resolved	30.99	75227	6	3.5	-
Set 2	resolved	6.187	39205	9	3.5	-
Set 3	resolved	0.6258	14931	15	3.5	-
Set 4	direct	18.31	76988	6	3.5	-
Set 5	direct	4.878	44887	9	3.5	-
Set 6	direct	0.6890	19784	15	3.5	-

Table 4.2: *List of generated PYTHIA Monte Carlo samples used in this analysis. The definitions of the variables are given in the text.*

4.5.1 Normalisation

The photoproduction Monte Carlos as described above are based only on LO calculations for the hard scattering process. The lack of higher order diagrams and the incomplete understanding of the hadronisation process results in large uncertainties in the calculations of cross sections for the absolute jet cross sections. To improve the description of the data,

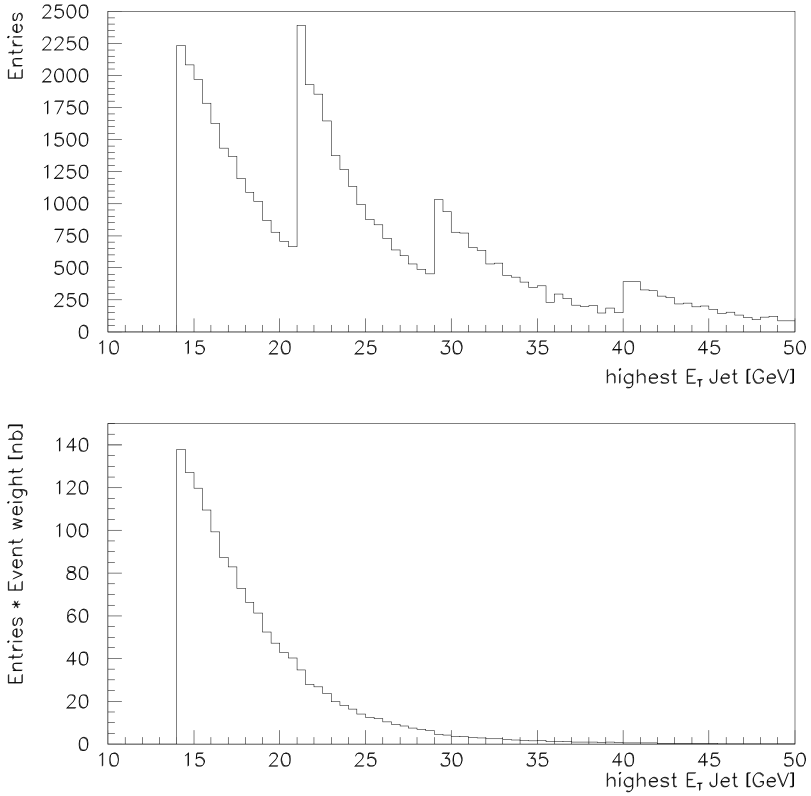

Figure 4.2: *The effect of the event weighting on the E_T spectrum. The upper plot shows for the HERWIG Monte Carlo the number of events versus the E_T of the highest E_T jet for events passing the dijet cuts on the hadron-level. A clear structure due to the different E_T^{min} requirements for the different samples is visible. The lower plot shows the same events where each event is weighted to retrieve a smooth E_T distribution and the same luminosity as the 96/97 data sample.*

the relative resolved and direct contributions in the Monte Carlo samples are scaled. The scaling factors are determined by a fit to the measured x_γ^{OBS} distribution of the data shown in figure 6.14. The resulting scaling factors for HERWIG (PYTHIA) are 1.785 (1.431) and 1.736 (1.160) for the direct and resolved component, respectively. All comparisons to Monte Carlo will contain these factors from now on.

Chapter 5

Reconstruction of Event Variables

The event variables used to describe the kinematics of photoproduction events such as y_{JB}, x_γ^{OBS} and δ are based on the measurement of the hadronic final state only. In contrast to deep inelastic scattering, photoproduction events are characterised by the lack of a scattered electron in the detector. The variables have already been introduced in 2.1 or are described in detail in section 5.1. For many of the hadrons produced in the final state no tracks are reconstructed either because the particle is neutral or it was not within the acceptance of the tracking devices. The kinematic reconstruction hence relies on the accurate measurement of energy as measured by the calorimeters.

The radioactivity of the uranium in the ZEUS calorimeter provides a stable and time independent signal which is used to set the absolute calibration scale as described in section 3.2.2. The same activity however leads to energy deposits within the calorimeter of the order of 1 GeV, which do not originate from ep interactions. This contribution has to be removed to avoid a bias in the reconstruction of the hadronic final state. Section 5.2 describes the algorithm for the reduction of this contribution and of other sources of noise.

Particles reaching the calorimeter have already traversed inactive material causing an undetected energy loss. A part of this energy can be recovered if the tracking information, matched to the appropriate energy deposits in the calorimeter, is taken into account. Additionally, low momentum tracks not reaching the calorimeter can be included in the measurement of the hadronic final state by use of the tracking information. Section 5.3 gives a description of the used matching algorithm.

In any measurement of cross sections having a strong energy dependence, as is the case in this thesis, uncertainties in the hadronic energy determination will have a significant impact on the precision of the measured data. It is therefore important to understand and control the nature and sizes of these uncertainties. Previous analyses of photoproduction at ZEUS found that the hadronic energy uncertainty yielded the largest systematic error. Section 5.4 gives details of the method used to minimise the energy scale uncertainties arising from, in particular, the loss of energy in the dead material.

5.1 Definition of Event Variables

The lack of a detected scattered electron in the final state enforces the reconstruction of the kinematics purely based on the measurement of the hadronic final state. The method used, based on the measurement of the hadronic angles and energies, was developed by Jacquet and Blondel [103]. The kinematic variables are given by

$$Q^2_{JB} = \frac{(\sum P_x)^2 + (\sum P_y)^2}{1 - y_{JB}} \tag{5.1}$$

$$y_{JB} = \frac{\sum(E - P_z)}{2E_e} \tag{5.2}$$

$$x_{JB} = \frac{Q^2_{JB}}{s \cdot y_{JB}}. \tag{5.3}$$

The sum in each case has to be taken over all final state momenta, with E being the energy and P_x, P_y and P_z the momentum components. E_e is the initial electron energy. An important quantity is δ, which is formed from the energy and the z-component of the total hadronic final state momentum;

$$\delta = \sum E - P_z, \tag{5.4}$$

with the sum again over all final state momenta. This variable is primarily used to reduce DIS background, in which case $\delta \approx 2 \cdot E_e$. For simplicity it is also referred to as $E - P_z$.

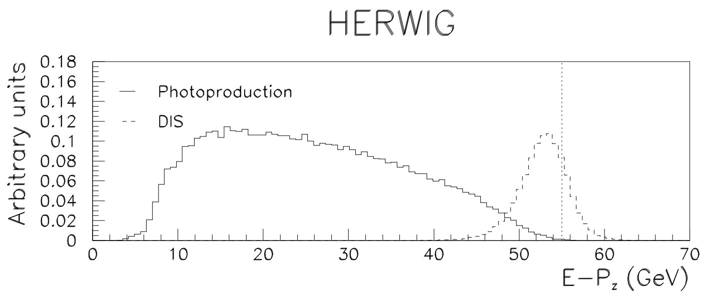

Figure 5.1: *Comparison of $E - P_z$ distributions for photoproduction and DIS using the HERWIG Monte Carlo. The distributions are shown in arbitrary units and are neither normalised to the same area nor to the same luminosity. The distributions are shown for uncorrected calorimeter quantities. The dotted line in the right hand side plot is at twice the initial electron energy.*

The difference in this quantity for photoproduction dijet and DIS events can be seen in figure 5.1.

5.2 Reduction of Calorimeter Noise

The uranium noise signal (UNO) inside calorimeter cells leads to an energy deposition simply referred to as noise. The size of this contribution can be determined by use of calorimeter calibration triggers taken when no electron and proton beams are present by integrating the signal over 20 ms to cancel statistical fluctuations. In the detector simulation the contribution is modeled based on this information. A comparison of the UNO signal as seen in Monte Carlo and data is given in figure 5.2. The mean value is centered around zero with a width of $\sim$ 18 MeV in the EMC and $\sim$ 27 MeV in the HAC sections.

At the reconstruction level, a noise suppression cut on the absolute value of the cell energy of 100 MeV for EMC and 150 MeV for HAC cells is applied to all calorimeter cells [104]. Comparing empty Monte Carlo events with data taken during normal operation but with no ep interaction a comparison of the multiplicities of noisy cells was done. It

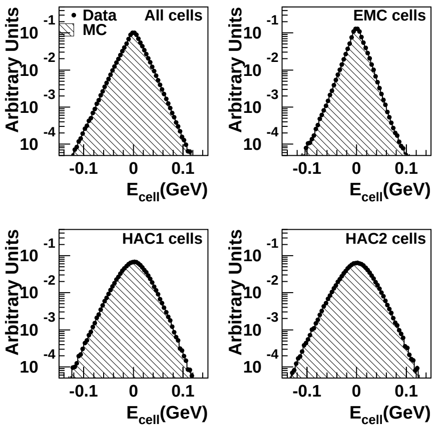

Figure 5.2: *Comparison of the UNO signal as seen in data and Monte Carlo for all calorimeters.*

was found that additional sources of noise such as sparks or noise in the PMT themselves or in the readout electronics, which are not simulated in the detector, lead to an average of 6 EMC and 2 HAC cells per event remaining in the data. Using the asymmetry A, from the left and right PMT signals defined as A=E_{left}-E_{right}, cells are removed if their energy, E_{cell} = E_{left}+E_{right}, is less than 0.7 GeV and if the following relation for the absolute value of the asymmetry holds:

$$|A| > 0.49\mathrm{E}_{cell} + 0.03\ \mathrm{GeV}. \tag{5.5}$$

In addition to this cut, each physics run has a list of noisy cells. An isolated cell is removed from the sample if its energy signal is larger than the average noise signal plus three standard deviations retrieved for this cell within the run using empty events.

5.3 The Hadronic Energy Flow Algorithm

The reconstruction of the hadronic final state in photoproduction based on the calorimeter information alone can be improved by using tracking information from the CTD whenever

this provides a better energy resolution of the object to measure. The major problem in the implementation is to avoid double counting of energy. This is the basic concept of the hadronic energy flow algorithm leading to hadronic final state objects called **Z**eus **U**nidentified **F**low **O**bjects (ZUFO,ZUFOs) [105].

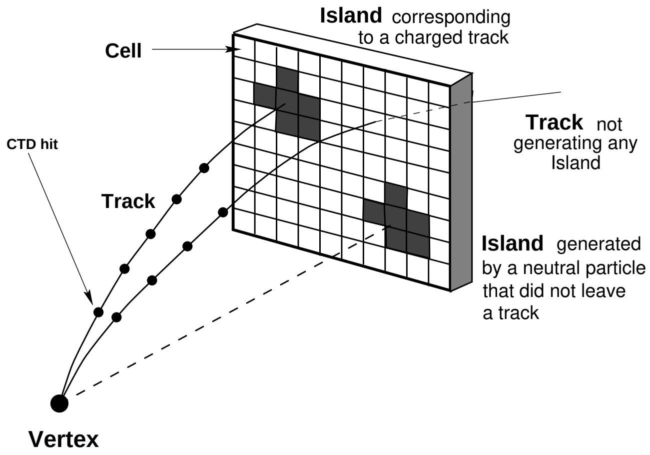

Figure 5.3: *Sketch of the hadronic energy flow algorithm. For charged particles the combined (if available) information from CTD tracking and the calorimeter is used. For neutral particles the algorithm relies on the calorimeter measurement.*

Figure 5.3 shows a schematic representation of the calorimeter and tracking information and their relation which is then used inside the algorithm. Initially calorimeter cells are clustered into so-called cone islands [105]. The clustering process is split into two steps. In an iterative process, the cells of the EMC, HAC1 and HAC2 sections of each calorimeter part are combined separately with their highest energy neighbours to form local islands. This can be done either by connecting nearest neighbours only or also next-to-nearest neighbours. The two different definitions are shown schematically in figure 5.4. Next, the islands are clustered in a $\theta - \phi$ cone starting from the outer HAC sections using probabilities derived from a single pion Monte Carlo simulation. Charged tracks are then extrapolated to the calorimeter surface and associated to a cone island, if possible. Only tracks originating from the primary vertex which passed at least three superlayers and

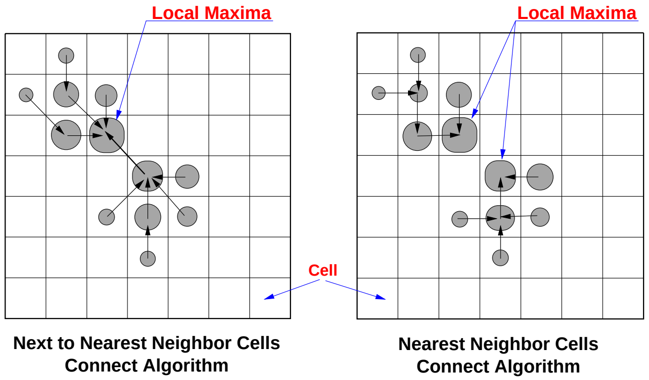

Figure 5.4: *Schematic representation of the two cell island clustering modes*

with a transverse momentum, p_T, between 0.1 to 30 GeV are used in this step. The result of the procedure is a set of track-cluster entities. For each of these objects a decision has to be made which information, either CTD or CAL, will be used to determine the four momenta of the hadronic particles in the event. For three types of track-cluster combinations the decision is simple. For charged tracks not associated to any calorimeter cluster, the track information will be used under the assumption that the particle is a pion. Calorimeter objects which are not associated to any track are counted as neutral particles. The calorimeter information is used and zero invariant mass, $E^2 = p^2$, is assumed. Calorimeter objects associated with more than 3 tracks are called jet-clusters. The calorimeter information is used and zero invariant mass, $E^2 = p^2$, is assumed. The track measurement is used if the two following rules are fulfilled: the calorimeter energy deposit is due to the associated track alone, leading to equation 5.6, and the momentum resolution of the CTD track measurement is better than the energy resolution of the calorimeter measurement of the cone island as stated in equation 5.7. The requirements to replace calorimeter information by tracking information become:

$$\frac{E_{Island}}{p_{Trk}} < 0.8 + \Delta\left(\frac{E_{Island}}{p_{Trk}}\right) \tag{5.6}$$

$$\frac{\Delta p_{Trk}}{p_{Trk}} < \frac{\Delta E_{Island}}{E_{Island}}, \tag{5.7}$$

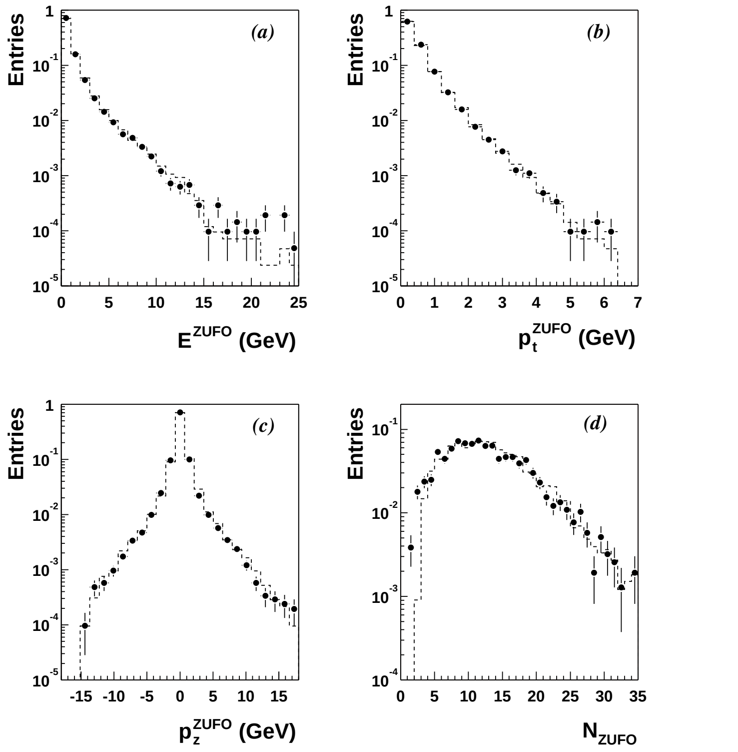

Figure 5.5: *Overall distributions of ZUFO properties: (a) Energy, E^{ZUFO}, (b) transverse momentum, p_t^{ZUFO}, (c) longitudinal momentum, p_z^{ZUFO} and (d) number of ZUFOs, N^{ZUFO}. The points are data and the dashed line shows the reconstructed distributions for the HERWIG Monte Carlo.*

where Δp_{Trk} and ΔE_{Island} are the uncertainties assigned to the measurement of the track momentum and the island energy and $\Delta\left(\frac{E_{Island}}{p_{Trk}}\right)$ is the uncertainty on the ratio of E_{Island} and p_{Trk}. The first requirement ensures that no energy associated to a neutral particle is rejected. The second requirement improves the energy resolution since the information with the smaller relative uncertainty is used. In all other cases the island information is used. Figure 5.5 shows an overall comparison of data and Monte Carlo ZUFOs for quantities derived from using ZUFOs.

5.4 Energy Response of the Calorimeter

From the beginning of the ZEUS data taking it became apparent that the spectrum of measured electron energies with the ZEUS calorimeter in neutral current DIS events was inconsistent with that from Monte Carlo [106]. Several sources of these discrepancies between data and Monte Carlo simulation have been investigated.

Studies have been performed under the assumption that the main reason for the differences between data and Monte Carlo simulation lies in the absolute energy response of the calorimeter [107, 108, 109]. Using a high Q^2 DIS sample with an isolated electron and a single jet-like hadronic final state the difference in the transverse momentum of the hadronic final state, reconstructed using two different methods, with respect to the transverse momentum of the electron, was studied. The first reconstruction method is based on the measurement of energies while the second uses the two angles of the electron and the hadronic final state to reconstruct the transverse momentum and hence is named double angle method. This double angle method has the advantage of being, to first order, independent of uncertainties in energy measurements. The study resulted in correction factors for the calorimeter cell energy depending on the type and location of the cell. The factors applied to the cell energies are given in table 5.1. The actual values are averages per calorimeter section of two independently performed studies [110, 111].

	EMC	HAC
FCAL	1.041	0.9525
BCAL	1.0515	1.079
RCAL	1.025	1.025

Table 5.1: *Energy correction factors as used for the different calorimeter cell types.*

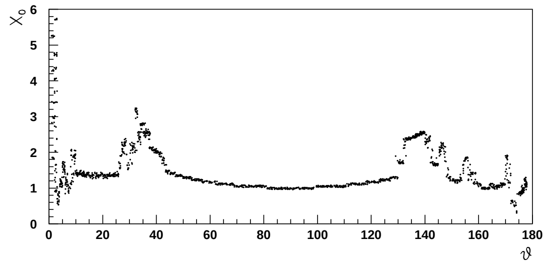

Figure 5.6: *Inactive material in front of the calorimeter as seen in the detector simulation in units of radiation lengths X_0 versus the polar angle.*

5.5 The Dead Material Simulation

Particles reaching the calorimeter have already traversed inactive material causing an undetected energy loss. This dead material consists of the beam pipe, the inner tracking chambers and solenoid and varies from 1 to 3 radiation lengths. A picture of the dead material map as seen in the detector simulation is shown in figure 5.6. The dead material distribution is averaged over ϕ since in most of the regions of interest the actual ϕ dependence can be neglected. Low energy particles will lose a relatively large amount of their energy in this dead material. Differences in data and Monte Carlo simulation may arise due to differences in the multiplicities and energy spectra of low energy particles as seen in data and Monte Carlo as well as due to incorrect implementation of the dead material map in the detector simulation. It was also found that for particles entering the transition regions between the different calorimeter parts FCAL, BCAL and RCAL the energy response is not well modeled in the detector simulation [108].

5.6 The Energy Correction Method

The use of tracking information in the reconstruction of the hadronic final state reduces the dependence on differences in the calorimeter energy scale between data and detector simulation. The majority of ZUFOs are, however, still calorimeter objects. To compensate for the energy losses in front of the calorimeter, an energy correction method has been developed. To reduce the sensitivity to energy scale and differences between data and detector simulation, a method was chosen which determines the corrections for data and Monte Carlo independently. The method developed specifically for this analysis is based on and is the extension to a work performed for an analysis of 1995 data [71, 112]. The current method has been developed for the 1996 and 1997 data explicitly. Preliminary results, based on the work of this thesis, have been presented at the Conference on Calorimetry in High Energy Physics 2000 [113]. The final results improve the energy scale uncertainty from 3% to within 1.5%.

The method is based on energy and momentum conservation to determine the energy corrections for the hadronic final state particles. A sample of high Q^2 DIS events was selected in a phase space where either the transverse momentum of the scattered electron or the kinematic variable y can be measured with good resolution using the double angle method. The double angle method determines the kinematic variables from a measurement of the angles of the scattered electron and the hadronic final state and is thus to first order independent from the energy scale [114]. The kinematic variables are given by

$$Q^2_{DA} = 4E_e^2 \frac{\sin\gamma_h(1+\cos\theta_e)}{\sin\theta_e + \sin\gamma_h - \sin(\theta_e+\gamma_h)}, \tag{5.8}$$

$$x_{DA} = \frac{E_e}{E_p}\frac{\sin\theta_e + \sin\gamma_h + \sin(\theta_e+\gamma_h)}{\sin\theta_e + \sin\gamma_h - \sin(\theta_e+\gamma_h)}, \tag{5.9}$$

$$y_{DA} = \frac{\sin\theta_e(1-\cos\gamma_h)}{\sin\theta_e + \sin\gamma_h - \sin(\theta_e+\gamma_h)}, \tag{5.10}$$

where E_e and E_P are the initial electron and proton energies, θ_e , the scattered electron angle and γ_h the angle of the hadronic final state which is determined by the formula

$$\cos\gamma_h = \frac{(\sum P_{T,x})^2 + (\sum P_{T,y})^2 - (\sum(E-P_z))^2}{(\sum P_{T,x})^2 + (\sum P_{T,y})^2 + (\sum(E-P_z))^2}. \tag{5.11}$$

The expression represents the p_T-weighted cosine of the polar angle of the hadronic final state. Using these equations an expression for the energy of the scattered electron in the double angle method, E_{DA}, can be derived;

$$E_{DA} = \frac{2E_{beam}\,(1-y_{DA})}{1-\cos\theta_e}. \tag{5.12}$$

Correction functions for energy loss are determined via an iterative minimisation procedure. The expression to be minimised consists of two parts. The first part is the sum of the squared relative differences of the transverse momentum of the hadronic final state $p_{T,HFS}$ and the transverse momentum of the scattered electron $p_{T,elec}$ over events which are labeled as a whole p_T-sample:

$$\sum_{p_T}^{sample}\left(\frac{p_{T,HFS}-p_{T,elec}}{p_{T,elec}}\right)^2, \tag{5.13}$$

where $P_{T,elec}$ is determined from the double angle scattered electron energy E_{DA} as

$$p_{T,elec} = E_{DA}\cdot|\sin\theta|. \tag{5.14}$$

The second part is the sum over the absolute relative differences of y_{DA} and y_{JB}, the latter being related to the longitudinal energy, over events which are collectively labeled high-y sample:

$$\sum_{high\ y}^{sample}\left(\frac{y_{JB}-y_{DA}}{y_{DA}}\right)^2. \tag{5.15}$$

The second sample had to be introduced to overcome a lack of events with particles going into the backward region of the detector. Within the first sum the transverse momentum of the hadronic final state is given by the transverse momentum of the sum over all ZUFOs momenta. While ZUFOs with the energy determined based on track information are assumed to be accurately measured, ZUFOs with energy information coming from the calorimeter are assumed to have lost energy in dead material. These are multiplied by a correction function, the free parameters of which are to be determined by the minimisation. Hence the sum is a function of the parameters to be found by the minimisation process. The same applies for the second sum, where through the dependence of y_{JB} from the ZUFOs momenta, the sum becomes again a function of the parameter to be found. Calculating the total of the sums and changing the correction functions input parameter, a global minimum of the total sum as function of the correction functions can be determined.

The input events to the minimisation procedure are high Q^2 events from data and Monte Carlo. For each Monte Carlo generator used in this analysis the correction functions are determined separately minimising possible sources of inconsistencies which might originate by the use of different hadronisation models. The global DIS selection requirements are given in table 5.2.

$\|z_{vertex}\| < 40$ cm
$Q^2_{DA} > 100$ GeV^2
$E_{DA} > 15$ GeV
$y_{elec} < 0.95$
$\|E_{DA} - E'_e\|/E_{DA} < 0.05$

Table 5.2: *High Q^2 DIS selection cuts used in the definition of the samples. Except of the last item these are the standard DIS selection cuts for ZEUS analyses.*

The y_{elec} (for the definition see equation 6.15) cut removes photoproduction background events while the requirement that the difference in energy of the scattered electron should be small, as determined by the double angle method (see also equation 5.12) and measured by the calorimeter, reduces the bias due to events with final state radiation in the determination of y_{DA}.

The two samples used are defined as follows:

5.6.1 The p_T Sample

The p_T subsample is defined by the additional requirements that the energy of the scattered electron E_{DA} is greater than 25 GeV and the transverse energy of the scattered electron $p_{T,elec}$ is greater than 10 GeV where $p_{T,elec}$ is defined using the double angle energy measurement of the electron to be

$$p_{T,elec} = E_{DA} \cdot |\sin\theta|. \tag{5.16}$$

The overall resolution in this variable compared to the transverse momentum determined using the hadronic final state $p_{T,HFS}$ is shown in figure 5.7.

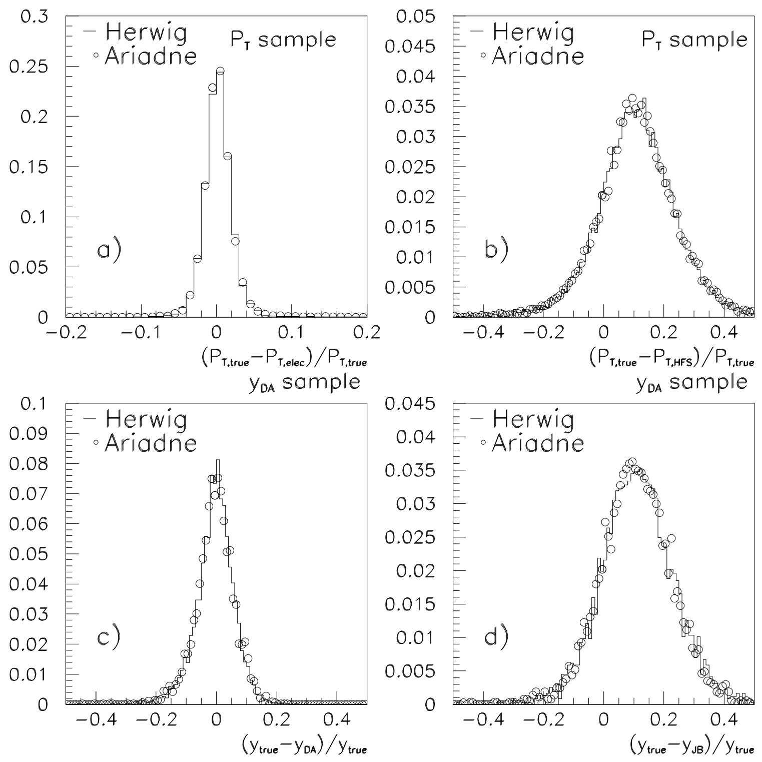

Figure 5.7: *a) The resolution in transverse momentum of the scattered electron compared to the true value. The mean for both Monte Carlo is about 0.2 % with a standard deviation of 2 %. b) The resolution in the transverse momentum of the hadronic final state compared to the true value. The mean for both Monte Carlo is about 11 % with a standard deviation of 12 %. c) The resolution in y_{DA} compared to y. The mean is about 0.2 % with a standard deviation of 6 %. d) The resolution in y_{JB} compared to y. The mean is about 12 % with a standard deviation of 11 %. Both Monte Carlo agree with each other up to the last digit quoted here.*

5.6.2 The high-y_{DA} Sample

The y_{DA} sample is defined by the additional requirements, $15 < E_{DA} < 25$ GeV and $y_{DA} > 0.3$. Low y events have little hadronic activity inside the detector resulting in a worse resolution compared to higher values of y. The overall resolution in y_{DA} as shown in figure 5.7 is worse than the resolution in p_T. To minimise the impact on the global minimisation due to the worse resolution while at the same time keeping enough events for a smooth dependence on the minimisation procedure, the above y_{DA} cut was chosen and the ratio of this sample with the p_T sample was optimised as described in the next section 5.6.3.

5.6.3 The Final Minimisation Expression

The final functional form to be minimised is given by

$$\sum_{p_T}^{sample} \left(\frac{p_{T,HFS} - p_{T,DA}}{P_{T,DA}} \right)^2 + f \cdot \sum_{high\ y}^{sample} \left(\frac{y_{JB} - y_{DA}}{y_{DA}} \right)^2 , \tag{5.17}$$

with f being a function of the relative weights of two samples. Events with a relative difference larger than 20 % away from the mean difference corresponding to about 2 σ are excluded from the minimisation to restrict it to well measured events and to improve the stability of the fit. The variable $p_{T,HFS}$ and y_{JB} depend on the momenta of all ZUFOs in the event and the value of the correction function parameters which are optimised by minimising the given expression. The transverse momentum of the electron depends through E_{DA} on the energies of all final state particles, which are changed within the minimisation procedure. The dependence on the energy changes performed during the minimisation was found to be negligible as shown in figure 5.8, where the relative difference distributions of the uncorrected and corrected values of E_{DA} and y_{DA} are given together with gaussian fits to the distributions. Both Monte Carlo used in the minimisation procedure show the same behaviour and have similar widths in the distributions. The small width in the distribution of the change in the variable E_{DA} shows the expected benefit of the double angle reconstruction method, since it is to first order independent from the energy scale. For y_{DA}, the dependence on the iteration was seen to be larger but with a width still smaller than the resolution of the variable with respect to the true y value. The energy correction is parametrised as a function of the energy and the polar angle θ of the ZUFO. The polar angle dependence reflects the geometry of the detector. The minimisation is performed and correction factors found in seven polar angle bins. The chosen binning in

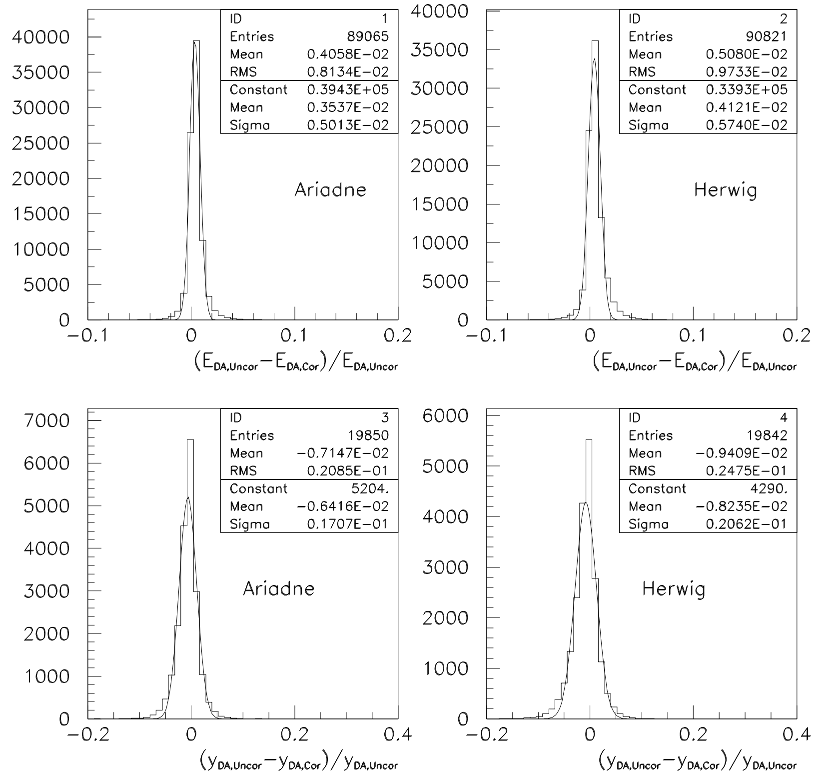

Figure 5.8: *Relative change of the minimised variables E_{DA} and y_{DA} before and after the minimisation procedure.*

θ is

$$0° \to 7° \to 37° \to 44° \to 86° \to 118° \to 144° \to 180°, \tag{5.18}$$

where information from the dead material map shown in figure 5.6 combined with geometric information and requirements for stability of the fit was used in the definition. The energy dependence is parametrised in each bin of θ as

$$f_i(E) = 1 + \frac{A_i}{E^{B_i}}. \tag{5.19}$$

The parametrisation above was found to best fit the energy loss studied using single track-cluster matches. Another function studied was of the form, originally used for the 1995 analysis,

$$f_i(E) = 1 + A_i \cdot e^{-B_i \cdot E}, \tag{5.20}$$

where B can either be a fixed variable or a free parameter of the minimisation. The chosen form in equation 5.19 was found to be also used in previous studies of energy loss in the dead material [108]. Since ZUFOs have an absolute minimum energy above 0.1 GeV (originating from the noise reduction applied, see section 5.2), the singularity at zero has no impact.

The minimisation program is based on the MINUIT [115] package. A total of 14 free parameters must be determined by the minimisation. The minimisation was performed varying the ratio of the two samples and taking the best resolution in the reconstruction of $p_{T,HFS}$ and y_{JB} as criteria for the best method. The optimal ratio of selected p_T sample to selected y_{DA} sample events was found to be 10:1. The results of the minimisation are shown in figure 5.9. Except for the first θ bin, general agreement between the data and the two Monte Carlos is found. The differences which do exist indicate, however that a separate treatment of the different Monte Carlo generators and data is well motivated.

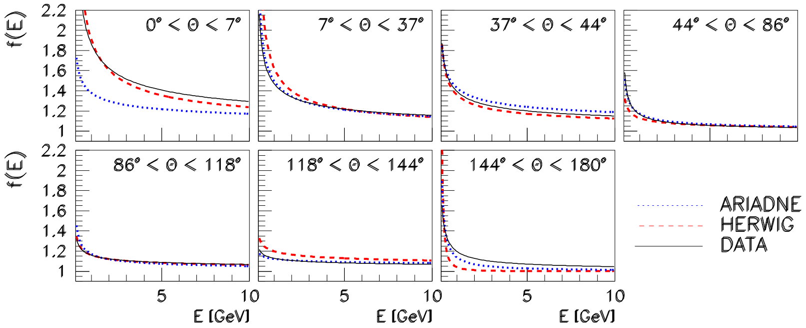

Figure 5.9: *The correction functions in all different θ bins for data and the two Monte Carlo generators used.*

5.6.4 Tests of the Energy Correction

The energy correction extracted has been applied to photoproduction and DIS Monte Carlo events to study the general improvement of the reconstruction of hadronic final state variables, transverse jet energies and energies scale uncertainties.

5.6.4.1 Tests with Photoproduction

To study the impact of the energy correction on the dijet analysis, the transverse energies of jets as seen in the detector in the Monte Carlo samples, from now on labeled detector-level jets, were compared to the jets reconstructed from the final state hadrons, hadron-level jets, using three different methods. The first method uses uncorrected calorimeter cell information in the construction of jets, the second ZUFOs and the third energy-corrected ZUFOs.

Figure 5.10 shows the relative difference of the transverse momentum of the hadron-level and detector-level jets as a function of the pseudorapidity of the jets, η^{jet}. The resolutions, as seen in the HERWIG Monte Carlo, are indicated as the shaded bands. The resolutions for the PYTHIA Monte Carlo are not shown for reasons of clarity, but are essentially the same and show similar dependence as the HERWIG Monte Carlo resolutions. The transverse energies of the detector-level jets were required to be greater than 11 GeV which is the lowest transverse energy used in the dijet analysis. The use of ZUFOs reduces the bias in the reconstruction and improves the resolution compared to the detector-level jets reconstructed using CAL cells. The η-dependence of the relative difference shows an almost flat behaviour compared to calorimeter cells jets reducing the dependence of the reconstruction of the E_T of the detector-level jets on the accuracy of the η measurement. The transition region for the F and BCAL at $\eta \approx 1.1$ shows up as problematic region in the reconstruction of calorimeter detector-level jets. The transition region from BCAL to RCAL at $\eta \approx -0.72$ is not that visible due to the overall deterioration of the jet reconstruction in the backward direction. The use of ZUFOs improves the transverse energy measurement in the transition and backward regions. The

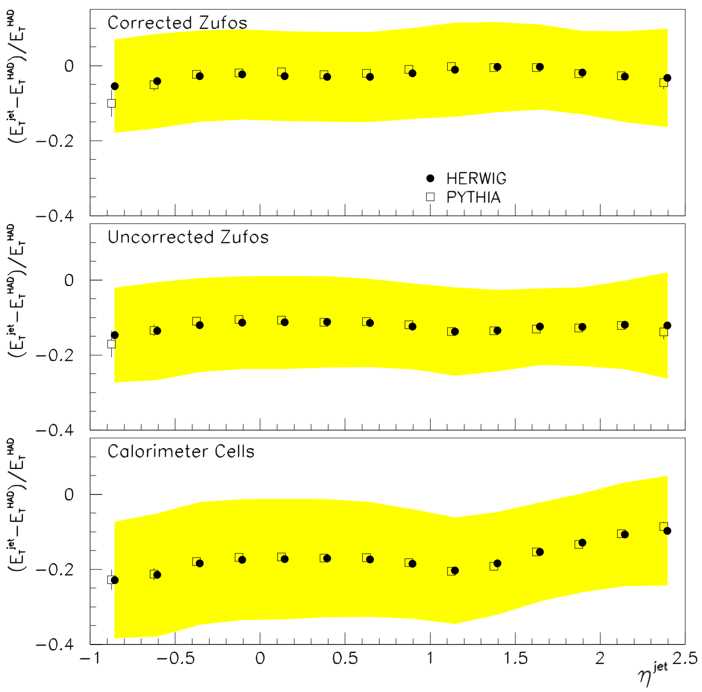

Figure 5.10: *Comparison of the bias and resolution of the transverse energy reconstruction of detector jets E_T^{jet} as function of the pseudorapidity η^{jet} using different inputs for the jet algorithm. Indicated as shaded band are the resolutions for the HERWIG Monte Carlo.*

energy corrected ZUFOs further minimise the bias in the reconstruction of the detector-level jets. Over most of the η range, the agreement between the detector and hadron-level jets is better than 2.5% for the energy-corrected ZUFOs.

Figure 5.11 shows the relative difference of the transverse momentum of the hadron-level and detector-level jets as a function of the transverse energy E_T^{jet} of the detector-level jets for different bins in η. Again resolutions are given for the HERWIG Monte Carlo, indicated by the shaded bands. The above stated conclusions still hold. A small remaining linear dependence in the reconstruction of the transverse energy E_T^{jet} as function of the transverse energy E_T^{jet} can be seen. The similarity of this dependence for the PYTHIA

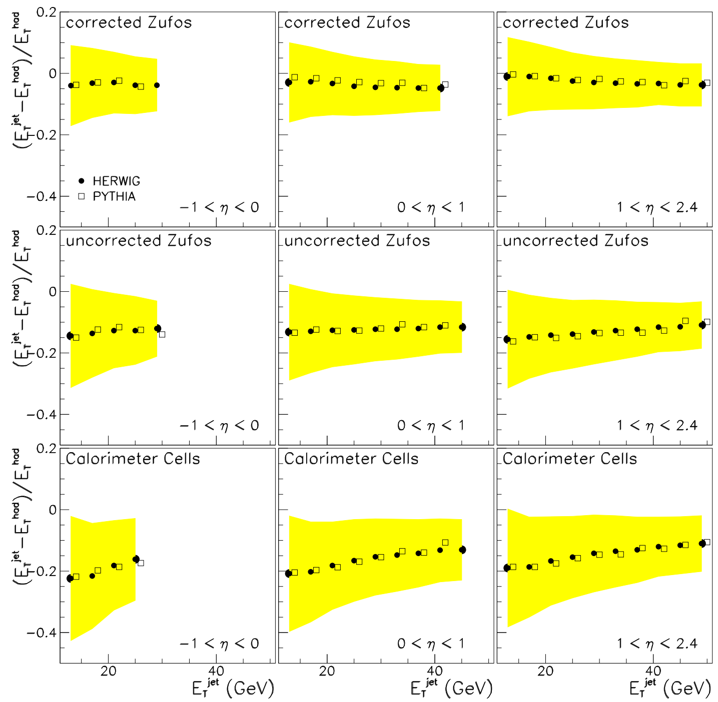

Figure 5.11: *Comparison of the bias and resolution of the transverse energy reconstruction of detector jets E_T^{jet} as function of the transverse energy E_T^{jet} of the jets in different η bins. Indicated as shaded band are the resolutions for the HERWIG Monte Carlo.*

and HERWIG Monte Carlos supports the presumption that this energy correction method is independent of the hadronisation model used.

Shown in figure 5.12 is the reconstruction of the kinematical variable y_{JB} based on calorimeter cells, ZUFOs and corrected ZUFOs information. The figure shows the relative difference between y_{JB} and y_{true} as function of the x_γ^{OBS}. x_γ^{OBS} as defined in equation 2.4 measures the relative contribution to $E - P_z$ from the jets. For high x_γ^{OBS} values, most of the $E - P_z$ is contained in the jets. The deviation from the true y values is largest at low x_γ^{OBS}. This behaviour is expected for resolved photoproduction events, where some of the final state hadrons will escape without detection through the backward beam pipe

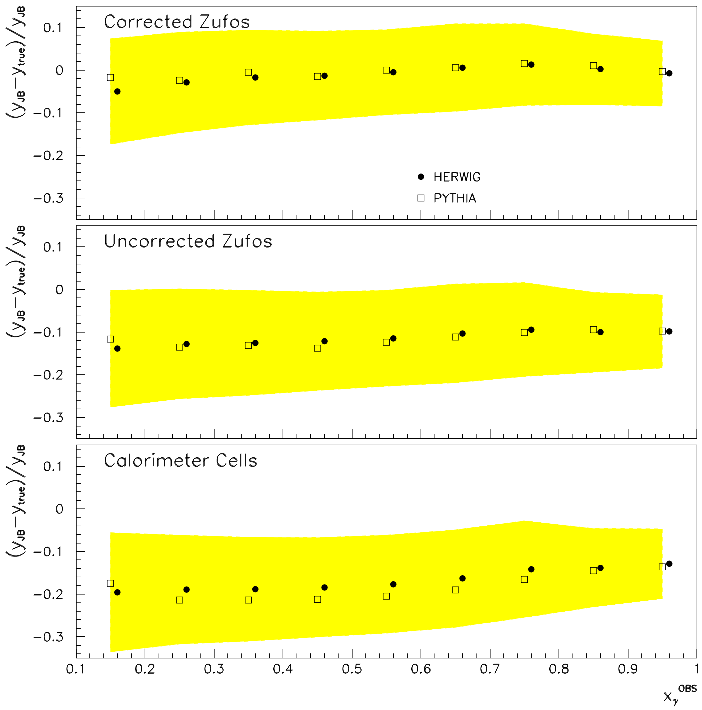

Figure 5.12: *Comparison of the bias and resolution of the reconstruction of y_{JB} as function of x_γ^{OBS}. Indicated as shaded bands are the resolutions for the HERWIG Monte Carlo.*

hole. The differences in the reconstruction of the variable y_{JB} for the two Monte Carlo samples diminishes when using corrected ZUFOs. Except in the lowest bin of x_γ^{OBS} the deviation of y_{JB} from the true value of y is within 2% for corrected ZUFOs.

As can be seen from the distributions displayed above, the use of this energy correction method for ZUFOs based on a global minimisation procedure gives significant improvements in both the reconstruction of jet transverse energies and y_{JB}.

5.6.4.2 Tests with DIS

Having seen the good performance of the energy correction method for ZUFOs applied to photoproduction Monte Carlo events, the focus in this section is the comparison of data with Monte Carlo events. The comparison is done for the transverse momentum of the hadronic final state p_T and the kinematical variable y using DIS events. The scattered electron allows for the determination of p_T and y using the angles of the final state hadrons and electron, which gives to first order an energy scale independent measurement of these quantities. The comparison is made for calorimeter cells and a reconstruction of these variables based on energy corrected ZUFOs.

The reconstruction of the hadronic transverse momentum $p_{T,HFS}$ is given by a sum over all momenta within the event, which are either based on calorimeter cells or ZUFOs information, excluding the scattered electron. The transverse momentum is reconstructed with the double angle method, where it is given by

$$p_{T,DA} = 2E_e\,(1-y_{DA})\,\frac{\sin\theta'_e}{(1-\cos\theta'_e)}, \tag{5.21}$$

with the initial electron energy E_e and the scattered electron angle θ'_e.

In figure 5.13 the relative difference between the p_T, reconstructed using the hadronic and the double angle method, is shown as a function of γ_h (as defined in equation 5.11) for data and HERWIG and ARIADNE Monte Carlo. In addition the relative differences between data and Monte Carlo are plotted. Using the calorimeter information alone a difference in the energy response of data compared to Monte Carlo is seen of about 2% in the BCAL region, the data being higher than the MC. For energy corrected ZUFOs this discrepancy decreases to within 1% over the whole γ_h range.

In figure 5.14 the relative differences between the y_{JB} and y_{DA} are plotted, again as function of γ_h, for data and the above mentioned Monte Carlos. Differences between data and Monte Carlo are again visible with about the same size as in the transverse momentum distributions above. Again the energy corrected ZUFOs lower these differences to below 1% for the HERWIG and just a little above 1% for the ARIADNE Monte Carlo.

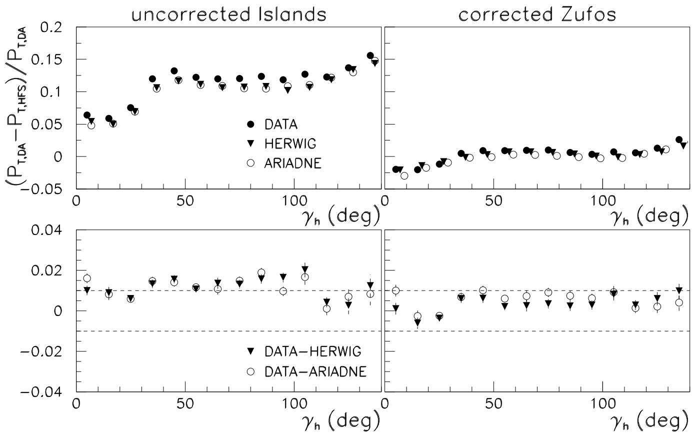

Figure 5.13: *Comparison of the final state transverse momentum p_T using the hadronic and double angle method in the reconstruction. Also given are the differences between data and the Monte Carlo used. The dotted lines indicate differences of ± 1 %.*

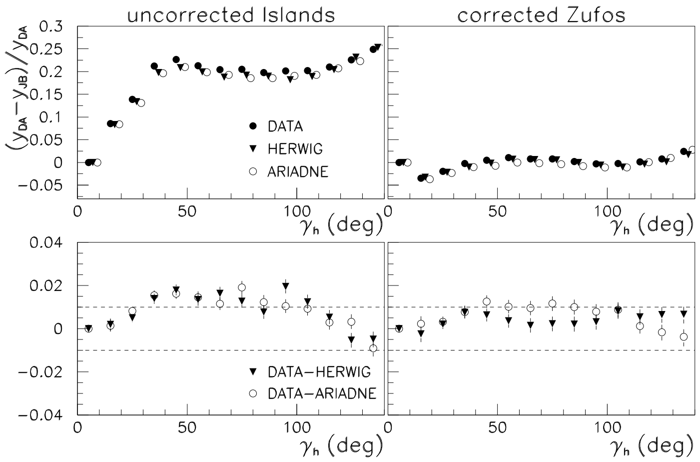

Figure 5.14: *Comparison of the kinematical variable y using the Jacquet-Blondel and double angle method in the reconstruction. Also given are the differences between data and the Monte Carlo used. The dotted lines indicate differences of ± 1 %.*

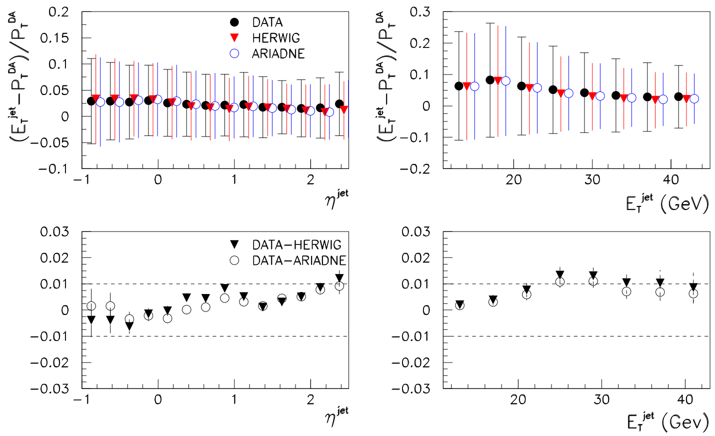

Figure 5.15: *Comparison of the relative difference of $p_{T,DA}$ and E_T^{jet} as function of η^{jet} and E_T^{jet}. Also shown is the difference of data and Monte Carlo. The error bars in the top plots indicate the resolutions.*

A further test of the agreement in the reconstruction of transverse energies of jets using energy corrected ZUFOs is shown in figure 5.15, where the transverse energy of the highest E_T jet is used instead the total hadronic $p_{T,HFS}$. The relative difference of E_T^{jet} and $p_{T,DA}$ as function of η^{jet} and as E_T^{jet} are plotted. Since these are not the same quantities an exact balancing of $p_{T,DA}$ and E_T^{jet} is not expected. This comparison is purely motivated to test the transverse jet energy reconstruction and to estimate an energy scale uncertainty for the transverse jet energy reconstruction between data and Monte Carlo. The differences between data and the used Monte Carlo are below 1% as function of η^{jet}. This holds over the full range in η and for both Monte Carlos except in the very forward η bin for HERWIG. As function of E_T^{jet} these differences are within 1.3%. These values have to be compared to a uncertainty of 2-3% in a comparable analysis for the 1995 data [71]. The newly implemented energy correction method marks a major improvement in the energy corrections for ZUFOs. Without the achieved energy scale precision any extraction of differential cross sections would be limited by the energy scale uncertainty.

Chapter 6

Event Selection

The work presented in this analysis is based on data collected with the ZEUS detector in 1996 (10.8 pb^{-1}) and 1997 (27.9 pb^{-1}) and corresponds to an integrated luminosity of 38.7 pb^{-1}. The averaged estimated uncertainty for the integrated luminosity is 1.6%. The following sections will present the online and offline selection criteria for photoproduction events. To understand the relation between these criteria and background reduction, a short summary of the background sources relevant to this analysis is given in section 6.1. The online event selection is performed using the ZEUS three-level trigger system, with details described in section 6.2. The selected events are reconstructed and corrected as described in chapter 5, after which the final selection cuts are applied. Section 6.3 describes the final cuts and their impact on the background reduction while section 6.4 shows comparisons between Data and MC events selected using the same criteria.

6.1 Background Processes

To understand the choice of the selection criteria applied, a summary of the processes causing background to the dijet photoproduction sample is given. The background processes are separated into two distinct classes.

The first class of events originates from non-ep-physics events, which are due to inter-

actions of the proton and/or electron beam with residual beam gas molecules within the beam pipe, beam scraping or interactions of the halo muons which accompany the proton beam and cosmic muons, which are mainly entering the detector from above. These events can be reduced significantly through requiring a reconstructed vertex close to the nominal interaction point and specific time difference in the energy signals coming from the different calorimeter components consistent with an interaction in the central region of the detector.

The second class are ep interactions of different physics types, which are neutral current deep inelastic scattering (NC-DIS) events and charged current deep inelastic scattering events. The rejection for NC-DIS is based on the $E - P_z$ distribution (see equation 5.4 and figure 5.1), which peaks for NC-DIS events, due to momentum conservation, at twice the initial electron energy. For photoproduction events, which are defined though the absence of a detected electron, this distribution peaks at twice the energy of the exchanged photon, which is lower than in DIS. In addition to the $E - P_z$ distribution, the detection of a scattered electron in the calorimeter can further eliminate this type of events. Charged current deep inelastic scattering events are effectively cut out by the requirement that the missing transverse momentum of an event not exceeds a certain optimised threshold. Missing transverse momentum is caused by the undetected escape of the neutrino originating from the initial vertex.

6.2 Online Event Selection

The next paragraphs give a a short description of the selection criteria applied at each level of the trigger system as introduced in section 3.2.4.

6.2.1 First Level Trigger

To get selected by the FLT the following loose criteria had to be fulfilled:

- One out of four Calorimeter FLT energy thresholds must be exceeded. These are: a total calorimeter energy greater than 15 GeV, a total electromagnetic calorimeter energy greater than 10 GeV, an electromagnetic energy in the RCAL greater than 2 GeV and an electromagnetic energy in the BCAL greater than 3.4 GeV. The calculation of the sums for the first three thresholds given are performed excluding the 3 inner rings around the FCAL and the inner-most ring around the RCAL beam pipe. The term inner ring refers to the calorimeter towers in the F and RCAL which are closest to the beam pipe.

- The events are required to have at least one good track found by the CTD-FLT coming from the nominal interaction region, -50 cm $< z_{vertex} <$ $+80$ cm.

- In addition, several vetoes have to be passed. A veto is issued if the timing signal from the two C5 counters is not consistent with an *ep*-physics event in the central region of the detector, a coincidence in the outer and inner veto wall is observed indicating a interaction outside of the detector, or the SRTD timing is consistent with a beam-gas initiated event.

6.2.2 Second Level Trigger

The second level trigger decision is based on the "high$-E_T$" trigger. The requirements for this trigger are a $z-$vertex within -60 cm to $+60$ cm around the nominal interaction point, the value of $E-P_z$ has to be greater than 8 GeV and less than 75 GeV, the sum of the transverse energies of all calorimeter cells excluding the inner ring around the FCAL beam pipe has to be above 8 GeV and $E-P_z$ has to be either greater than 12 GeV or the ratio P_z/E less than 0.95. While the first $E-P_z$ requirement ensures enough hadronic activity to fulfill the high$-E_T$ condition, the latter removes beam-gas introduced events, where all the energy is deposited in the forward direction. In addition, events are vetoed at the SLT if only 1 PMT in the calorimeter gave a significant signal. $E-P_z$ distributions are shown in figure 5.1.

6.2.3 Third Level Trigger

The third level trigger performs an extensive reconstruction using algorithms identical to the ones used in the offline reconstruction of the events. Before trigger decisions are taken, the input events are subjected to background reduction algorithms. Events are vetoed at the TLT e.g. if a CAL spark candidate was found, if the CAL timing was consistent with a non-*ep*-physics event, or if the event was initiated by a cosmic or a halo muon.

A calorimeter EMC or HAC cell is defined as a spark candidate if there is a large energy imbalance between its two photomultipliers:

$$E_L + E_R > 1.5 \text{ GeV and } |(E_L - E_R)/(E_L + E_R)| > 0.9, \tag{6.1}$$

where E_L and E_R are the left and right photomultiplier PMT energies. Events are thus rejected if they contain at least a single spark candidate and little other calorimeter energy (less than 2 GeV).

Calorimeter timing is used to reject beam-gas events and cosmic and halo muon events. A weighted average time is calculated for the RCAL and FCAL as well as for the CAL as whole, using energy signals above 200 MeV and excluding photomultipliers from the bad channel list. Suspicious photomultipliers, which are paired to another good PMT, are kept when the energy imbalance as defined in the equation 6.1 is less than 0.2. For each PMT, a time is calculated with a parametrised error given by

$$\sigma_i(\text{ns}) = 0.4 + \left(\frac{1.4}{E_i(\text{GeV})}\right)^{0.65}. \tag{6.2}$$

The time average for a certain region X is then given by

$$t_X = \sum_i \left(t_i/\sigma_i^2\right) / \sum_i \left(1/\sigma_i^2,\right) \tag{6.3}$$

with error

$$\sigma_{t_X} = \left(\sum_i \left(1/\sigma_i^2\right)\right)^{-1/2}, \tag{6.4}$$

where the sums are over the PMT's in the considered region. Two PMT's have to be above the threshold and a minimum energy of least 1 GeV in the RCAL or BCAL and

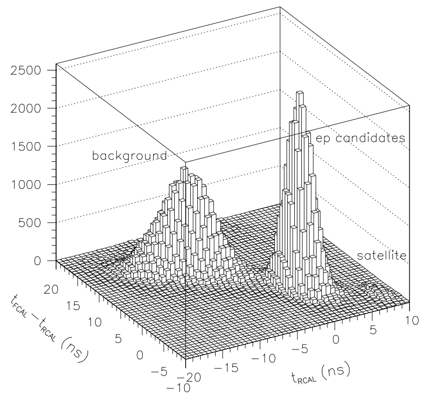

Figure 6.1: *Timing distributions for background and ep physics candidates at the TLT.*

2 GeV in the FCAL have to present for the timing calculations. Events are rejected if any of the following condition is fulfilled:

$$t_{RCAL} < \min(-6\text{ns}, -3\sigma_{t_{RCAL}}) \tag{6.5}$$

$$t_{RCAL} > \max(+6\text{ns}, +3\sigma_{t_{RCAL}}) \tag{6.6}$$

$$t_{FCAL} < \min(-8\text{ns}, -3\sigma_{t_{RCAL}}) \tag{6.7}$$

$$t_{FCAL} > \max(+8\text{ns}, +3\sigma_{t_{RCAL}}) \tag{6.8}$$

$$t_{FCAL} - t_{RCAL} < \min(-8\text{ns}, -3\sqrt{\sigma^2_{t_{RCAL}} + \sigma^2_{t_{FCAL}}}) \tag{6.9}$$

$$t_{FCAL} - t_{RCAL} < \max(+8\text{ns}, +3\sqrt{\sigma^2_{t_{RCAL}} + \sigma^2_{t_{FCAL}}}) \tag{6.10}$$

$$t_{CAL} < \min(-8\text{ns}, -3\sigma_{t_{CAL}}) \tag{6.11}$$

$$t_{CAL} > \max(+8\text{ns}, +3\sigma_{t_{CAL}}) \tag{6.12}$$

An example of a timing distribution at the TLT level can be seen in figure 6.1. CAL timing cuts are not applied to the Monte Carlo events.

Cosmic and halo muons are identified based on the correlation of the time and position of energy deposits in the calorimeter. In addition the algorithm uses information from the muon chambers. This algorithm is also not used for Monte Carlo events.

In addition to the above mentioned TLT cuts, the events are subject to further common filters to select photoproduction events. A z-vertex is required within $\pm$ 60 cm from the nominal interaction point. The value of $E - P_z$ has to be below 75 GeV and the number of bad tracks has to be less than 6. A track is considered bad, if it has a p_T greater than 0.2 GeV, passes more than 3 superlayers of the CTD but does not point towards the interaction vertex.

Events are considered photoproduction dijet candidates if at least one of the different jet algorithms applied to the energy deposits of the calorimeter found at least two jets with $\eta^{jet} < 2.5$ and $E_T^{jet} > 4$ GeV.

6.2.4 Online Event Selection Efficiency

To study the efficiency of the trigger selection chain as a whole, the HERWIG Monte Carlo was used. The efficiency is defined as the number of events generated and selected divided by the number of generated events. A generated event is one which fulfills the cross section criteria at the hadron-level, which are given in section 2.4. The upper plot in figure 6.2 shows the efficiency of the trigger system as function of the z-vertex. As expected the trigger system is highly efficient around the nominal interaction point. Over a wide range the trigger efficiency is better than 98%. The lower plots in figure 6.2 shows the efficiencies of the trigger selection as function of the transverse energy of highest E_T hadron-level jet, on the left hand side without an additional cut, on the right hand side with an additional vertex cut of $|z_{vertex}| < 40$ cm as applied offline on the final sample.

Displayed in the lower part of figure 6.3 is the efficiency of the trigger selection as function of the variable y_{JB}, calculated using only calorimeter information, with an additional vertex cut applied again. Since this analysis covers the kinematical range $0.20 < y < 0.85$, see section 2.4, the degrading efficiency at higher y_{JB} seems to be problematic. That it however does not pose a problem can be inferred from the upper plot in figure 6.3, which shows the correlation between y_{JB} and y_{true}. Shown are the mean values of the reconstructed y_{JB} as function of y_{true}. The vertical error bars indicate the resolutions. The line

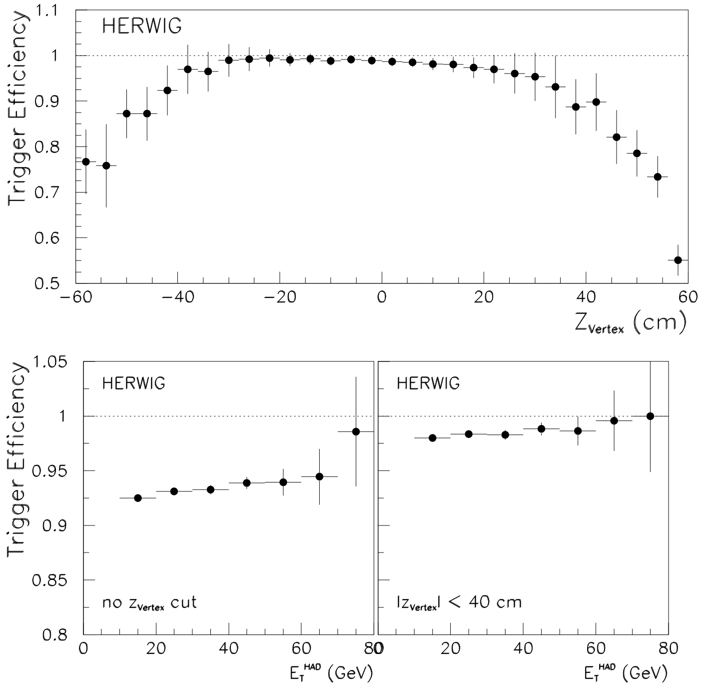

Figure 6.2: *Trigger efficiencies, shown as function of the vertex and as function of the transverse energy of the highest E_T hadron-level jet.*

is a straight line fit, for which the parameters are stated in the plot, too. As can be seen, the upper limit of the y_{true} range with $y_{true} \approx 0.85$ corresponds to a mean measured value of about 0.66 for y_{JB}. At this value the efficiency as function of y_{JB} is still very high. Since the fully corrected y_{JB} will be calculated using energy-corrected ZUFOs, which, as was shown in figure 5.12, removes the bias in the reconstruction of y_{JB}, a good efficiency over the full used range in y from 0.2 to 0.85 is achieved.

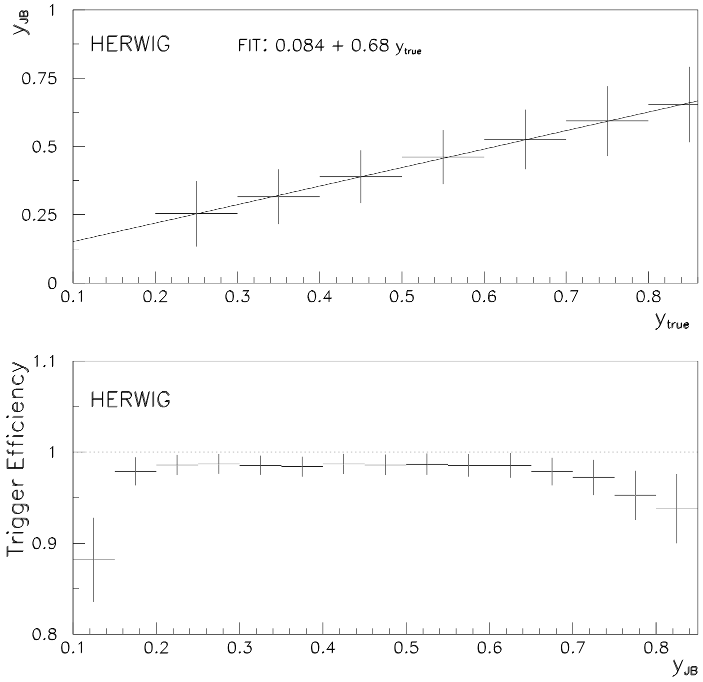

Figure 6.3: *Shown in the lower plot is the trigger efficiency as a function of y_{JB}, the upper plots shows the relation between y_{true} and y_{JB} together with a straight line fit.*

6.3 Offline Event Selection

In addition to the online selection criteria, the fully corrected data has to comply to other criteria. These criteria are chosen to optimise the reduction of non-photoproduction events and are discussed below.

To reduce the number of events from beam-gas, halo or cosmic interactions a tighter cut is applied on the z-vertex of the events, requiring

$$-40 \text{ cm} < z_{Vertex} < +40 \text{ cm}. \tag{6.13}$$

The motivation for this cut is based on the z-vertex distribution as shown in figure 6.4.

The simulation of the Monte Carlo z-vertex distribution contains information from the experimentally measured vertex distribution for the given year and hence compares well with the vertex distribution from data. The distribution is well fitted by a gaussian plus a constant. The width of the gaussian is about 12 cm. The distribution starts to deviate from a pure gaussian at about $\pm$ 30 $\sim$ 35 cm. The cut of $\pm$ 40 cm ensures that more than 3 σ of the distribution coming from nominal ep physics is contained in the selected region, while keeping non-ep background events out of the sample.

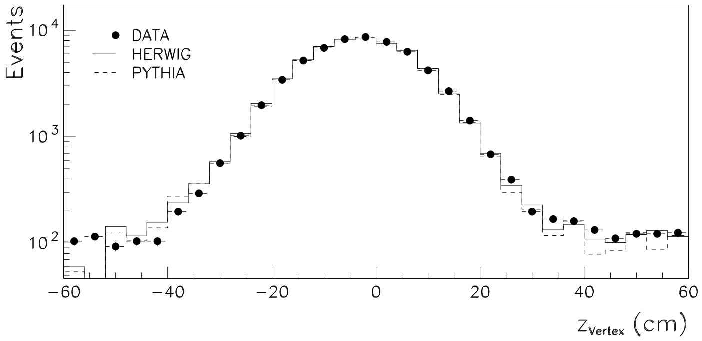

Figure 6.4: *Comparison of the vertex distribution as seen in data and Monte Carlo.*

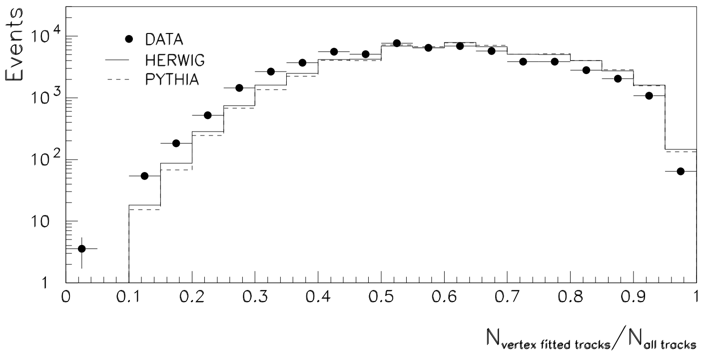

Figure 6.5: *Comparison of the ratio of vertex fitted to non-vertex fitted tracks as seen in data and Monte Carlo.*

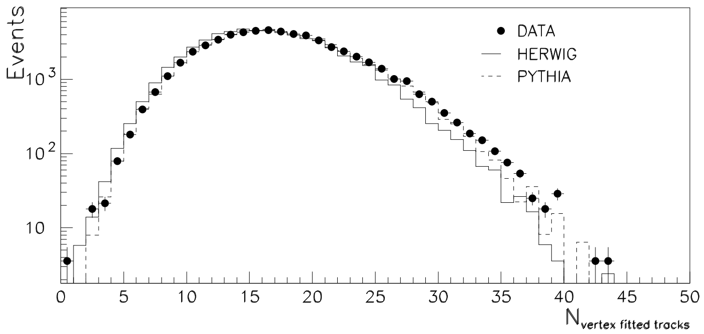

Figure 6.6: *Comparison of number of the vertex fitted tracks as seen in data and Monte Carlo.*

A discrepancy in the distribution of the ratio of tracks fitted to the primary vertex over all tracks found in an event between data and Monte Carlo exists as can be seen in figure 6.5. This discrepancy is not as pronounced in the distribution of the number of tracks matched to the primary vertex, as shown in figure 6.6. The origin of the discrepancy of the first mentioned distribution is the existence of a large number of ghost tracks in the data. To remove events where the tracks are dominated by ghost tracks, a cut is applied on the ratio of tracks;

$$\frac{\text{number of primary vertex fitted tracks}}{\text{number of tracks}} > 0.1 \,. \tag{6.14}$$

To reject background from NC-DIS a electron finder is applied to the events. In case a scattered electron candidate is found with an energy E'_e above 5 GeV, the value of y is calculated based on this electron information using the formula:

$$y_{elec} = 1 - \frac{E'_e}{2E_e}\,(1 - \cos\theta'_e)\,, \tag{6.15}$$

where θ'_e is the scattering angle of the scattered electron candidate. A comparison of the y_{elec} distribution for data, NC-DIS Monte Carlo and photoproduction Monte Carlo is shown in figure 6.7. The NC-DIS events were subject to the same selection cuts as in the photoproduction data and MC samples, except for the cut on y_{elec} itself. Good agreement between data and the photoproduction Monte Carlos is found for values above approximately 0.7. At lower values of y_{elec} the NC-DIS events dominate. The photoproduction events tend to have a high value of y_{elec} peaking at 1. Events are rejected when:

$$y_{elec} < 0.85, \tag{6.16}$$

resulting in an estimated background left in the sample of less than 1%.

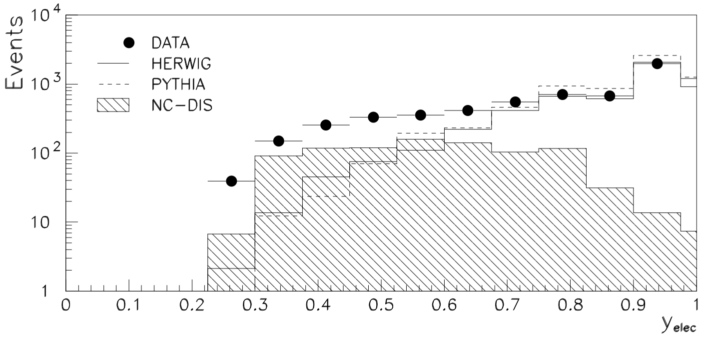

Figure 6.7: *Comparison of the y_{elec} distribution as seen in data and Monte Carlo. The different MC samples are normalised to the luminosity of the 1996/1997 data sample.*

To reject NC-DIS events without a reconstructed electron in the final state, a cut on the variable y_{JB}, calculated using the energy-corrected ZUFOs, was applied. Shown in figure 6.8 are the distributions for data, photoproduction and NC-DIS Monte Carlos for y_{JB}. The photoproduction Monte Carlos describe the distribution up to high values of y_{JB}. The deviation is clearly attributed to NC-DIS events, which peak at about 1 for these events. The cut on the y_{JB} variables used for the rejection of NC-DIS and for beam gas events with usually low y_{JB} values was

$$0.2 < y_{JB} < 0.85\ . \tag{6.17}$$

The implementation of these cuts places a constraint on the virtuality of the exchanged photon $Q^2 < 1$ GeV^2, with a median Q^2 of 10^{-3} GeV^2. It also defines the center-of-mass energy of the photon-proton system $W_{\gamma p}$ (see equation 2.2 to be within the range 134 GeV $< W_{\gamma p} <$ 277 GeV.

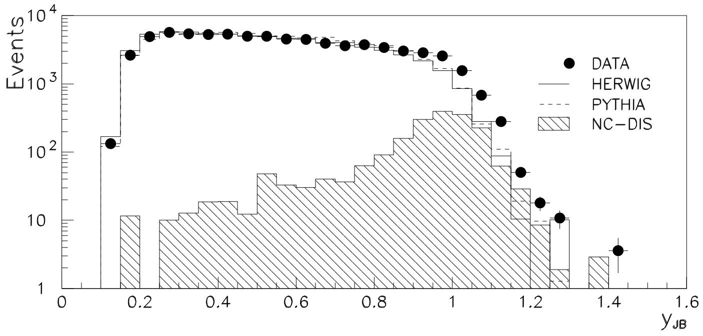

Figure 6.8: *Comparison of the y_{JB} distribution as seen in data and Monte Carlo*

The rejection of charged current deep inelastic scattering events is based on the missing transverse momentum $\not{P}_T$, carried away by the undetected neutrino. To take into account the energy resolution of the calorimeter, this quantity is scaled with the inverse square root of the sum of the deposited energy. In figure 6.9 the $\not{P}_T/\sqrt{E_T}$ distribution is shown for the data, photoproduction and charged current deep inelastic scattering Monte Carlos. The cut was chosen [97] to be

$$\frac{\not{P}_T}{\sqrt{E_T}} < 1.5\sqrt{\text{GeV}}\ . \tag{6.18}$$

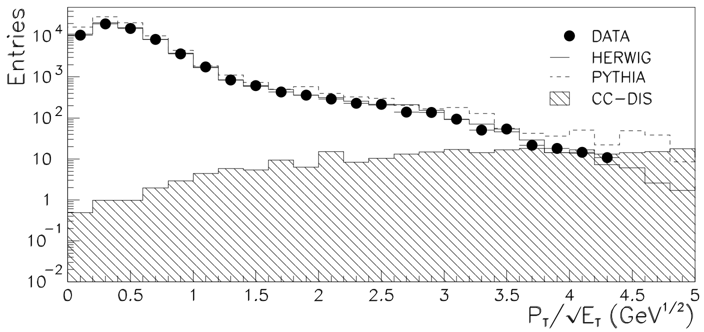

Figure 6.9: *Comparison of the missing p_T distribution as seen in data and Monte Carlo.*

The events of the selected sample of dijet candidates were subject to the k_T clustering jet algorithm as described in section 2.2.1. A total of 61798 events with at least two jets were selected, fulfilling the requirements

- $-1 < \eta^{jet} < +2.4$,
- $E^{jet}_{T,leading} > 14$ GeV, where $E^{jet}_{T,leading}$ is the transverse energy of the highest transverse energy jet,
- and $E^{jet}_{T,second} > 11$ GeV, where $E^{jet}_{T,second}$ is the transverse energy of the second highest transverse energy jet.

Examples of candidates for resolved and direct dijet events are shown in figure 6.10 and 6.11. Both events are clear dijet events with a back-to-back topology in the transverse x-y plane. The candidate for resolved photoproduction with $x^{OBS}_{\gamma} = 0.744$ has some hadronic energy deposited near the beam pipe in the RCAL. This energy is associated with the photon remnant. The direct photoproduction candidate has a value x^{OBS}_{γ} of 0.947.

6.4 Comparison of Data and Monte Carlo

The next section studies the performance of the description of the data by the used Monte Carlo models. The same online and offline cuts were applied to the Monte Carlo events. All distributions shown are determined using the energy-corrected ZUFOs as described in section 5.6. In the determination of cross sections from data using Monte Carlo based correction factors, a further correction term is applied on the MC events only. This correction term is determined from figure 5.15 and consists of adding an extra term to the transverse energy of the jets depending on the initial transverse energy of the jet. The motivation is to zero the difference between data and MC as seen in figure 5.15. The correction terms used are given in table 6.1.

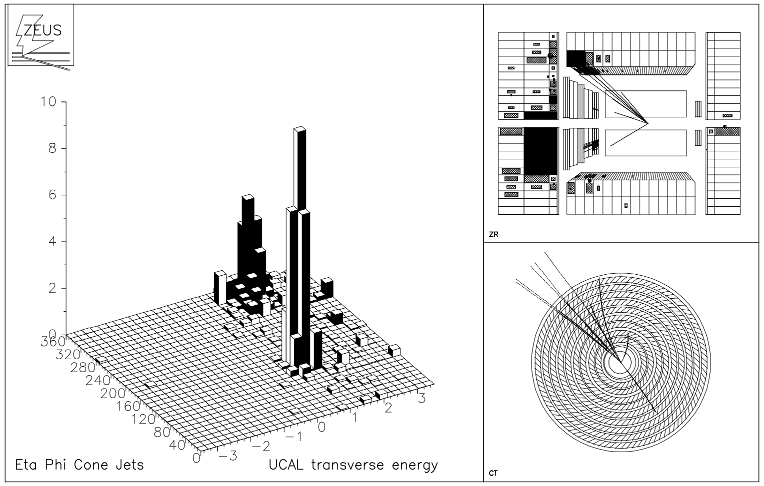

Figure 6.10: *A Candidate for a resolved photoproduction event. Shown on the left hand side is a 3D plot of the deposited energies in the calorimeter cells versus the azimuthal angles ϕ and the pseudorapidity η of the cells. Positive η corresponds to the FCAL region where some energy deposits can be seen originating from the proton remnant. In the η range from 1 to 2, two clear separated energy accumulations can be seen corresponding two the two jets found in the event. The upper right hand side plot shows the detector components used (CAL and CTD) in this analysis in a r-z projection. Indicated as black lines are the tracks reconstructed by the reconstruction software and the measured energy deposits which are also seen at the right hand side. The lower part of the right hand side shows a CTD projection into the x-y plane and the reconstructed tracks. The reconstructed x^{OBS}_{gamma} is 0.7444.*

6.4.1 Transverse Energy Flow

As discussed in chapter 4 in resolved photoproduction events, the possibility of multiple-parton interaction (MI) is considered. These multiple-parton processes cause additional transverse energy in the final state, which can enter as a pedestal-like energy in the determination of the transverse energy of the jets. Previous analysis of jet photoproduction performed at ZEUS ([28], [29], [67], [68],[116]) found an excess of events with respect to Monte Carlo prediction for low x^{OBS}_{γ} values, which translates into forward-going jets. This is seen in figure 6.12, where a comparison of the 1994 data x^{OBS}_{γ} distribution with different Monte Carlos with and without MI is shown. The measurement is performed

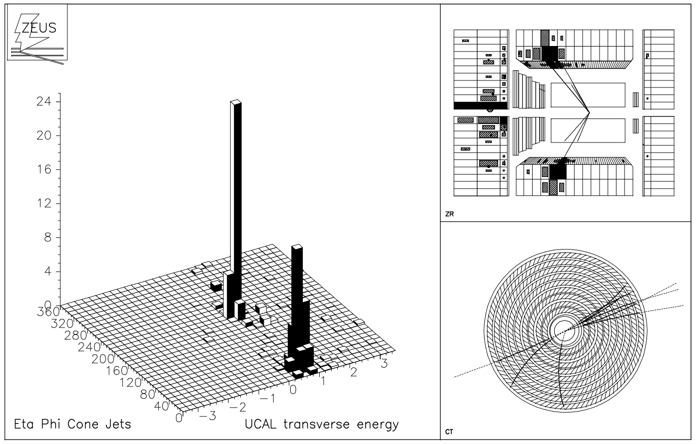

Figure 6.11: *A Candidate for a direct photoproduction event. The reconstructed x_{gamma}^{OBS} is 0.947. The explanation of the different views of the detector is given in figure 6.10*

Energy range [GeV]	HERWIG [%]	PYTHIA [%]
$10 < E_T^{jet} < 15$	0.21	0.18
$15 < E_T^{jet} < 19$	0.38	0.31
$19 < E_T^{jet} < 23$	0.76	0.60
$23 < E_T^{jet} < 27$	1.34	1.08
$27 < E_T^{jet} < 31$	1.31	1.11
$31 < E_T^{jet} < 35$	1.05	0.71
$35 < E_T^{jet} < 39$	1.03	0.68
$39 < E_T^{jet} < 90$	0.86	0.63

Table 6.1: *Monte Carlo transverse energy correction as function of E_T^{jet} for the HERWIG and PYTHIA Monte Carlo. The relative corrections are given in percent.*

with jets of transverse energy greater than 6 GeV. The excess at low x_γ^{OBS} values is partly compensated when including multiple-parton interaction in the Monte Carlo. In figure 6.13 the transverse energy flow around the jet is shown in bins of η^{jet} and E_T^{jet} for

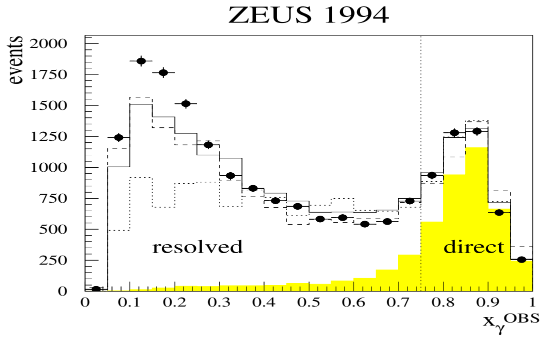

Figure 6.12: *The x_γ^{OBS} distribution from the 1994 dijet analysis. The data (dots) are compared to HERWIG without MI (dotted histogram) and HERWIG (full histogram) and PYTHIA (dashed histogram) with MI. The figure is taken from [116].*

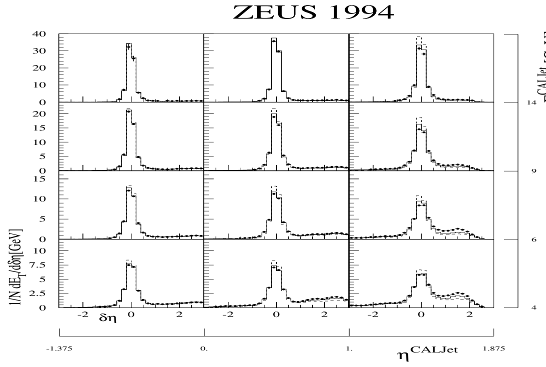

Figure 6.13: *Transverse energy flow around jets from the 1994 dijet analysis. The transverse energy is integrated over $|\Delta\phi| < 1$ and shown in bins of the pseudorapidity and the transverse energy of the jet. The data (dots) are compared to HERWIG with (full histogram) and without (dashed histogram) MI. The figure is taken from [116].*

jets of transverse energy greater than 4 GeV. The transverse energy flow is defined to be

$$\frac{1}{N}\frac{dE_T}{d\Delta\eta}, \tag{6.19}$$

where $\Delta\eta$ is the difference in η of the jet and the calorimeter cell or ZUFO, respectively. Only calorimeter cells or ZUFOs within a distance of $\Delta\phi$ less than 1 to the jet are considered to ensure the rejection of contributions of transverse energy from the other jet. The transverse energy flow distributions show an excess of the data over the Monte Carlo predictions, even for the Monte Carlo with MI, for low energy and forward going jets. This excess vanishes as the transverse energy of the jet is raised. The 1994 dijet analysis [67] demonstrated that Monte Carlos with inclusion of multiple-parton interactions gives a better description of the data in the regions most sensitive to these effects, which are low transverse energy and very forward going jets. The comparable x_γ^{OBS} distribution for the 1996/1997 data used in this thesis to the one shown in figure 6.12 is given in figure 6.14. No significant excess at low x_γ^{OBS} is seen for data. The best description at low x_γ^{OBS} is given by HERWIG, which here does not include multiple-parton interactions. The transverse energy flow distributions for the 96/97 data to be compared to the ones given in figure 6.13 are given in figure 6.15 and figure 6.16 in a linear and a logarithmic scale, respectively. The latter is shown for clarity. The binning in η differs from figure 6.13 to cover the full η-range of this analysis. Comparing the central bins of figure 6.15 with figure 6.13, which have the same η range, a clear improvement is seen with the increase in the transverse jet energy. The transverse energy flow in the very forward η bin with $1 < \eta < 2.4$ shows a discrepancy, which can be better seen in the logarithmic scale in figure 6.16. Again the difference in the distribution diminishes with increasing transverse jet energy. The HERWIG Monte Carlo gives a better description of the data once more.

In figure 6.17, the transverse energy flow is shown in bins of x_γ^{OBS} and E_T^{jet}. As expected, the Monte Carlo description is worse for low x_γ and low E_T^{jet} values, improving with an increase in the value of these variables. Again the HERWIG Monte Carlo without MI is slightly better than the PYTHIA Monte Carlo with MI. The overall better description of the transverse energy flow by the HERWIG Monte Carlo even without inclusion of the multiple-parton interaction might indicate that the origin of the discrepancy between data and Monte Carlo is not coming from multiple-parton interaction alone. In the kinematic phase space of high E_T^{jet} used in this analysis multiple-parton interaction do not form an obstacle in the extraction of cross sections.

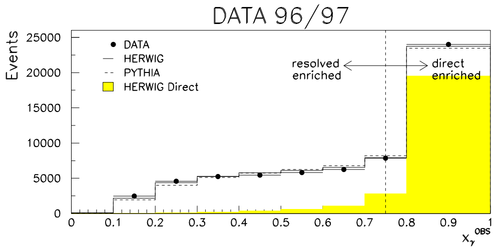

Figure 6.14: *Comparison of the x_γ^{OBS} distribution as seen in data and Monte Carlo. Shown is the uncorrected measured x_γ^{OBS} distribution for 96/97 data and for the HERWIG and PYTHIA Monte Carlo. The shaded histogram is the direct component for HERWIG. The line at $x_\gamma^{OBS} = 0.75$ separates the region called resolved enriched and direct enriched.*

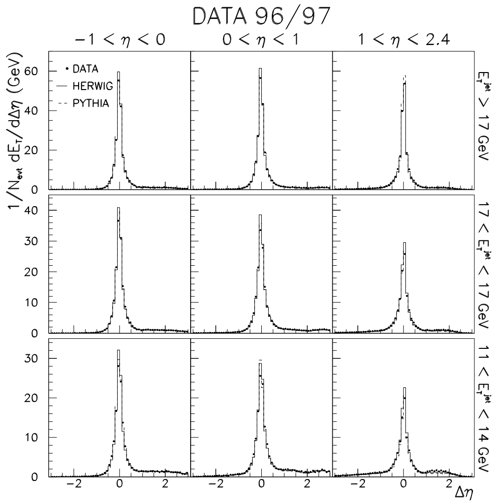

Figure 6.15: *Comparison of transverse energy flow for the 96/97 data with Monte Carlo in bins of η and E_T^{jet} in a linear scale.*

6.4.2 General Distributions

Figure 6.18, 6.19 and 6.20 show distributions of kinematical variables which are used in the determination of the cross sections.

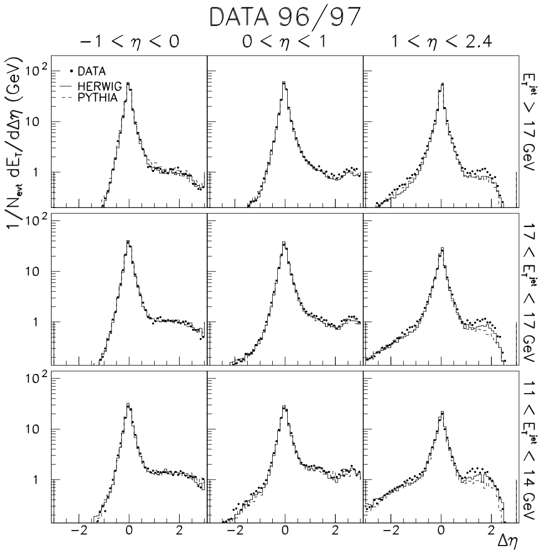

Figure 6.16: *Comparison of transverse energy flow for the 96/97 data with Monte Carlo in bins of η and E_T^{jet} in a logarithmic scale. Shown is the same data as in figure 6.15*

Shown at the top of figure 6.18 are the E_T^{jet} distributions of the highest and second highest in the transverse energy of the jets, within the selected η range, named leading and second, respectively. At the bottom, the distributions of the average and the difference in the transverse energy of the two highest transverse energy jets are illustrated. While the $E_{T,\mathrm{leading}}$ and the average E_T distributions are well modeled for both HERWIG and PYTHIA, the $E_{T,\mathrm{second}}$ and the difference in the transverse energies is described better by the PYTHIA Monte Carlo. The discrepancy in the $E_{T,\mathrm{second}}$ distribution between data and HERWIG, with HERWIG having in general higher transverse energies for the second jet, is the origin for the discrepancy in the ΔE_T distribution.

In figure 6.19, the η distributions for the leading and second jets as well as the average η and difference in η are displayed. None of the two Monte Carlos agree over the full η range for both leading and second jets. While PYTHIA describes the η distribution of

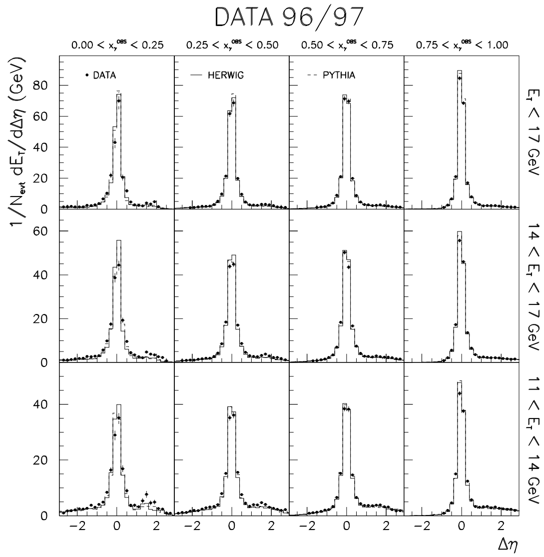

Figure 6.17: *Comparison of transverse energy flow for the 96/97 data with Monte Carlo in bins of x_γ^{OBS} and E_T^{jet}.*

the leading jet better from the rear up to η of about 1.5, HERWIG starts to deviate from the data distribution at η of about 1. For forward leading jets with $\eta > 1.5$, both Monte Carlos underestimate the number of events. For the second jet, this behaviour changes and HERWIG is describing the data distribution up to η of about 2. PYTHIA overestimates the number of events with the second jet going into the backward direction, corresponding to an η range of approximately -0.5 to 0, and underestimates in the forward region of $0.6 < \eta < 1.6$. In the very forward direction with $\eta > 2$, HERWIG overestimates the data distribution. The deviations in the description of the data for the two η distributions are almost canceled in the average $\bar{\eta}$ of the two jets as seen at the lower left. The latter is important since the measurement of the $\cos\theta^*$ cross sections depends on a cut on this variable. The lower right plot shows the difference in η of the two selected jets, $\Delta\eta$, which is well described by HERWIG and underestimated for $\Delta\eta < 1$ in PYTHIA.

In figure 6.20, the x_γ^{OBS} and x_p^{OBS} are shown at the top. The x_p^{OBS} distribution lies

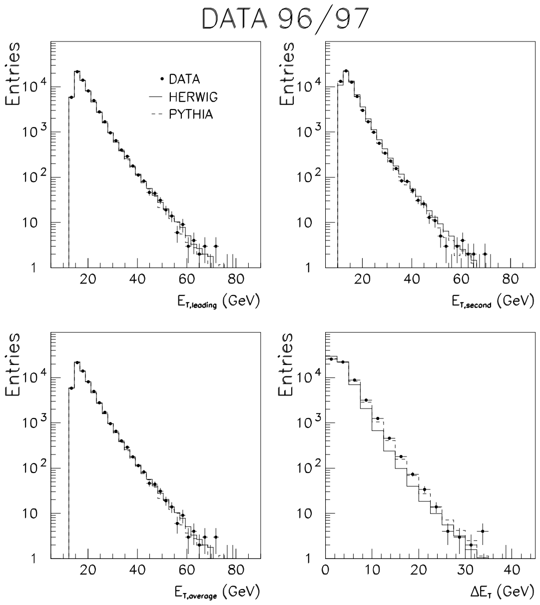

Figure 6.18: *Comparison of the E_T^{jet} distributions as seen in data and Monte Carlo. At the top left the E_T^{jet} distribution for the leading jet in E_T^{jet}, the top right the same for the second jet. The bottom left is the average of the transverse energies of the two jets and the bottom right the difference of the transverse energies.*

between 10^{-2} and $10^{-0.5}$ (i.e. ≈ 0.32). The distribution is well described by the Monte Carlos. This reflects the fact that within the used x_p^{OBS} region, the structure functions of the proton are well measured. The lower limit of the distribution can be explained using the definition of x_p^{OBS} as given in equation 2.6 and stems from the transverse energy requirement of the jets. The upper limit reflects the fall in the parton densities towards high x in the proton. The x_γ^{OBS} is reasonably described by the Monte Carlo. The discrepancy for x_γ^{OBS} above 0.8 is caused by bin-to-bin migration: the resolution in x_γ^{OBS} is 0.05, which is just the bin width in the shown x_γ^{OBS} distribution. The distribution has to be compared to figure 6.14, where a larger bin size was chosen. In the lower right the invariant mass distribution of the two jets, M_{JJ}, is shown. For values of M_{JJ} above 25 GeV, a good description of the data distribution is given by both Monte Carlos. For

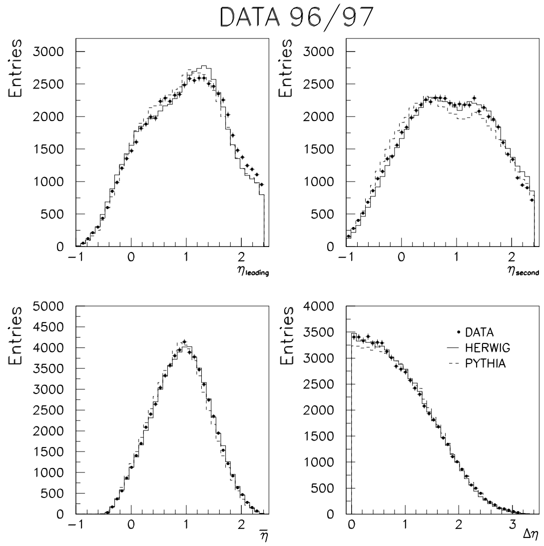

Figure 6.19: *Comparison of the η^{jet} distributions as seen in data and Monte Carlo.*

the measurement of the $\cos\theta^*$ cross sections, a cut of $M_{JJ} > 42$ GeV will be applied for reasons given below. The lower right part of the figure shows the scattering angle, $\cos\theta^*$, distribution in the center-of-mass of the dijet system. A reasonable description of the data is given by the Monte Carlos.

6.4.3 The $\cos\theta^*$ Distribution

To perform a unbiased measurement of the $\cos\theta^*$ cross sections, additional cuts have to be applied. The motivation of the cuts can be seen in figure 6.21. Given at the left hand side is a scatter plot of the invariant mass of the dijet system M_{JJ} versus $\cos\theta^*$, while at the right hand side the same is given for the average $\bar{\eta}$ of the two jets versus $\cos\theta^*$. Strong correlations are seen between these variables, which can be understood looking at the definitions of the variables as given in equation 2.7 and equation 2.9. The lines indicate the cuts performed in the determination of the $\cos\theta^*$ cross sections. The additional cuts

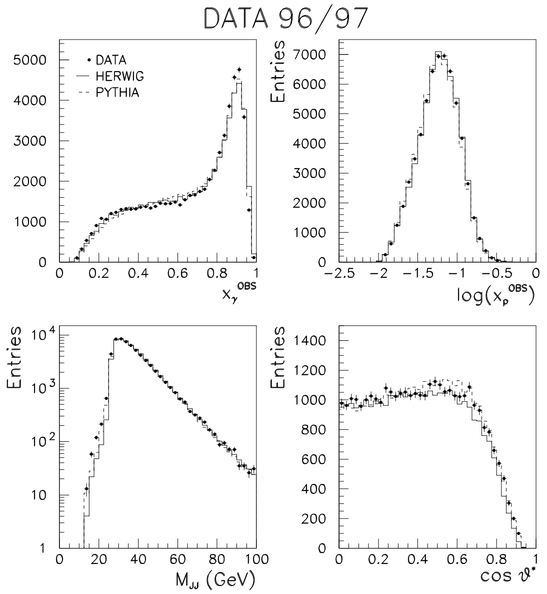

Figure 6.20: *Comparison of $x_\gamma^{OBS}, x_p^{OBS}, M_{JJ}$ and $\cos\theta^*$ distributions as seen in data and Monte Carlos.*

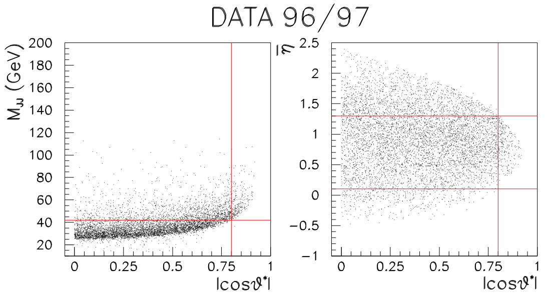

Figure 6.21: *Scatter-plots of M_{JJ} versus $\cos\theta^*$ and $\bar{\eta}$ versus $\cos\theta^*$. For clarity only a subsample of the 96/97 data is shown.*

are; $\cos\theta^* < 0.8$, $M_{JJ} > 42$ GeV and $0.1 < \bar{\eta} < 1.3$. On $\bar{\eta}$, which is the boost of the dijet system in the laboratory frame, a cut is applied to ensure that the phase space is uniform as function of $|\cos\theta^*|$, hence any shape seen in the measured distributions is caused by

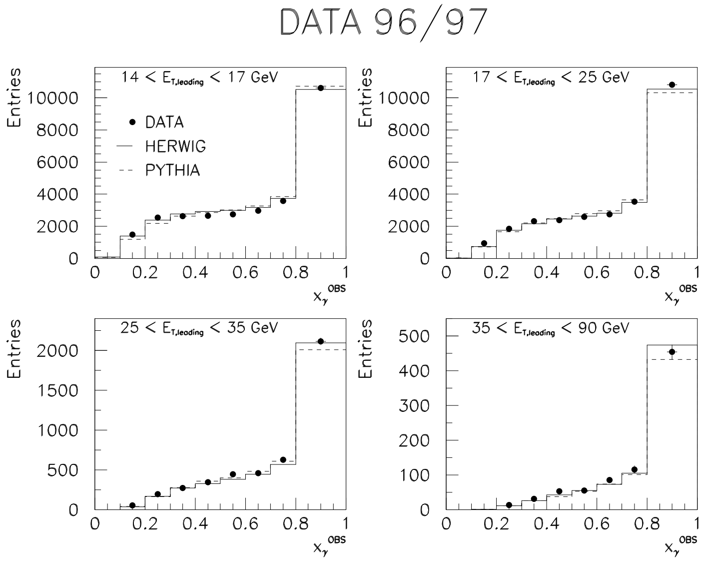

Figure 6.22: *Comparison of x_γ^{OBS} distribution of data and Monte Carlo in four different E_T^{jet} ranges.*

the dynamics of the process and not due to some bias from the cuts.

6.4.4 The Uncorrected Cross Sections

The following figures 6.22 and 6.24 - 6.28 show a comparison of the number of events seen in data with the Monte Carlo predictions from HERWIG and PYTHIA for detailed kinematical ranges. The number of events are shown in all the distributions for which the cross sections will be determined.

In figure 6.22, the number of dijet events is given as function of the fractional photon momentum x_γ^{OBS} in four different bins of E_T^{jet} of the leading jet. The bin width is taken to be about twice the resolution in the variable x_γ^{OBS}, except for x_γ^{OBS} values greater than 0.8 for which the last two bins are combined. The resolution in x_γ^{OBS} is shown in figure 6.23 at the right hand side together with a gaussian fit to the distribution. The

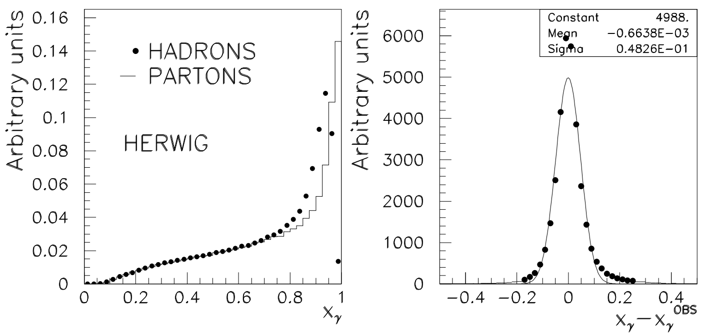

Figure 6.23: *On the left side, a comparison of the parton and the hadron x_γ distributions for dijet events fulfilling the kinematic criteria is given. At the right side the resolution in the variable x_γ^{OBS} is given, where x_γ is taken for the hadrons.*

parameters of the fit are givenm at the top of the picture. The combination of the last two bins is motivated by Monte Carlo studies. Comparing the x_γ distributions for dijet events with jets determined using firstly the partons of the hard scattering process and than the hadrons of the final hadronic state, a large hadronisation dependence for x_γ greater than 0.8 is found. This hadronisation dependence is seen in figure 6.23 at the left hand side. The combined bin minimises the hadronisation dependence, needed for a comparison to NLO calculations performed with partons.

In figure 6.24 and figure 6.25, the number of dijet events is given as function of the pseudorapidity of the second jet in four different ranges of E_T^{jet} and three different bins in η of the leading jet. The distributions are given for events with x_γ^{OBS} less than 0.75, the resolved enriched sample, and for events with x_γ^{OBS} greater 0.75, the direct enriched sample, respectively. To ensure infrared safety as discussed in section 2.4 each event is counted twice in these η distributions by interchanging the values of η_1^{jet} and η_2^{jet}. Given in figure 6.26 and figure 6.27 are the number of dijet events as function of the transverse energy of the leading jet, again separated for x_γ^{OBS} less and greater 0.75. The distributions are shown in six bins of η, with different combinations for the η requirements of the first and second jet.

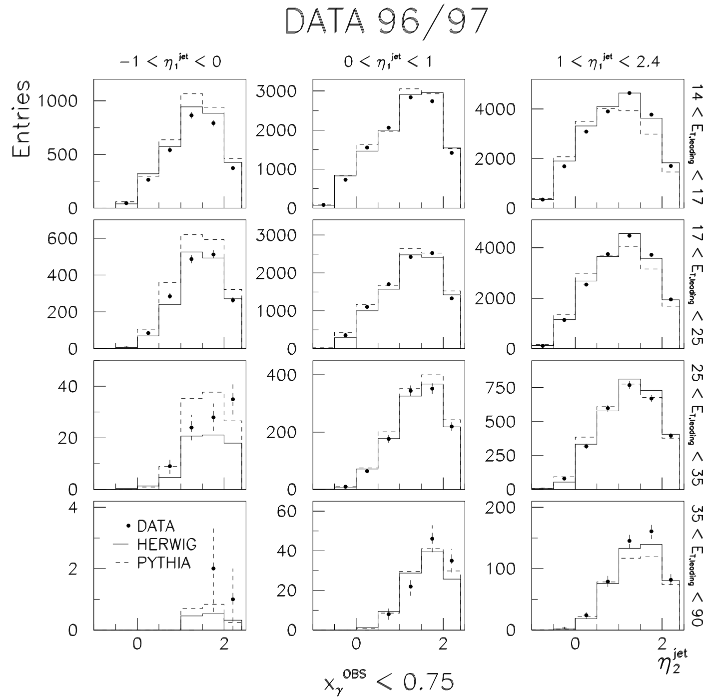

Figure 6.24: *Comparison of η_2^{jet} distributions of data and Monte Carlo in four different E_T^{jet} and three different η ranges of the leading jet for x_γ^{OBS} less than 0.75 (resolved enriched sample).*

The last comparison is shown in figure 6.28. The $\cos\theta^*$ distributions are given for four different bins in E_T^{jet} for the leading jet.

All comparisons show that both Monte Carlos describe the overall data reasonably well. The Monte Carlo used to determine purities, efficiencies (of which the definition will be given in the following chapter in equation 7.2 and 7.3) and systematic uncertainties was chosen to be the HERWIG Monte Carlo to take the sample with higher statistics. The PYTHIA Monte Carlo was only used to estimate model dependencies originating from the use of a different hadronisation model.

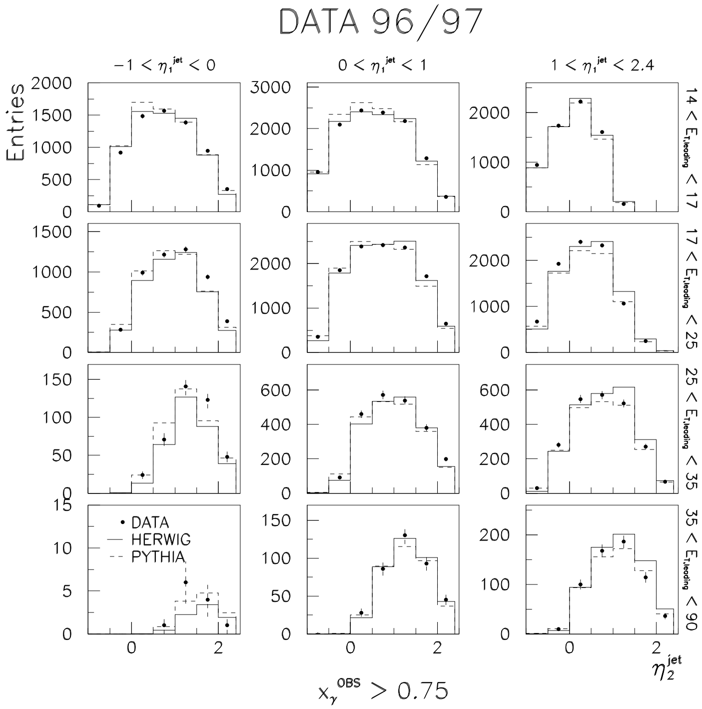

Figure 6.25: *Comparison of η_2^{jet} distributions of data and Monte Carlo in four different E_T^{jet} and three different η ranges of the leading jet for x_γ^{OBS} greater than 0.75 (direct enriched sample).*

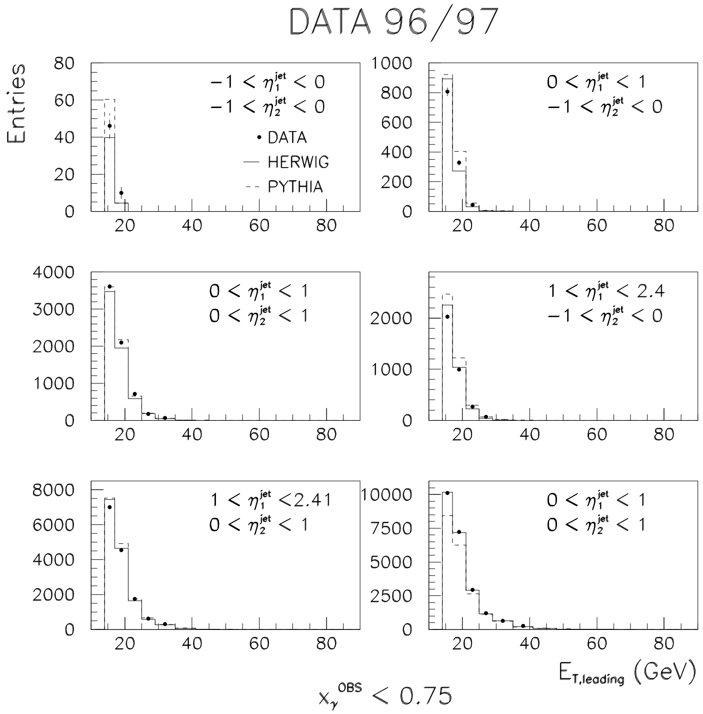

Figure 6.26: *Comparison of E_T^{jet} distributions of data and Monte Carlo of the leading jet in six different η bins for x_γ^{OBS} less than 0.75 (resolved enriched sample).*

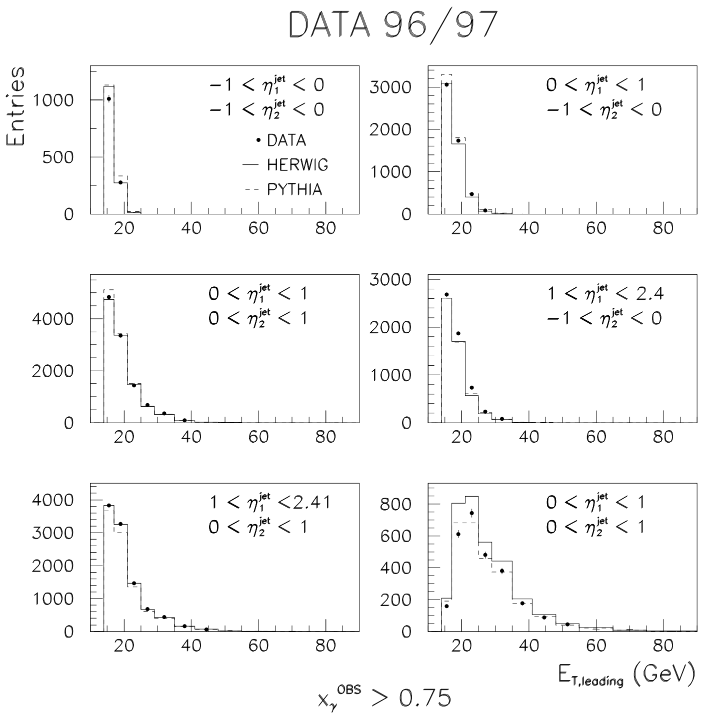

Figure 6.27: *Comparison of E_T^{jet} distributions of data and Monte Carlo of the leading jet in six different η bins for x_γ^{OBS} greater than 0.75 (direct enriched sample).*

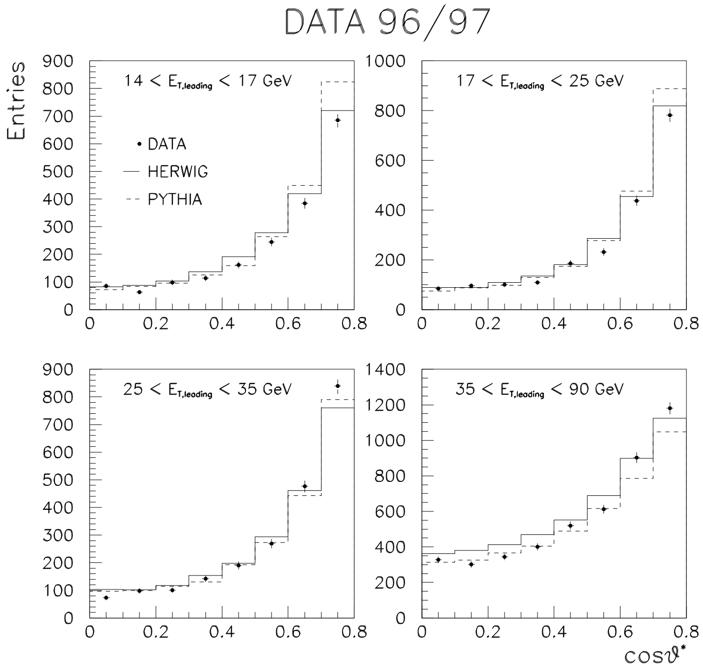

Figure 6.28: *Comparison of $\cos\theta^*$ distributions of data and Monte Carlo in four E_T^{jet} ranges of the leading jet.*

Chapter 7

Unfolding the Cross Sections

In the following chapter, the unfolding of the cross sections for the different measurements is introduced. The cross sections are determined from the quantities measured at the detector-level using corrected ZUFOs and further corrected back to the hadrons of the final state. No attempt is made to retrieve parton cross sections. The unfolding procedure and the estimates of the systematic uncertainties are discussed.

7.1 Unfolding Procedure

In order to measure cross section for jets of hadrons, a bin-by-bin unfolding method was used. To determine efficiencies and purities of the event selection the HERWIG Monte Carlo was used. In the bin-by-bin unfolding method the number of events in the data corrected to the hadron-level N_i^{hadron} in bin i is estimated from the number of events observed at the detector-level N_i^{data} in this bin using the formula:

$$N_i^{hadron} = N_i^{data} \left(\frac{\text{Purity}_i}{\text{Efficiency}_i} \right)_{MC} = N_i^{data} \left(\frac{N_i^{gen}}{N_i^{rec}} \right)_{MC}. \tag{7.1}$$

The efficiency of bin i is defined as the ratio of the number of events generated and reconstructed over the number of generated events in this bin;

$$\text{Efficiency}_i = \frac{N_i^{gen\&rec}}{N_i^{gen}}. \tag{7.2}$$

The purity of bin i is defined as the ratio of the number of events generated and reconstructed over the number of reconstructed events in this bin;

$$\text{Purity}_i = \frac{N_i^{gen\&rec}}{N_i^{rec}}. \tag{7.3}$$

The bin-by-bin unfolding method depends on an accurate description of the data by the Monte Carlo. In the case that this description is poor the correction for bin-to-bin migrations becomes model dependent. The PYTHIA Monte Carlo was used to estimate this model dependence since HERWIG was used for the extraction of the cross sections.

7.2 Determination of Systematic Uncertainties

In addition to the determination of the cross sections using the PYTHIA Monte Carlo to determine the model dependence, numerous variations of the unfolding procedure were done to estimate the systematic uncertainties of the cross sections. The following list summarises all variations studied.

- the PYTHIA Monte Carlo was used to study mainly the impact of the hadronisation model and the unfolding procedure,
- the HERWIG MC was used without normalisation factors (as defined in section 4.5.1) for the direct and resolved components,
- the cut on the absolute value of the vertex was changed from nominal 40 cm to 30 cm and 50 cm, respectively.
- the cut on the ratio of vertex fitted tracks to all tracks (vctrhl/vctpar in the following pictures) was changed from nominal 0.1 to 0 and 0.2,
- the cut on the missing transverse momentum was changed from nominal 1.5 GeV to $\frac{p_T}{\sqrt{E_T}} < 1.2$ GeV and $\frac{p_T}{\sqrt{E_T}} < 1.8$ GeV, respectively,
- the cut to reject DIS electron candidates was changed from nominal 0.85 to $y_{elec} < 0.8$ and $y_{elec} < 0.9$, respectively,

- the value of y_{JB} was varied by ± 2 %,
- the value of E_T of the jets was varied by ± 3 %,

The last two items are motivated by the fact that the measured values for y_{JB} and E_T^{jet} using energy corrected ZUFOs have a correlation with respect to the true values as can be seen in figure 5.12 for y_{JB} and figures 5.10 and 5.11 for E_T^{jet}. All the above stated variations have been applied both to Monte Carlo and data simultaneously.

- The influence of a possible hadronic scale difference between data and Monte Carlo was estimated varying the reconstructed jet energies and y_{JB} by $\pm$ 1.5% at the same time and by $\pm$ 1% separately. This variation needed only be performed for Monte Carlo.

The dependence of the cross sections to these variations are shown, for all bins used in the measurement of the cross sections, in figures 7.1 to 7.7. Each data point represents one variation for the given bin. The explanation for the points are given in figure 7.1.

The variation due to the energy scale uncertainties are strongly correlated from bin to bin. Hence the energy scale uncertainties are shown separately as a shaded band on the cross-section figures given in the chapter 8. The positive and negative fluctuations from the other variations for a given cross section are added in quadrature to give the total positive and negative systematic uncertainty.

Shown in figure 7.8, as an example, is the total systematic error for the differential cross sections in x_γ^{OBS} for the four different E_T^{jet} bins used in this analysis. The shaded band indicates the systematic error which is attributed to the energy scale uncertainty of the transverse energies of the jets. The error bars represent the other systematic uncertainties, which are added in quadrature.

7.2.1 Neutral current deep inelastic scattering Background Events

Most neutral current deep inelastic scattering events are removed from the dijet photoproduction sample by the offline selection criteria. Still some genuine dijet events or single jet events in which the scattered electron is taken as a jet will survive the cuts. To estimate the number of events which will remain in the selected dijet sample, a neutral current deep inelastic scattering Monte Carlo sample was subject to the same cuts as the dijet photoproduction samples. Since the HERWIG Monte Carlo used for the unfolding of the cross sections includes events up to $Q^2 = 4$ GeV^2, only NC-DIS events with $Q^2 >$ 4 GeV^2 were considered. 661 events (amounting to 1% of the total sample) were found to pass the cuts for the NC-DIS Monte Carlo sample when normalised to the combined 1996 and 1997 luminosity. The small number of events and the overall size of the systematic uncertainties does not require that these events are subtracted off for the determination of the cross sections.

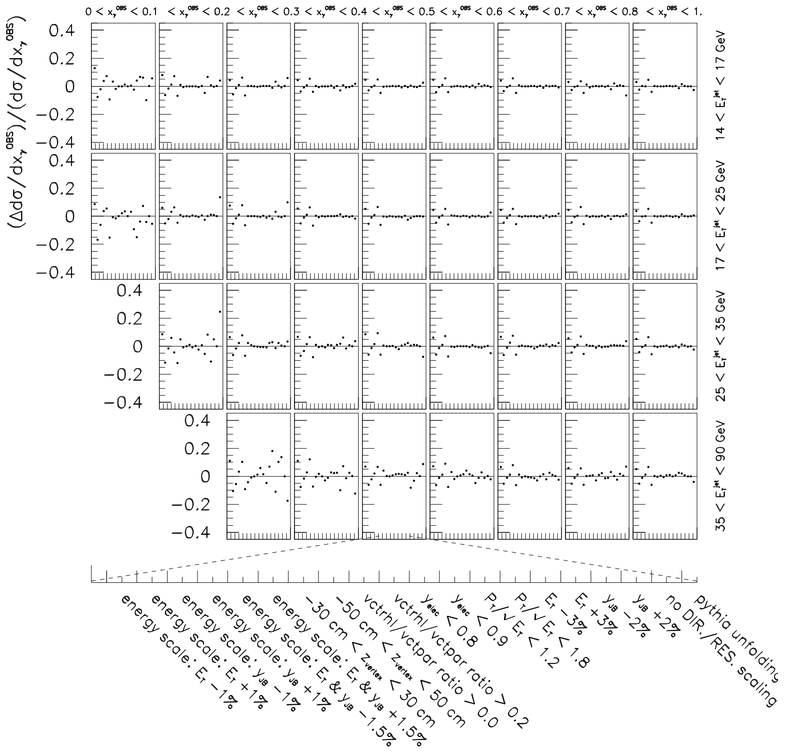

Figure 7.1: *The relative effect of various systematic variations in the analysis on the $d\sigma/dx_\gamma^{OBS}$ cross section for $0.20 < y < 0.85$.*

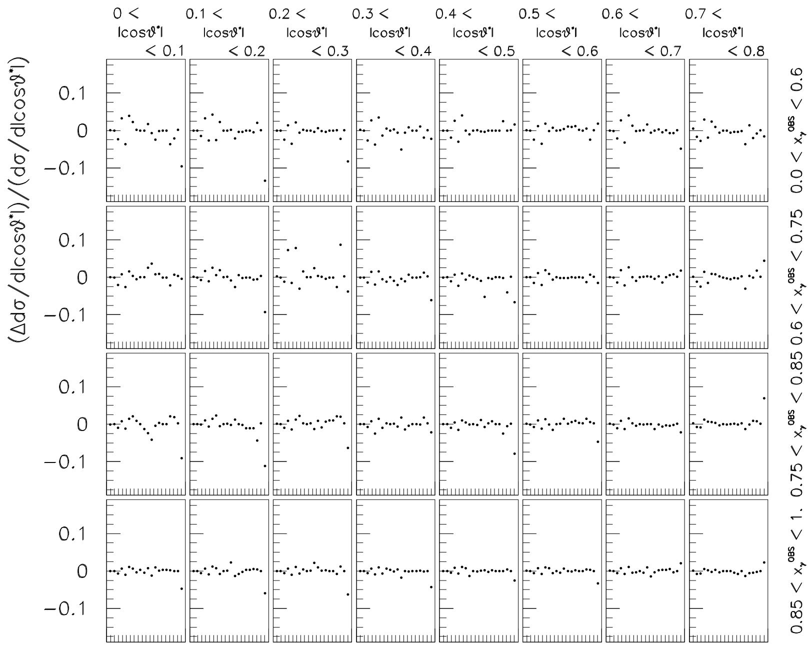

Figure 7.2: *The relative effect of various systematic variations in the analysis on the $d\sigma/d|\cos\theta^*|$ cross section for $0.20 < y < 0.85$. The points are in the same order as in figure 7.1*

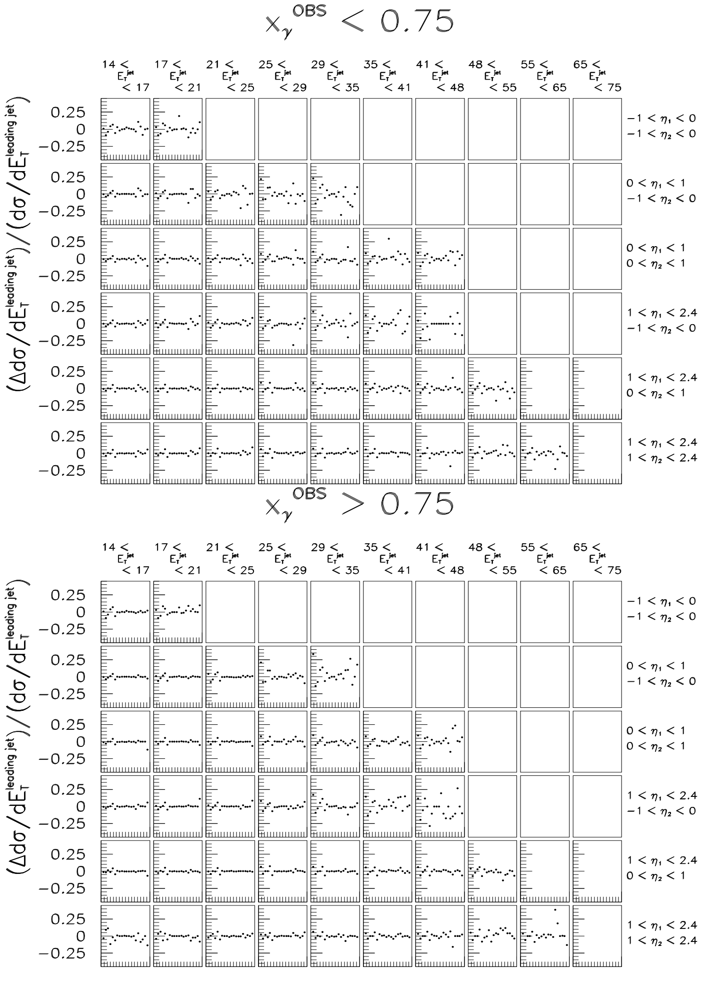

Figure 7.3: *The relative effect of various systematic variations in the analysis on the $d\sigma/dE_T^{leadingjet}$ cross section. Shown in the upper plot is the cross section for events with $x_\gamma^{OBS} < 0.75$, in the lower plot for $x_\gamma^{OBS} > 0.75$. The points are in the same order as in figure 7.1*

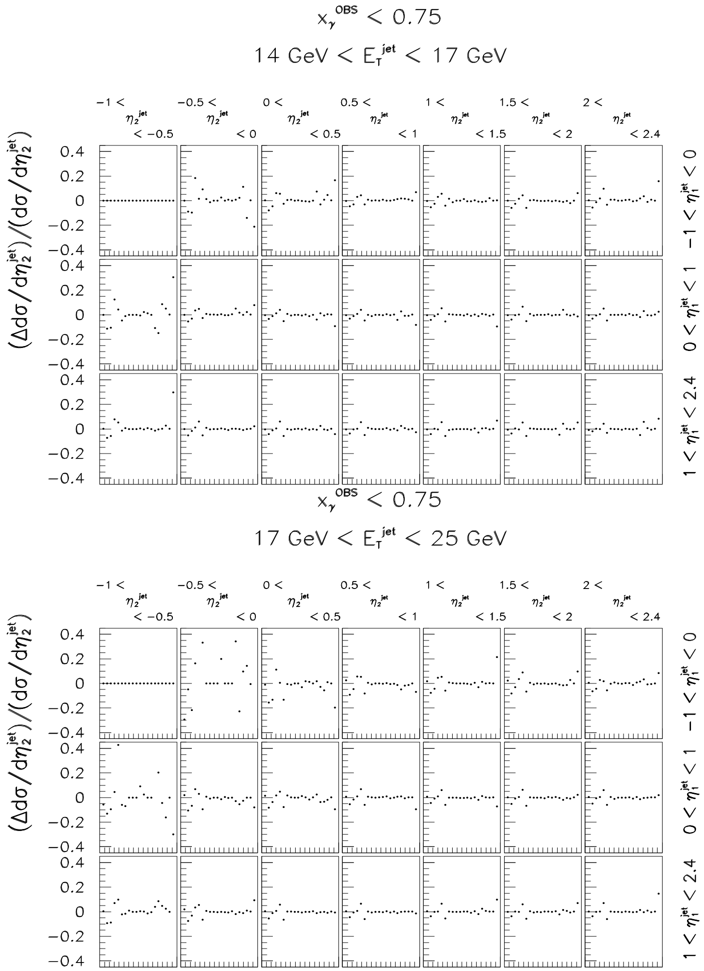

Figure 7.4: *The relative effect of various systematic variations in the analysis on the $d\sigma/d\eta_2^{jet}$ cross section for events with $x_\gamma^{OBS} < 0.75$. Shown in the upper plot is the cross section for events with 14 GeV $< E_T^{jet} <$ 17 GeV, in the lower plot with 17 GeV $< E_T^{jet} <$ 25 GeV. The points are in the same order as in figure 7.1*

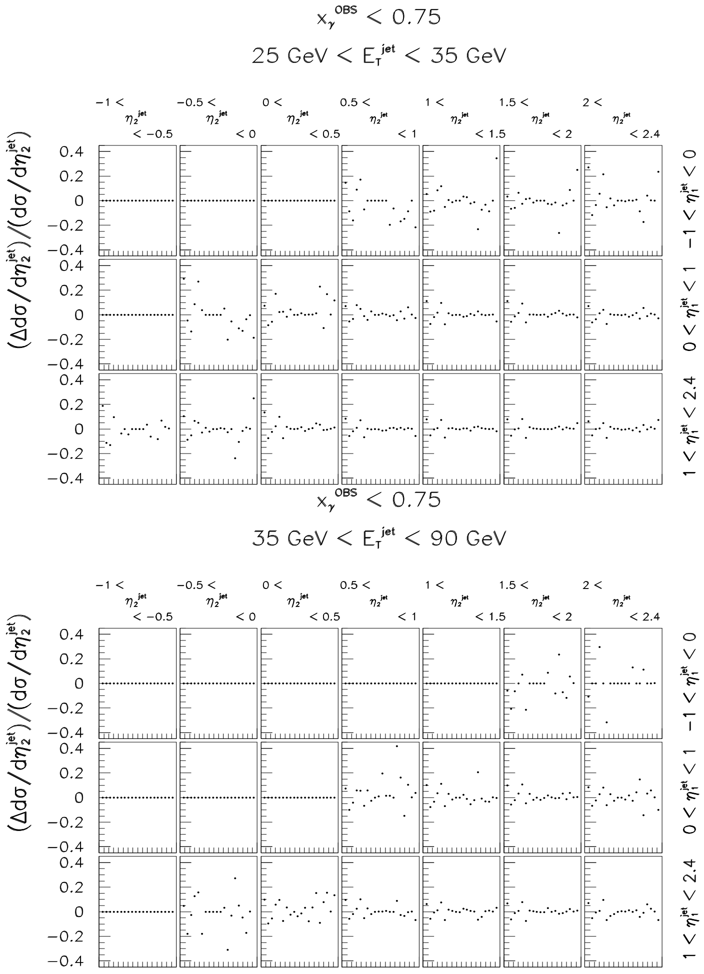

Figure 7.5: *The relative effect of various systematic variations in the analysis on the $d\sigma/d\eta_2^{jet}$ cross section for events with $x_\gamma^{OBS} < 0.75$. Shown in the upper plot is the cross section for events with 25 GeV $< E_T^{jet} <$ 35 GeV, in the lower plot with 35 GeV $< E_T^{jet} <$ 90 GeV. The points are in the same order as in figure 7.1*

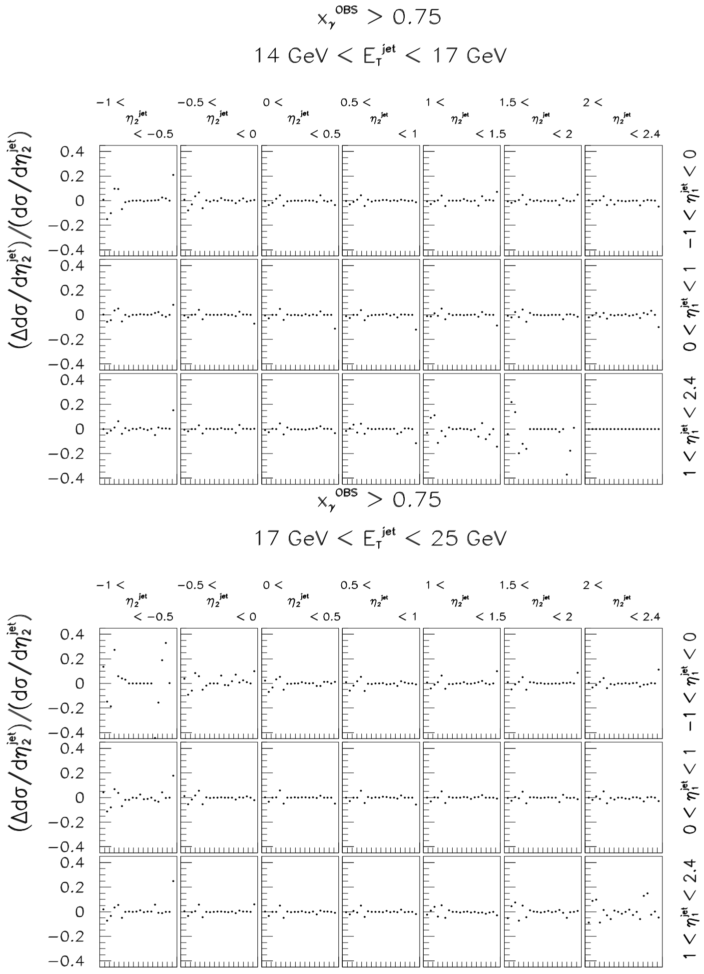

Figure 7.6: *The relative effect of various systematic variations in the analysis on the $d\sigma/d\eta_2^{jet}$ cross section for events with $x_\gamma^{OBS} > 0.75$. Shown in the upper plot is the cross section for events with 14 GeV $< E_T^{jet} <$ 17 GeV, in the lower plot with 17 GeV $< E_T^{jet} <$ 25 GeV. The points are in the same order as in figure 7.1*

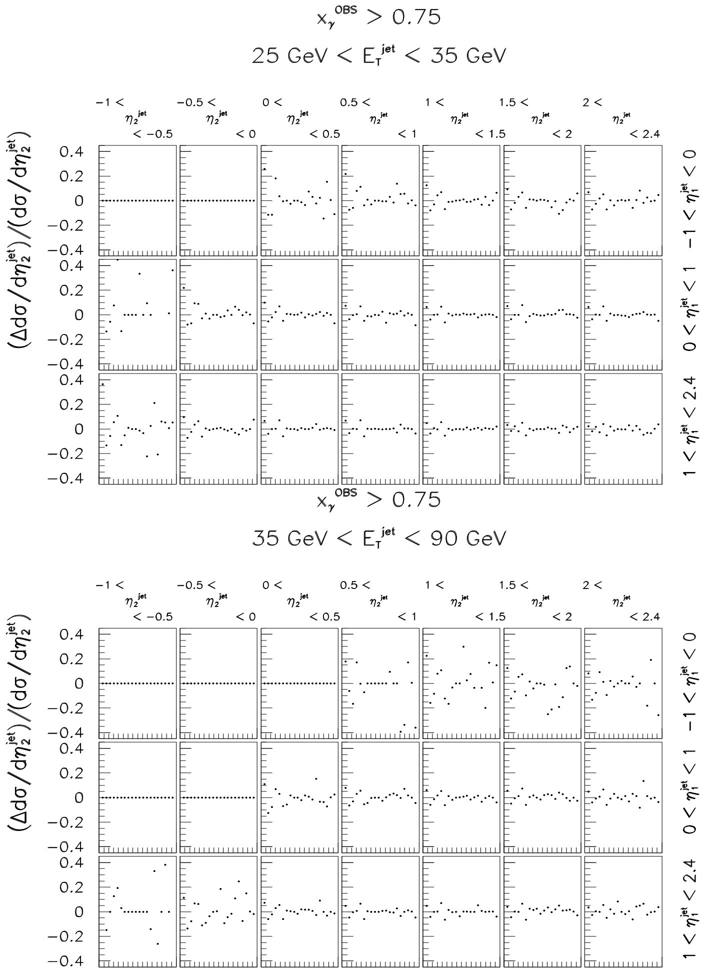

Figure 7.7: *The relative effect of various systematic variations in the analysis on the $d\sigma/d\eta_2^{jet}$ cross section for events with $x_\gamma^{OBS} > 0.75$. Shown in the upper plot is the cross section for events with 25 GeV $< E_T^{jet} <$ 35 GeV, in the lower plot with 35 GeV $< E_T^{jet} <$ 90 GeV. The points are in the same order as in figure 7.1*

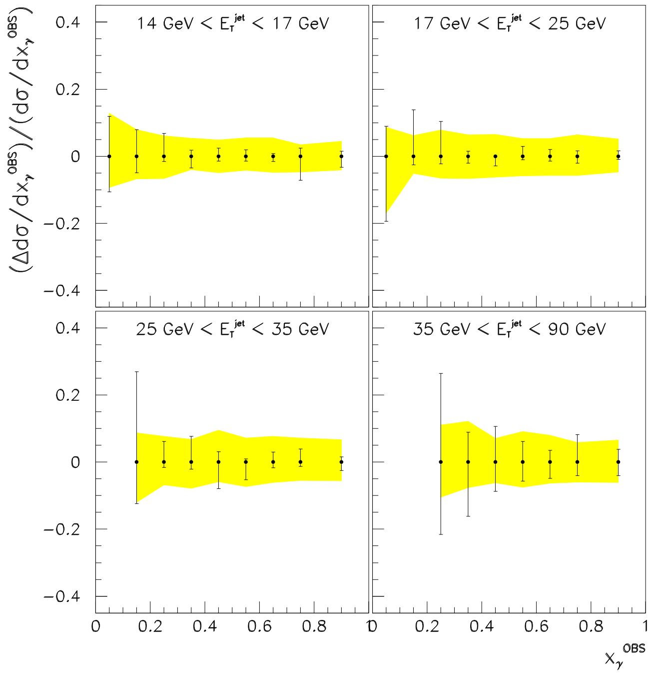

Figure 7.8: *Example of total systematic uncertainties for the differential x_γ^{OBS} cross sections. Indicated as shaded bands are the uncertainties related to the energy scale uncertainty. The error bars indicate the other systematic uncertainties added in quadrature. The statistical errors are not shown.*

Chapter 8

Results

The dijet photoproduction cross sections measured in the variables $E_{T,leading}$, x_γ^{OBS}, $\cos\theta^*$ and η_1^{jet} and η_2^{jet} as defined in section 2.1 are presented in the following. Tables of the numerical values of the cross sections are given in the appendix C.

8.1 Cross Sections for $0.2 < y_{JB} < 0.85$

Dijet cross sections are measured within the kinematical range $0.2 < y_{JB} < 0.85$ (see equation 5.2). This corresponds to Q^2 values less than 1 GeV and to center-of-mass energies for the photon-proton system $W_{\gamma p}$ (see equation 2.2) from 134 GeV to 277 GeV.

The dijet cross section as function of the transverse energy of the leading jet is presented in six different ranges of the jet pseudorapidity. The cross sections are determined requiring x_γ^{OBS} to be either less than or greater than 0.75 to distinguish resolved from direct events. The numerical values for the cross sections and the assigned uncertainties are given in table C.11 and C.13. The results are plotted in figures 8.1 and 8.2. The data is compared, as in all following figures, to NLO QCD predictions based on the calculations from Frixione *et al.* and on the GRV photon structure function. The two shaded bands indicate the energy scale and the theoretical uncertainty, respectively. High x_γ^{OBS} events dominate the cross sections in the very backward directions as expected from the

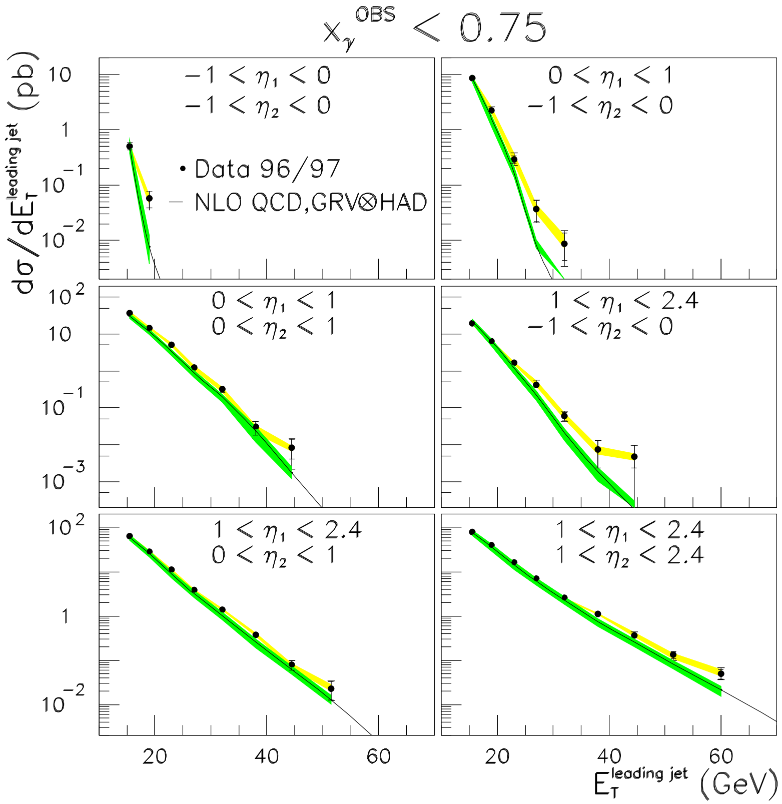

Figure 8.1: *Differential cross section $d\sigma/dE_T^{leading\ jet}$ for $x_\gamma^{OBS} < 0.75$ in the kinematic range $0.2 < y < 0.85$ and $Q^2 < 1$ GeV^2. The corresponding η ranges are given in the plots. The line is the NLO QCD prediction using the GRV photon structure function corrected for hadronisation. The two shaded bands indicate the energy scale uncertainty for the data and the theoretical uncertainty for the calculations, respectively.*

functional dependence of x_γ^{OBS} on η of the jets. The slopes and absolute values of the cross sections are in general well described by the theoretical calculations over almost three orders of magnitude. The deviations of the theoretical calculations from the data cross sections for $x_\gamma^{OBS} > 0.75$ and two forward going jets at low transverse energy of the leading jet originate from edge effects of the phase space being probed. In general the

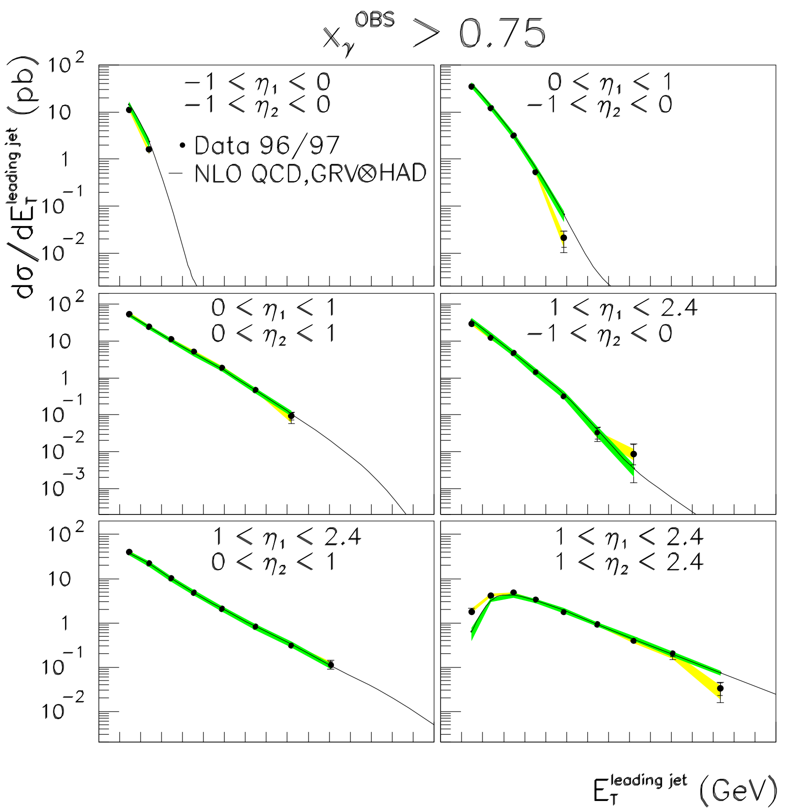

Figure 8.2: *Differential cross section $d\sigma/dE_T^{leading\ jet}$ for $x_\gamma^{OBS} > 0.75$ in the kinematic range $0.2 < y < 0.85$ and $Q^2 < 1$ GeV^2. The corresponding η ranges are given in the plots. The line is the NLO QCD prediction using the GRV photon structure function corrected for hadronisation. The two shaded bands indicate the energy scale and theoretical uncertainty, respectively.*

description is better for the high x_γ^{OBS} cross sections. For the low x_γ^{OBS} cross sections the NLO calculations tends to underestimate the data cross sections. This tends to be a function of the transverse energy of the leading jet which sets the scale of the process. A possible explanation of this behaviour could be an corresponding underestimation of the size of the photon structure functions at low x_γ values, which in this region would

primarily be dominated by the gluon content of the photon. This discrepancy than might become more pronounced when the photon structure functions are evolved by the DGLAP equations to higher scales in a range where the photon structure functions are not well constrained by previous experiments. Translated into a naive LO picture for the resolved and direct processes this would indicate the need for a higher gluon content within the photon at low x_γ.

Tables C.1 to C.4 and C.5 to C.8 show the cross sections as function of η_2^{jet} for four different E_T ranges of the leading jet and six different ranges of η_1^{jet} and again separated for x_γ^{OBS} less and greater than 0.75. The corresponding plots are given in figure 8.3 and 8.4. For both regions in x_γ^{OBS} the NLO QCD gives an overall good description of the data points. Only for $x_\gamma^{OBS} < 0.75$ and transverse energy of the leading jet $E_T^{jet} > 35$ GeV the NLO QCD underestimates the data points. This is consistent with the trend seen in the differential cross section $d\sigma/dE_T^{leading\ jet}$ in figure 8.1.

Given in table C.9 and figure 8.5 are the cross sections as function of $\cos\theta^*$ for four different ranges in x_γ^{OBS}. The best description is given for the bin with $x_\gamma^{OBS} > 0.85$. This corresponds to the direct enhanced sample where the photon interacts mostly as a bare photon with the least dependence on the photon structure function. The description in the lower x_γ^{OBS} bins is poorer. Both the data and theory also exhibit a change in shape when going from very high x_γ^{OBS} to low x_γ^{OBS} values. This corresponds to a change of the propagator in the dominant terms of the cross sections from a quark to a gluon propagator indicating that the different contributions from diagrams with quark and gluon propagator (e.g. figures 1.4 and 1.5) are summed correctly in the NLO calculation.

The above shown comparisons of the measured experimental cross sections with different theoretical predictions and their general agreement shows strong evidence that the established formalism of NLO calculations used in the determination of the theoretical distributions can be a way to extract information about the photon structure from these cross sections. Nevertheless it is also true that the dependance of these distributions on the photon structure function is not strong enough to use them as a means of a measurement of the photon structure. As in the case for the proton structure function measurements

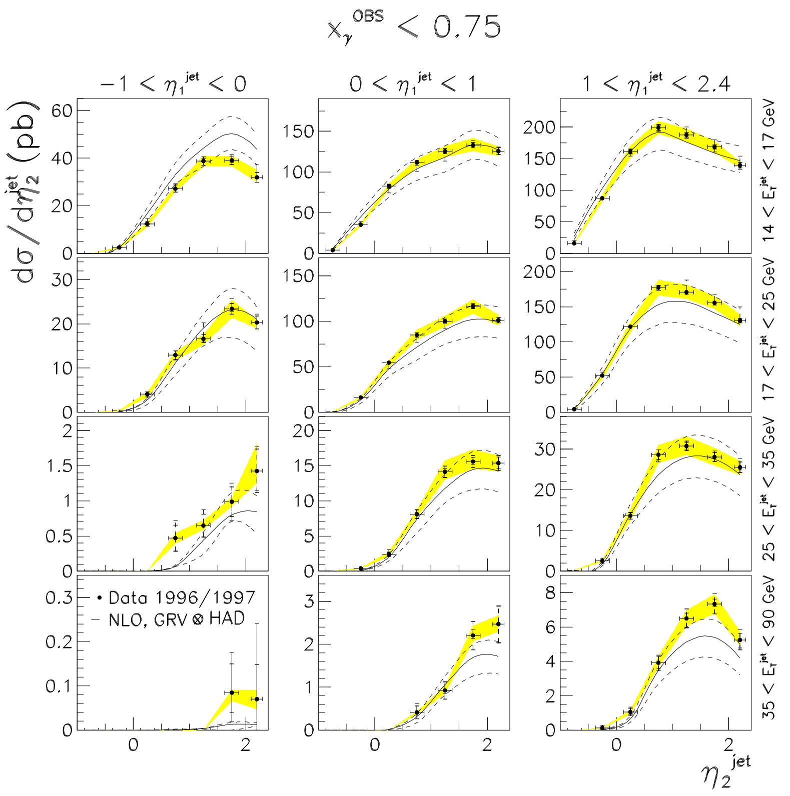

Figure 8.3: *Differential cross section $d\sigma/d\eta_2^{jet}$ for $x_\gamma^{OBS} < 0.75$ in the kinematic range $0.2 < y < 0.85$ and $Q^2 < 1$ GeV^2 in different bins of transverse energy for the leading jet. The corresponding η ranges are given in the plots.The solid line is the NLO QCD prediction using the GRV photon structure function corrected for hadronisation. The dashed lines indicate the theoretical uncertainties. The shaded band indicates the energy scale uncertainty.*

one would prefer to use the cross sections with a variable which, as in the case for the proton variable x_{Bj}, is directly related to the photon structure function. This is the reasoning behind the measurement of the differential cross sections as function of x_γ as shown in the next figure 8.6.

Given in table C.15 and figure 8.6 are the cross sections as function of x_γ^{OBS} for four

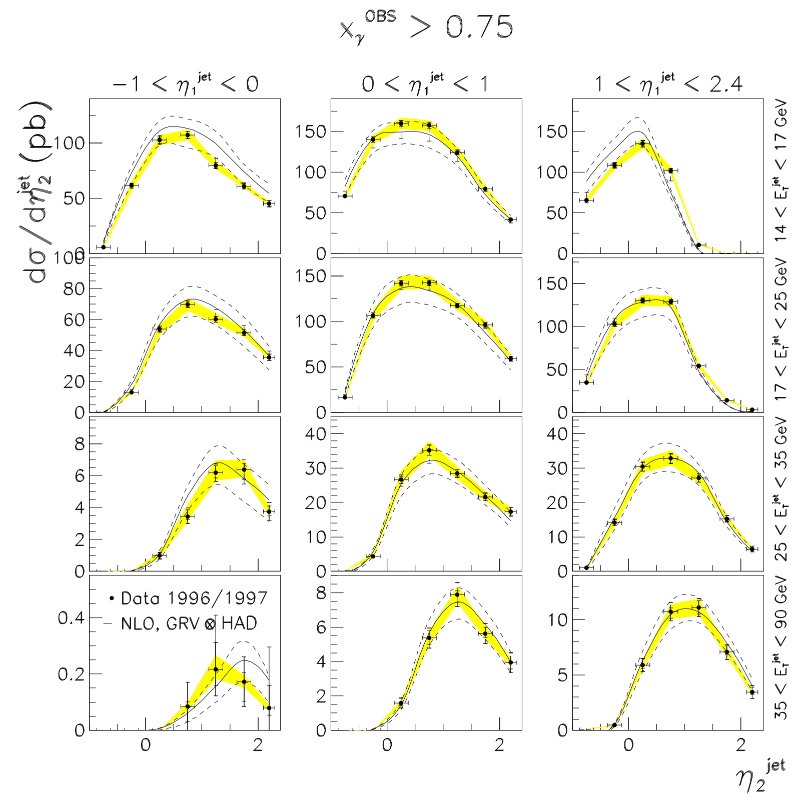

Figure 8.4: *Differential cross section $d\sigma/d\eta_2^{jet}$ for $x_\gamma^{OBS} > 0.75$ in the kinematic range $0.2 < y < 0.85$ and $Q^2 < 1$ GeV^2 in different bins of transverse energy for the leading jet. The corresponding η ranges are given in the plots.The solid line is the NLO QCD prediction using the GRV photon structure function corrected for hadronisation. The dashed lines indicate the theoretical uncertainties. The shaded band indicates the energy scale uncertainty.*

different ranges in the transverse energy of the leading jet. The NLO QCD predictions are shown this time for the three different photon structure functions introduced in 1.4. All three NLO calculations tends to underestimate the measured cross sections. The best description is given using the GRV photon structure function. For a better comparison the ratios of the measured cross sections to the single NLO QCD predictions are shown in

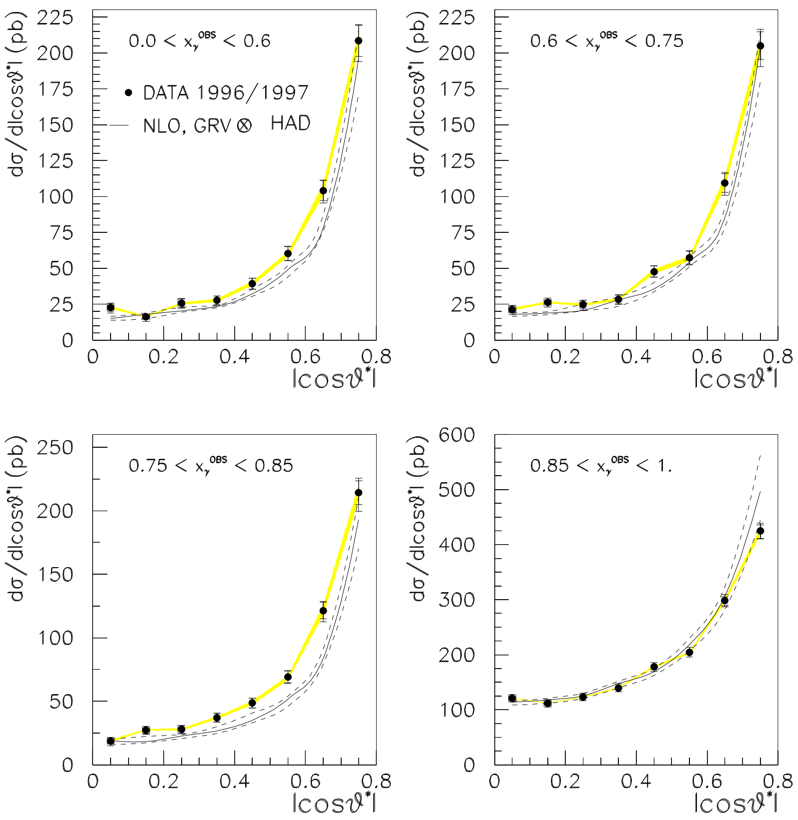

Figure 8.5: *Differential cross section $d\sigma/d|\cos\theta^*|$ for four different bins in x_γ^{OBS} in the kinematic regime of 0.2 < y < 0.85 and Q^2 < 1 GeV^2. . The corresponding x_γ^{OBS} ranges are given in the plots. The line is the NLO QCD prediction using the GRV photon structure function corrected for hadronisation. The dashed line indicate the upper and lower theoretical uncertainties.*

figures 8.7 to 8.9 together with the bands for the energy scale and theoretical uncertainty, respectively. The ratios for all structure functions tend to increase with higher transverse energy of the leading jet. The shape of the ratios is almost flat for the GRV photon structure function with all points falling within the theoretical uncertainties. The AFG parametrisation shows a similar but slight worse behaviour for the shapes. For the GS96

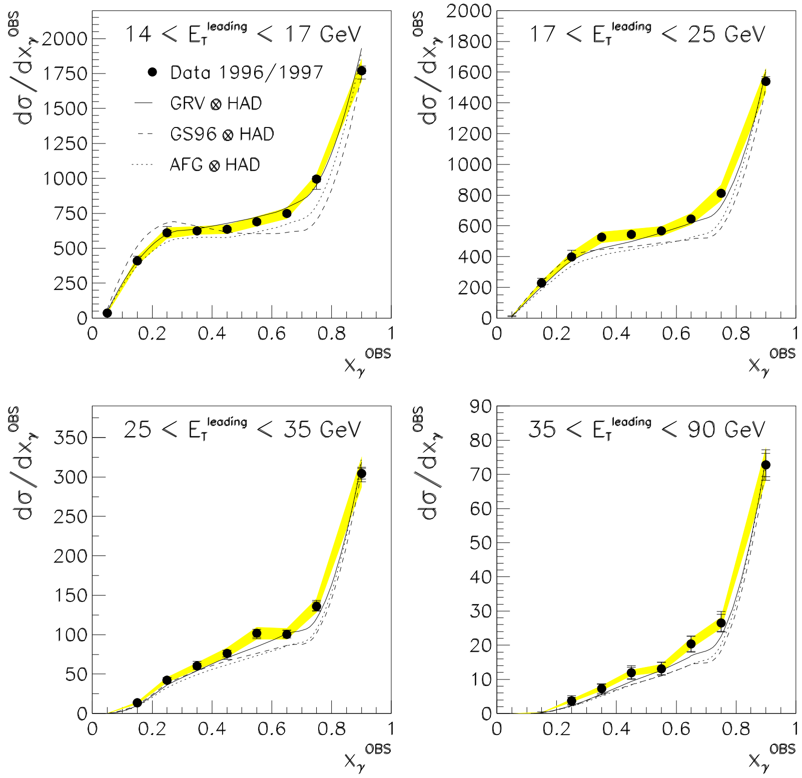

Figure 8.6: *Differential cross section $d\sigma/dx_\gamma^{OBS}$ for four different bins in the transverse energy of the leading jet in the kinematic regime 0.2 < y < 0.85 and Q^2 < 1 GeV. The corresponding energy ranges are given in the plots. The different lines are the NLO QCD predictions using specific photon structure function corrected for hadronisation. For simplicity the theoretical uncertainties are dropped.*

photon structure function the shape of the ratio deviates significantly from a flat line for the two most significant low transverse energy bins. The GS96 photon structure function is highly disfavoured by this figure. The discrepancy might be caused for the low x_γ^{OBS} region by the difference in the gluon density as seen in figure 1.8 for x_γ^{OBS} below 0.3. (The parton densities are scaled in this figure with x_γ^{OBS}). The GS96 parametrisation

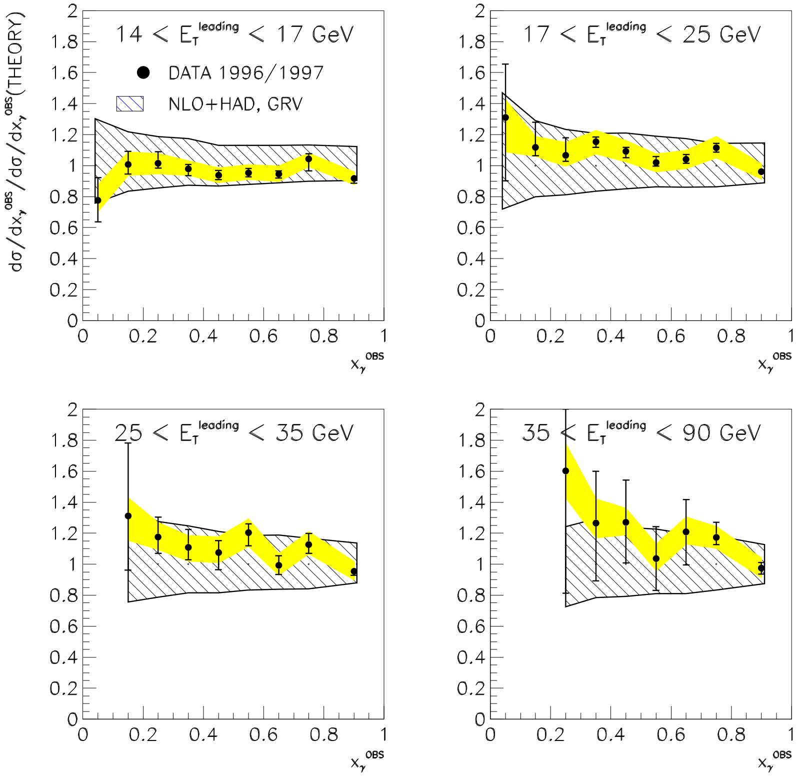

Figure 8.7: *Ratio of measured to theoretical cross sections $d\sigma/dx_\gamma^{OBS}$ using the GRV photon structure function. The shaded and hashed bands indicates the energy scale and theoretical uncertainties, respectively. The last point in x_{gamma}^{OBS} corresponds to the direct-dominated regime of the cross sections which can be reliably calculated using QED. This explains the fact that this point lies almost at one.*

for the gluon density is significantly higher than for the GRV and AFG parametrisation, resulting in higher cross sections for the low x_γ^{OBS} region. For high x_γ^{OBS} values the dominant contributions of the cross section originates from the quark density which is lower for the GS96 parametrisations and may be the cause for the ratio of data to theory to be greater than one in this region.

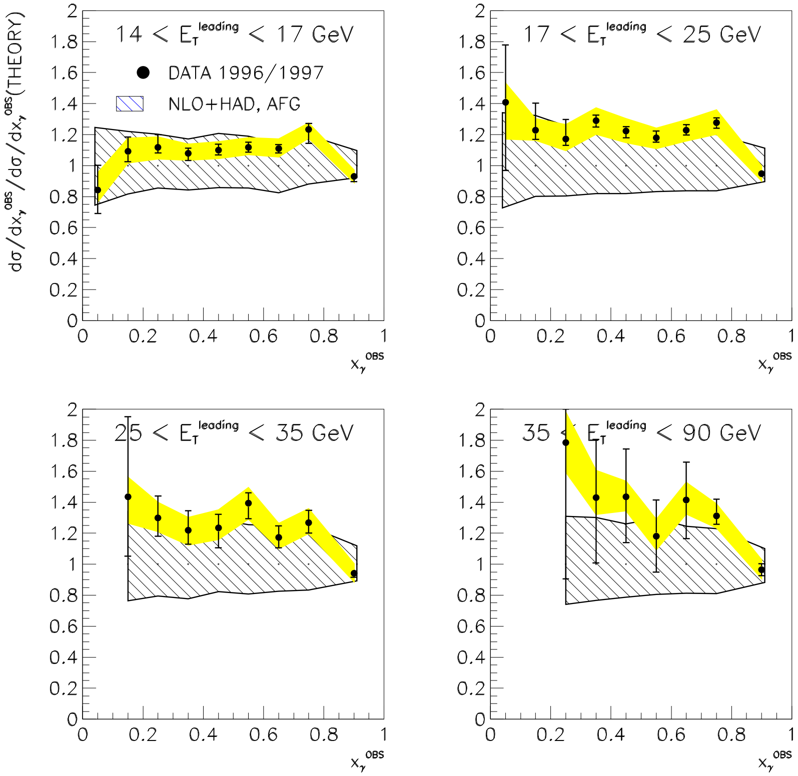

Figure 8.8: *Ratio of measured to theoretical cross sections $d\sigma/dx_\gamma^{OBS}$ using the AFG photon structure function. The shaded and hashed bands indicates the energy scale and theoretical uncertainties, respectively. The last point in x_{gamma}^{OBS} corresponds to the direct-dominated regime of the cross sections which can be reliably calculated using QED. This explains the fact that this point is almost at one.*

8.2 Summary

A measurement of dijet photoproduction cross sections in the kinematical regime $0.20 < y < 0.85$ and $Q^2 < 1$ GeV^2 with the transverse momenta of the two jets fulfilling the requirements $E_{T,1} > 14$ GeV and $E_{T,2} > 11$ GeV and pseudo-rapidities between $-1 < \eta_{1,2}^{jet} <$

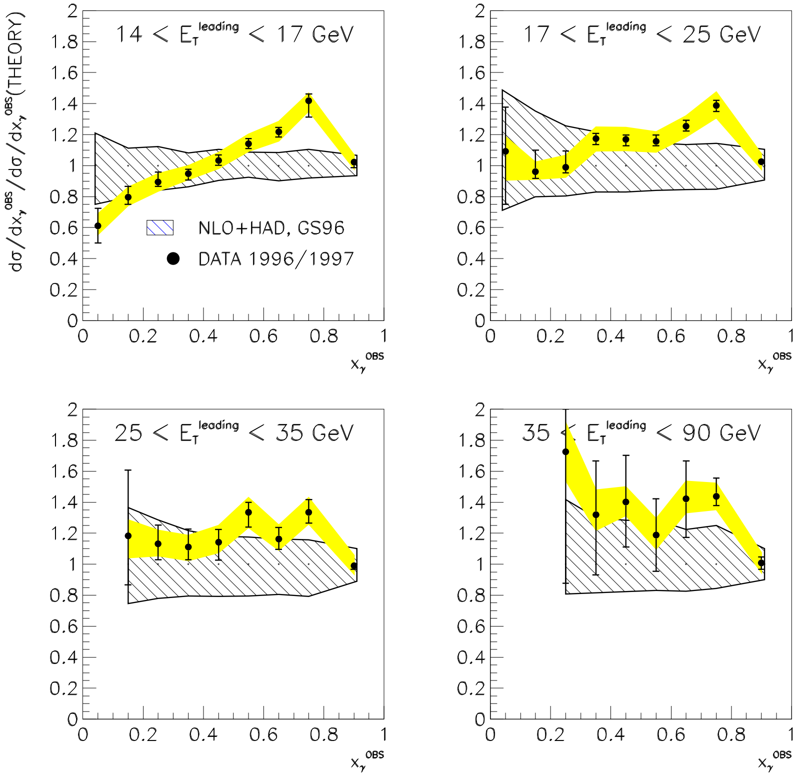

Figure 8.9: *Ratio of measured to theoretical cross sections $d\sigma/dx_\gamma^{OBS}$ using the GS96 photon structure function. The shaded and hashed bands indicates the energy scale and theoretical uncertainties, respectively. The last point in x_{gamma}^{OBS} corresponds to the direct-dominated regime of the cross sections which can be reliably calculated using QED. This explains the fact that this point is almost at one.*

2.4, have been presented. This is an extension of the measured pseudo-rapidity range by 0.4 units in the forward direction over a previous analysis [13], thus increasing the sensitivity of the measurements to resolved processes. The jets in the hadronic final state were reconstructed using the k_T-clustering jet algorithm.

Special care was taken to find an energy correction method to minimise the experimental uncertainty arising from the energy scale of the calorimeter, a limiting factor in similar studies in previous measurements. The resulting energy correction method achieved for the first time to constrain the energy uncertainty to about 1% over the full kinematical region measured.

Dijet cross sections have been measured as a function of the transverse energy of the leading jet, as a function of the pseudo-rapidity of the second jet, as a function of the cosine of the scattering angle in the dijet center-of-mass system and as a function of the fraction of the photon momentum participating in the hard scattering, the latter being experimentally estimated by x_γ^{OBS}. The extracted cross sections have been compared to NLO QCD calculations with different photon structure function parametrisations as input. An overall good agreement between data and NLO QCD predictions was found.

The measurements of the differential cross section as function of $\cos\theta^*$, which are probing the dominant matrix elements of the propagators, show a good agreement with the theoretical predictions in general. For low x_γ^{OBS} values the observed faster rise as function of $\cos\theta^*$ is consistent with the expectations on theoretical grounds due to the dominant gluon propagator terms and consistent with observations in previous publications [13]. In our case the same is seen to still hold at higher energies and masses. The agreement demonstrates that also in this high-mass region the dynamics of the short-distance process is understood.

The most significant cross section to draw conclusions from regarding the different parametrisations used as input was found to be the differential cross sections in x_γ^{OBS}. Comparing the ratios of measured to theoretical cross sections for these different parametrisations, a significant discrepancy in the description of the measured data was found for the GS96 parametrisation. Since the discrepancies are larger than the associated theoretical uncertainties this suggests that the GS96 parametrisation is not properly describing the parton densities of the photon in the probed kinematical region. The largest theoretical uncertainties, estimated by the variation of the renormalisation and factorisation scales, are thought to be higher-order contributions not present in the NLO calculations used.

Nevertheless the inclusion of these terms would have to result in a significant change of shape of the distributions (8.6-8.9) as function of x_γ^{OBS} and of the transverse energy (8.1) if it were to describe the measured data.

The results as given in this thesis cover a kinematic region with a high value for the hard scale. This region is not constrained by previous e^+e^- F_2^γ measurements. It is only recently that measurements F_2^γ from LEP extended up to an average scale of $\sim$ 28 GeV [118]. Our data at low x_γ^{OBS} constrain the parton densities in the photon, implying that future parametrisations should take them into account. The implications would even be stronger if improved higher-order or resummed calculations would be available, which will be explained further in the addendum. It remains to be shown how the existing parton density functions of the photon can be modified to describe both the presented ep data and existing results from e^+e^- experiments.

In the years 2000-2001 HERA undertook a big effort to upgrade the acceleration system to increase the luminosity by a factor of 4-5. The successful implementation of this upgrade will increase the event rates for low x_γ^{OBS} events which can then be used to minimise the statistical errors in this kinematic region. Assuming a uniform running from 2002 on up to the projected end of HERA in 2006, a data set enlarged by a factor of 10-16 will be accumulated resulting in an reduction of the statistical errors by a factor 3-4. This will be a major step forward in the determination of the photon structure function at low x_γ^{OBS}.

Looking even further into the future the commissioning of a linear e^+e^- collider as for example the proposed Tera Electron Volt Superconducting Linear Accelerator (TESLA) would extend the accessible phase space to significant higher scales, reaching values where there might be no need for higher-order terms in the pQCD NLO calculations due to the high hard scale of the processes.

Appendix A

Addendum

High energy physics is a forward moving field of research so it is no surprise that during the time span of writing this thesis and its final submission and defense there was an ongoing development of the topic covered in this thesis. This addendum tries to summarise the most important points as known at the end of 2002.

At the time of summing up the results to write this thesis, its results have also been submitted to the ZEUS Editorial Board for publication and have been finally published in the European Physical Journal C [117]. While preparing the final publication, it became necessary to perform some changes to the source code to correct for found errors. These corrections affected the values of the extracted differential cross sections, especially those measured differentially in E_T^{jet}. The recommended values to be used in any future work are obviously the latest and hence those published in the above stated paper.

The plotted ratio $\left(d\sigma/dx\gamma^{OBS}\right) / \left(d\sigma/dx_\gamma^{OBS}\,(Theory)\right)$ in figure 8.9 showed for the GS96 photon parton density parametrisation a strange shape for the kinematic range in $E_T^{leading}$ between 14 and 17 GeV where it should be the most constrained. This discrepancy between the description as given by the other two used parton density parametrisations and GS96 caused the latter to be investigated in detail. It turned out that the GS96 parametrisation was not able to describe the data within the kinematic regime it was fitted to. This was caused by wrongly implemented quark thresholds, an error which shows up more prominent at low energy scales and which gets adjusted a little bit by the QCD evolution when going to higher and higher energy scales. Since the author of the GS96 parametrisation left the field corrections to this parametrisation are not possible and its use should be discarded.

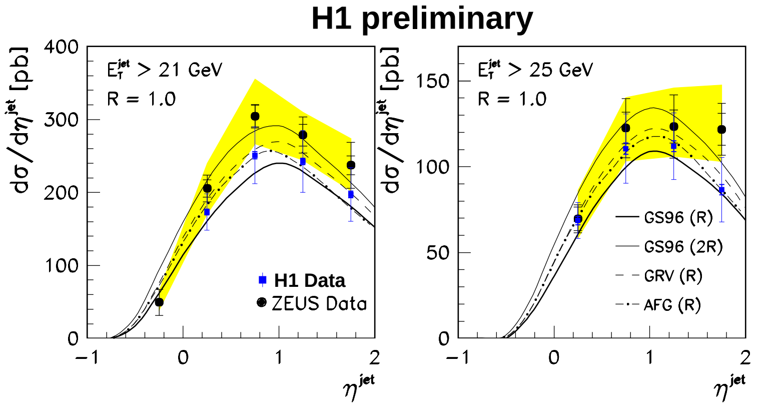

Figure A.1: *Comparison of differential cross sections $d\sigma/d\eta^{jet}$ from H1 and ZEUS [120] for two different bins in E_T^{jet} of the leading jet. The black squares show the H1 data with associated statistical (inner bars) and experimental errors (outer bars), the black dots are the equivalent ZEUS data points. The shaded band includes additional for the ZEUS data the uncertainty arising from the energy scale uncertainty.*

The presentation of preliminary results of this analysis at various conferences caused the competing experiment at HERA, H1 (which has been described very shortly in 3.2.2), to perform an equivalent analysis published in section [119]. A comparison of the main results of the two different experiments as stated in the following lines can be found in [120]. Shown in figure A.1 is as an example of this comparison a preliminary result of H1 and a result of ZEUS. The figure illustrates the differential cross section $d\sigma/d\eta^{jet}$ for two different thresholds for the E_T of the highest energy jet. The error bars indicate the statistical and experimental uncertainties. The lines correspond to the NLO calculations of the cross sections using different photon structure functions as inputs. The data from H1 and ZEUS are found to agree within the error bars. Similar comparisons exits for

differential cross sections in E_T^{jet} which again agree within the error bars.

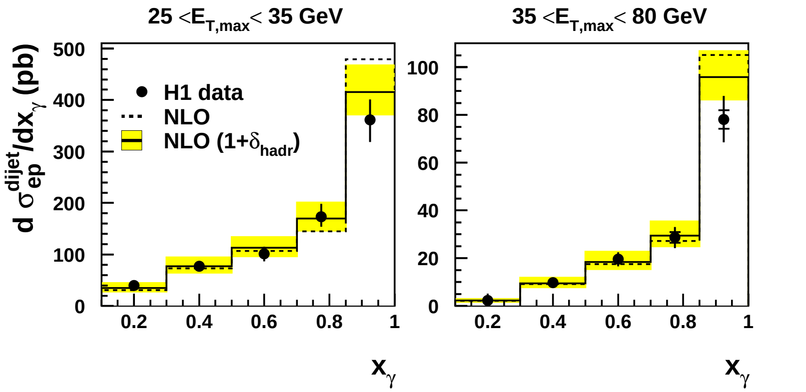

Figure A.2: *Differential cross section in $d\sigma/dx_\gamma^{OBS}$ as measured by the H1 experiment for two different bins in E_T^{jet} of the leading jet. The black dots are the H1 data points, the dotted line represents a NLO calculation, the full line with shaded side bands is the NLO calculation taking the hadronisation correction into account. On the left hand side plot the statistical errors are to small to be seen.*

In figure 8.6 the differential cross section in $\mathrm{d}\sigma/\mathrm{d}x_\gamma^{OBS}$ for four different bins in the transverse energy of the leading jet was given. A corresponding result of H1 is shown in figure A.2. The plot also shows as a dotted line the result of the NLO calculation and as a shaded band band the NLO calculation with a hadronisation correction included. Figure A.3 is the analogous plot to figures 8.7 and 8.8. It shows the relative deviation of the experimental measured cross section to the theoretical predicted cross section where the two different photon structure parametrisations AFG and GRV are used as input to the calculations. In contrast to the result of this thesis (Figures 8.7 and 8.8) and also to the result published in the ZEUS paper [117], the H1 data and the NLO calculations agree, suggesting that the photon structure functions are correct. This discrepancy in the results between the two experiments caused ZEUS to investigate the possible cause. One difference between the two measurements is the threshold cut used on the transverse energy of the second highest E_T^{jet}. While ZEUS required a minimum E_T^{jet} of 11 GeV, H1 used 15 GeV as threshold. The dependence of the cross section on this E_T^{jet} cut can

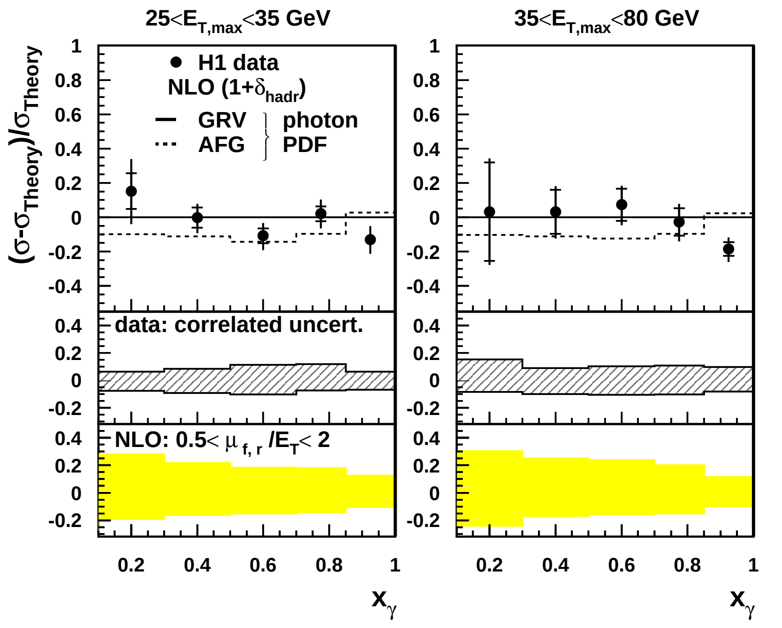

Figure A.3: *Relative difference of experimental and theoretical cross section for $d\sigma/dx_\gamma^{OBS}$ using different photon structure functions as given by H1*

be seen in figure A.4 where the measured cross section as function of this cut is plotted for different regions in x_γ^{OBS} and for transverse energies of the first jet between 25 and 35 GeV. Overlaid is the dependence of the Monte Carlo hadron cross section and the NLO calculation. As can be seen, the shape of the dependence agrees for Monte Carlo and NLO calculation while the shape for the dependence of the measured cross section differ. While using a low threshold of 11 GeV, the measured cross section is above the NLO prediction the difference in shape results in a crossing at about 15 GeV (the H1 threshold cut). For higher threshold cuts the measured cross section is below the predictions. Thus the apparent difference in the differential x_γ^{OBS} cross sections are caused by the different threshold cut used and is not a problem of the measured data as such but originates from theoretical calculations used in the comparison.

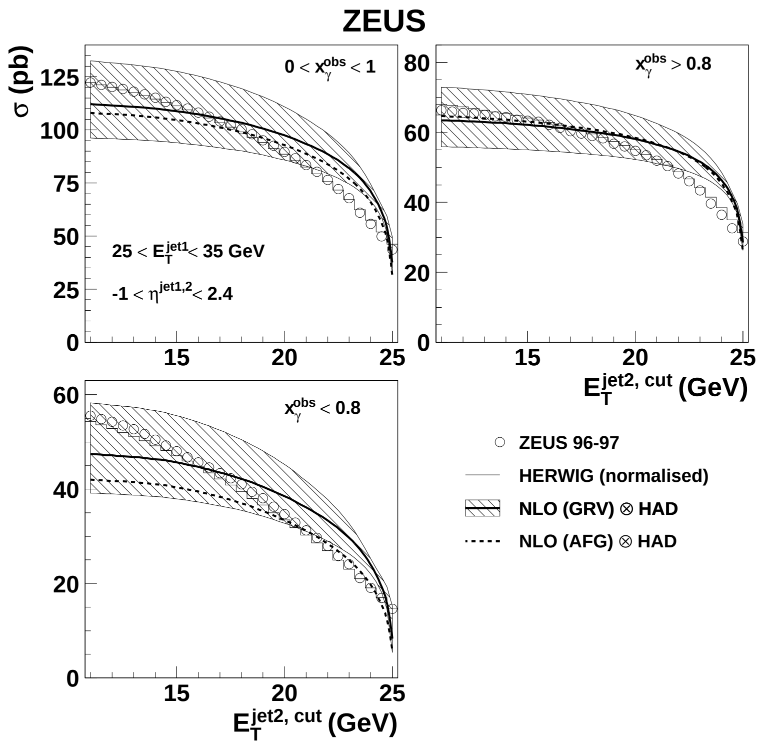

Figure A.4: *Measured cross section as function of the threshold cut required for the transverse energies of the second highest E_T^{jet}.*

The similarity in the dependence on the threshold cut between the Monte Carlo cross sections, based on LO and parton showers simulating NLO effects, and the NLO calculations which are in contrast to the dependence of the measured cross sections might indicate again that higher order terms are not negligible in the calculation of a theoretical prediction. NNLO calculations are estimated to be available at the time of start of the Large Hadron Collider which is scheduled for 2007. To be of full use an effort should be undertaken to have a NNLO based Monte Carlo available at the same time.

Appendix B

Parton Momentum Fractions

The momentum fractions of the initial photon and proton involved in the hard scattering $ab \to cd$ are defined as

$$x_\gamma^{LO} = \frac{p \cdot a}{q \cdot p} \quad \text{(B.1)}$$

$$x_p^{LO} = \frac{q \cdot b}{q \cdot p}, \quad \text{(B.2)}$$

where q is the momentum of the photon, p is the momentum of the proton, a is the momentum of the parton originating from the photon and b is the momentum of the parton originating from the proton. Neglecting transverse momenta and masses of the partons a and b with respect to their mother particles and assuming collinearity between the photon and proton this reduces to

$$x_\gamma^{LO} = \frac{E_a}{E_\gamma} \quad \text{(B.3)}$$

$$x_p^{LO} = \frac{E_b}{E_p}, \quad \text{(B.4)}$$

where E_a and E_b are the energies of parton a and b, respectively.

The momentum fractions can also be determined using the energies and scattering angles of the outgoing partons as given in equation 2.3 and 2.5,

$$x_\gamma^{LO} = \frac{\sum_{partons} E_T^{parton} e^{-\eta^{parton}}}{2yE_e}, \quad \text{(B.5)}$$

$$x_p^{LO} = \frac{\sum_{partons} E_T^{parton} e^{\eta^{parton}}}{2E_p}, \quad \text{(B.6)}$$

A short derivation is given in the following. Starting from the expression

$$E_T^{parton} e^{-\eta^{parton}} \quad \text{(B.7)}$$

and using the relation

$$\eta = -\ln \tan\left(\frac{\theta}{2}\right) \quad \text{(B.8)}$$

one can write

$$\begin{aligned}
E_T^{parton} e^{-\eta^{parton}} &= E^{parton} \sin\theta^{parton} \tan\left(\theta^{parton}/2\right) && \text{(B.9)}\\
&= E^{parton} \sin\theta^{parton} \left(\frac{1-\cos\theta^{parton}}{\sin\theta^{parton}}\right) && \text{(B.10)}\\
&= E^{parton} \left(1-\cos\theta^{parton}\right) && \text{(B.11)}\\
&= E^{parton} - P_z^{parton}. && \text{(B.12)}
\end{aligned}$$

Under the assumption of collinearity $E_a = -p_{z,a}$ and $E_b = p_{z,b}$ and the equation further simplifies to

$$\begin{aligned}
E_T^a e^{-\eta^a} &= 2 \cdot E_a && \text{(B.13)}\\
E_T^b e^{-\eta^b} &= 0.
\end{aligned}$$

Equation B.5 reduces, when using the result obtained in B.13, to

$$x_\gamma^{LO} = \frac{2E_a}{2yE_e} = \frac{E_a}{E_\gamma}. \quad \text{(B.14)}$$

A similar replacement for the x_p^{LO} definition in equation B.6 yields

$$x_p^{LO} = \frac{2E_b}{2E_p} = \frac{E_b}{E_p}. \quad \text{(B.15)}$$

Appendix C

Tables of Cross Sections

$d\sigma/d\eta_2^{Jet}$				
14 GeV < $E_T^{leading\ jet}$ < 17 GeV, x_γ^{OBS} < 0.75				
η_2^{Jet}	$d\sigma/d\eta_2^{Jet}$ pb	Δ_{stat} pb	Δ_{syst}(+/-) pb	$\Delta_{E-scale}$ (+/-) pb
-1.0 < η_1^{jet} < 0.0				
-0.5 .. 0.0	2.43	0.44	0.29/-0.62	0.45/-0.24
0.0 .. 0.5	12.29	0.97	2.31/-0.40	0.75/-0.99
0.5 .. 1.0	27.22	1.48	2.05/-0.03	1.16/-1.24
1.0 .. 1.5	38.75	1.75	1.11/-0.81	2.14/-2.05
1.5 .. 2.0	39.08	1.77	2.34/-1.01	1.72/-2.34
2.0 .. 2.4	31.95	2.08	5.24/-0.38	3.11/-1.77
0.0 < η_1^{jet} < 1.0				
-1.0 .. -0.5	4.07	0.60	1.31/-0.75	0.50/-0.46
-0.5 .. 0.0	35.40	1.66	3.47/-0.20	1.69/-1.89
0.0 .. 0.5	82.55	2.61	1.19/-8.38	3.41/-4.17
0.5 .. 1.0	111.29	3.04	3.16/-10.27	4.49/-5.18
1.0 .. 1.5	125.62	3.04	1.32/-12.21	6.53/-6.91
1.5 .. 2.0	132.91	3.19	5.40/-2.13	8.77/-7.00
2.0 .. 2.4	125.41	4.10	4.99/-2.50	6.16/-5.76
1.0 < η_1^{jet} < 2.4				
-1.0 .. -0.5	16.19	1.21	4.85/-0.24	1.27/-1.17
-0.5 .. 0.0	87.40	2.69	2.11/-1.06	5.21/-4.65
0.0 .. 0.5	161.25	3.62	4.05/-7.26	9.53/-9.03
0.5 .. 1.0	199.04	4.02	5.61/-6.27	10.97/-9.79
1.0 .. 1.5	187.80	3.65	12.64/-5.69	10.27/-10.91
1.5 .. 2.0	168.76	3.53	11.21/-8.03	9.01/-9.67
2.0 .. 2.4	139.81	4.18	14.08/-6.96	6.01/-4.38

Table C.1: *Differential dijet cross section $d\sigma/d\eta_2^{jet}$ in the kinematic range 0.2 < y < 0.85, Q^2 < 1 GeV^2 and x_γ^{OBS} < 0.75. Given in the table are the values for transverse energy of the leading jet between 14 and 17 GeV and an transverse energy for the second jet greater than 11 GeV in three different bins in the pseudo-rapidity of the leading jet.*

$d\sigma/d\eta_2^{Jet}$				
17 GeV $< E_T^{leading\ jet} <$ 25 GeV, $x_\gamma^{OBS} <$ 0.75				
η_2^{Jet}	$d\sigma/d\eta_2^{Jet}$ pb	Δ_{stat} pb	Δ_{syst}(+/-) pb	$\Delta_{E-scale}$ (+/-) pb
-1.0 $< \eta_1^{jet} <$ 0.0				
-0.5 .. 0.0	0.31	0.14	0.25/-0.07	0.23/-0.09
0.0 .. 0.5	4.07	0.54	0.12/-0.86	0.45/-0.63
0.5 .. 1.0	12.98	0.94	0.08/-1.15	0.72/-1.19
1.0 .. 1.5	16.67	0.92	3.60/-0.51	0.91/-1.30
1.5 .. 2.0	23.40	1.24	2.34/-0.57	2.05/-1.95
2.0 .. 2.4	20.35	1.45	1.88/-0.36	0.58/-1.30
0.0 $< \eta_1^{jet} <$ 1.0				
-1.0 .. -0.5	0.64	0.21	0.43/-0.22	0.28/-0.08
-0.5 .. 0.0	16.41	1.06	0.14/-1.72	1.12/-1.73
0.0 .. 0.5	54.36	1.89	1.78/-5.96	2.63/-4.45
0.5 .. 1.0	84.92	2.33	1.40/-8.08	5.76/-4.98
1.0 .. 1.5	100.07	2.34	1.28/-7.57	6.02/-5.82
1.5 .. 2.0	116.52	2.64	2.83/-2.37	7.45/-7.89
2.0 .. 2.4	101.18	3.10	2.23/-1.97	6.02/-5.97
1.0 $< \eta_1^{jet} <$ 2.4				
-1.0 .. -0.5	4.04	0.49	2.33/-0.09	0.40/-0.37
-0.5 .. 0.0	52.13	1.80	4.85/-1.24	2.84/-3.92
0.0 .. 0.5	121.58	2.72	0.61/-2.02	7.03/-7.93
0.5 .. 1.0	177.01	3.28	0.99/-3.63	11.33/-10.57
1.0 .. 1.5	170.70	2.93	17.34/-3.53	11.13/-9.13
1.5 .. 2.0	155.97	2.90	11.18/-3.46	9.33/-8.87
2.0 .. 2.4	130.49	3.36	19.22/-0.97	9.11/-7.66

Table C.2: *Differential dijet cross section $d\sigma/d\eta_2^{jet}$ in the kinematic range 0.2 $< y <$ 0.85, $Q^2 <$ 1 GeV^2 and $x_\gamma^{OBS} <$ 0.75. Given in the table are the values for transverse energy of the leading jet between 17 and 25 GeV and an transverse energy for the second jet greater than 11 GeV in three different bins in the pseudo-rapidity of the leading jet.*

$d\sigma/d\eta_2^{Jet}$				
25 GeV $< E_T^{leading\ jet} <$ 35 GeV, $x_\gamma^{OBS} <$ 0.75				
η_2^{Jet}	$d\sigma/d\eta_2^{Jet}$ pb	Δ_{stat} pb	Δ_{syst}(+/-) pb	$\Delta_{E-scale}$ (+/-) pb
-1.0 $< \eta_1^{jet} <$ 0.0				
0.5 .. 1.0	0.47	0.18	0.25/-0.18	0.08/-0.08
1.0 .. 1.5	0.65	0.16	0.23/-0.17	0.08/-0.06
1.5 .. 2.0	0.99	0.21	0.26/-0.27	0.06/-0.07
2.0 .. 2.4	1.43	0.31	0.34/-0.28	0.39/-0.17
0.0 $< \eta_1^{jet} <$ 1.0				
-0.5 .. 0.0	0.38	0.15	0.29/-0.13	0.11/-0.05
0.0 .. 0.5	2.37	0.32	0.74/-0.26	0.41/-0.20
0.5 .. 1.0	8.11	0.65	0.58/-0.60	0.63/-0.45
1.0 .. 1.5	14.16	0.81	0.45/-0.81	1.58/-1.10
1.5 .. 2.0	15.59	0.87	0.60/-0.43	1.73/-0.97
2.0 .. 2.4	15.35	1.08	0.89/-0.75	1.08/-1.15
1.0 $< \eta_1^{jet} <$ 2.4				
-1.0 .. -0.5	0.21	0.11	0.21/-0.02	0.13/-0.03
-0.5 .. 0.0	2.54	0.34	0.64/-0.67	0.26/-0.22
0.0 .. 0.5	13.58	0.81	0.84/-0.27	1.81/-1.04
0.5 .. 1.0	28.59	1.22	0.47/-1.74	2.40/-1.93
1.0 .. 1.5	30.76	1.15	0.79/-0.74	2.41/-2.17
1.5 .. 2.0	28.05	1.12	1.53/-0.11	2.24/-2.04
2.0 .. 2.4	25.55	1.33	2.09/-0.65	1.58/-1.87

Table C.3: *Differential dijet cross section $d\sigma/d\eta_2^{jet}$ in the kinematic range 0.2 $< y <$ 0.85, $Q^2 <$ 1 GeV^2 and $x_\gamma^{OBS} <$ 0.75. Given in the table are the values for transverse energy of the leading jet between 25 and 35 GeV and an transverse energy for the second jet greater than 11 GeV in three different bins in the pseudo-rapidity of the leading jet.*

$d\sigma/d\eta_2^{Jet}$				
35 GeV $< E_T^{leading\ jet} <$ 90 GeV, $x_\gamma^{OBS} <$ 0.75				
η_2^{Jet}	$d\sigma/d\eta_2^{Jet}$ pb	Δ_{stat} pb	Δ_{syst}(+/-) pb	$\Delta_{E-scale}$ (+/-) pb
-1.0 $< \eta_1^{jet} <$ 0.0				
1.5 .. 2.0	0.08	0.07	0.09/-0.04	0.01/-0.02
2.0 .. 2.4	0.07	0.08	0.17/-0.00	0.02/-0.02
0.0 $< \eta_1^{jet} <$ 1.0				
0.5 .. 1.0	0.41	0.15	0.21/-0.06	0.03/-0.04
1.0 .. 1.5	0.92	0.20	0.19/-0.07	0.10/-0.07
1.5 .. 2.0	2.20	0.33	0.14/-0.07	0.24/-0.12
2.0 .. 2.4	2.46	0.43	0.42/-0.44	0.21/-0.16
1.0 $< \eta_1^{jet} <$ 2.4				
-0.5 .. 0.0	0.14	0.08	0.15/-0.05	0.02/-0.02
0.0 .. 0.5	1.05	0.22	0.29/-0.13	0.10/-0.10
0.5 .. 1.0	3.91	0.45	0.36/-0.32	0.40/-0.23
1.0 .. 1.5	6.50	0.55	0.32/-0.51	0.49/-0.43
1.5 .. 2.0	7.34	0.59	0.28/-0.16	0.57/-0.55
2.0 .. 2.4	5.25	0.59	0.35/-0.47	0.51/-0.35

Table C.4: *Differential dijet cross section $d\sigma/d\eta_2^{jet}$ in the kinematic range 0.2 $< y <$ 0.85, $Q^2 <$ 1 GeV^2 and $x_\gamma^{OBS} <$ 0.75. Given in the table are the values for transverse energy of the leading jet between 35 and 90 GeV and an transverse energy for the second jet greater than 11 GeV in three different bins in the pseudo-rapidity of the leading jet.*

$d\sigma/d\eta_2^{Jet}$				
14 GeV $< E_T^{leading\ jet} <$ 17 GeV, $x_\gamma^{OBS} >$ 0.75				
η_2^{Jet}	$d\sigma/d\eta_2^{Jet}$ pb	Δ_{stat} pb	Δ_{syst}(+/-) pb	$\Delta_{E-scale}$ (+/-) pb
-1.0 $< \eta_1^{jet} <$ 0.0				
-1.0 .. -0.5	5.69	0.68	1.20/-0.08	0.55/-0.86
-0.5 .. 0.0	61.48	2.25	1.64/-1.43	4.09/-4.84
0.0 .. 0.5	102.59	2.95	4.31/-4.07	4.52/-4.15
0.5 .. 1.0	107.23	3.04	1.46/-1.72	4.68/-4.58
1.0 .. 1.5	79.91	2.44	6.43/-3.32	3.16/-3.44
1.5 .. 2.0	60.90	2.25	3.25/-2.27	2.78/-1.88
2.0 .. 2.4	45.14	2.77	0.38/-3.16	1.58/-1.64
0.0 $< \eta_1^{jet} <$ 1.				
-1.0 .. -0.5	70.33	2.58	6.05/-1.49	3.60/-4.05
-0.5 .. 0.0	139.83	3.38	3.50/-10.38	5.69/-5.12
0.0 .. 0.5	159.32	3.57	4.40/-18.03	7.50/-6.45
0.5 .. 1.0	157.54	3.58	1.32/-19.52	5.75/-6.79
1.0 .. 1.5	124.26	3.01	2.91/-11.13	6.10/-4.63
1.5 .. 2.0	79.39	2.50	1.14/-3.15	3.48/-4.44
2.0 .. 2.4	41.83	2.47	1.57/-4.37	0.59/-1.30
1.0 $< \eta_1^{jet} <$ 2.4				
-1.0 .. -0.5	65.38	2.43	10.02/-3.35	4.11/-2.61
-0.5 .. 0.0	108.30	2.94	3.50/-3.57	3.26/-4.04
0.0 .. 0.5	135.39	3.23	3.62/-4.70	6.19/-6.01
0.5 .. 1.0	101.80	2.87	0.90/-12.63	4.19/-4.09
1.0 .. 1.5	10.64	0.95	0.52/-1.96	1.19/-1.22
1.5 .. 2.0	0.10	0.08	0.06/-0.04	0.02/-0.02

Table C.5: *Differential dijet cross section $d\sigma/d\eta_2^{jet}$ in the kinematic range 0.2 $< y <$ 0.85, $Q^2 <$ 1 GeV^2 and $x_\gamma^{OBS} >$ 0.75. Given in the table are the values for transverse energy of the leading jet between 14 and 17 GeV and an transverse energy for the second jet greater than 11 GeV in three different bins in the pseudo-rapidity of the leading jet.*

$d\sigma/d\eta_2^{Jet}$				
17 GeV $< E_T^{leading\ jet} <$ 25 GeV, $x_\gamma^{OBS} > 0.75$				
η_2^{Jet}	$d\sigma/d\eta_2^{Jet}$ pb	Δ_{stat} pb	Δ_{syst}(+/-) pb	$\Delta_{E-scale}$ (+/-) pb
$-1.0 < \eta_1^{jet} < 0.0$				
-1.0 .. -0.5	0.14	0.07	0.19/-0.07	0.04/-0.03
-0.5 .. 0.0	12.96	0.86	1.84/-0.35	1.08/-1.21
0.0 .. 0.5	53.89	1.87	1.33/-1.59	2.85/-3.68
0.5 .. 1.0	69.90	2.16	1.35/-1.73	3.75/-4.31
1.0 .. 1.5	60.20	1.84	6.07/-0.70	3.84/-2.66
1.5 .. 2.0	51.56	1.86	4.54/-0.29	2.62/-2.67
2.0 .. 2.4	35.60	2.03	3.98/-1.12	1.56/-1.40
$0.0 < \eta_1^{jet} < 1.0$				
-1.0 .. -0.5	16.47	1.02	3.06/-0.87	1.11/-1.86
-0.5 .. 0.0	106.78	2.66	1.03/-2.94	5.97/-5.85
0.0 .. 0.5	141.99	3.07	2.23/-7.16	8.22/-7.04
0.5 .. 1.0	142.45	3.06	2.72/-8.09	7.73/-6.32
1.0 .. 1.5	117.50	2.58	2.57/-1.64	5.99/-5.32
1.5 .. 2.0	96.38	2.49	2.24/-3.85	4.66/-4.43
2.0 .. 2.4	59.04	2.50	0.35/-2.84	3.02/-2.75
$1.0 < \eta_1^{jet} < 2.4$				
-1.0 .. -0.5	34.82	1.53	8.88/-0.52	1.92/-2.57
-0.5 .. 0.0	102.78	2.53	6.20/-1.35	5.92/-4.61
0.0 .. 0.5	130.41	2.85	1.30/-3.17	6.64/-6.40
0.5 .. 1.0	128.73	2.84	2.41/-2.70	6.33/-5.47
1.0 .. 1.5	54.24	1.76	0.59/-1.95	2.89/-2.74
1.5 .. 2.0	13.96	0.95	0.28/-0.73	1.06/-1.01
2.0 .. 2.4	3.29	0.59	0.66/-0.34	0.33/-0.29

Table C.6: *Differential dijet cross section $d\sigma/d\eta_2^{jet}$ in the kinematic range 0.2 $< y <$ 0.85, $Q^2 <$ 1 GeV^2 and $x_\gamma^{OBS} >$ 0.75. Given in the table are the values for transverse energy of the leading jet between 17 and 25 GeV and an transverse energy for the second jet greater than 11 GeV in three different bins in the pseudo-rapidity of the leading jet.*

$d\sigma/d\eta_2^{Jet}$				
25 GeV $< E_T^{leading\ jet} <$ 35 GeV, $x_\gamma^{OBS} > 0.75$				
η_2^{Jet}	$d\sigma/d\eta_2^{Jet}$ pb	Δ_{stat} pb	Δ_{syst}(+/-) pb	$\Delta_{E-scale}$ (+/-) pb
$-1.0 < \eta_1^{jet} < 0.0$				
0.0 .. 0.5	0.98	0.22	0.17/-0.19	0.25/-0.11
0.5 .. 1.0	3.44	0.43	0.55/-0.19	0.74/-0.26
1.0 .. 1.5	6.19	0.55	0.45/-0.33	0.77/-0.50
1.5 .. 2.0	6.38	0.60	0.38/-0.91	0.59/-0.46
2.0 .. 2.4	3.74	0.57	0.36/-0.27	0.26/-0.27
$0.0 < \eta_1^{jet} < 1.0$				
-1.0 .. -0.5	0.09	0.06	0.11/-0.05	0.05/-0.01
-0.5 .. 0.0	4.38	0.48	0.38/-0.34	0.96/-0.35
0.0 .. 0.5	26.74	1.28	0.88/-1.97	2.64/-1.43
0.5 .. 1.0	35.24	1.50	1.52/-3.77	2.59/-1.77
1.0 .. 1.5	28.49	1.25	0.47/-0.81	1.90/-1.77
1.5 .. 2.0	21.66	1.14	1.25/-0.62	1.67/-1.29
2.0 .. 2.4	17.33	1.27	0.46/-0.93	1.19/-0.84
$1.0 < \eta_1^{jet} < 2.4$				
-1.0 .. -0.5	1.02	0.23	0.24/-0.32	0.37/-0.14
-0.5 .. 0.0	14.14	0.88	1.06/-0.83	1.35/-1.04
0.0 .. 0.5	30.44	1.33	1.26/-0.42	2.13/-1.82
0.5 .. 1.0	32.89	1.40	1.20/-1.51	2.35/-1.94
1.0 .. 1.5	27.11	1.21	0.66/-0.36	1.48/-1.50
1.5 .. 2.0	15.27	0.95	0.58/-0.65	0.77/-0.82
2.0 .. 2.4	6.47	0.81	0.37/-0.46	0.26/-0.34

Table C.7: *Differential dijet cross section $d\sigma/d\eta_2^{jet}$ in the kinematic range 0.2 $< y <$ 0.85, $Q^2 <$ 1 GeV^2 and $x_\gamma^{OBS} >$ 0.75. Given in the table are the values for transverse energy of the leading jet between 25 and 35 GeV and an transverse energy for the second jet greater than 11 GeV in three different bins in the pseudo-rapidity of the leading jet.*

$d\sigma/d\eta_2^{Jet}$				
35 GeV $< E_T^{leading\ jet} <$ 90 GeV, $x_\gamma^{OBS} > 0.75$				
η_2^{Jet}	$d\sigma/d\eta_2^{Jet}$ pb	Δ_{stat} pb	Δ_{syst}(+/-) pb	$\Delta_{E-scale}$ (+/-) pb
$-1.0 < \eta_1^{jet} < 0.0$				
0.5 .. 1.0	0.08	0.09	0.02/-0.05	0.02/-0.01
1.0 .. 1.5	0.22	0.09	0.19/-0.06	0.05/-0.03
1.5 .. 2.0	0.17	0.09	0.03/-0.07	0.02/-0.02
2.0 .. 2.4	0.08	0.08	0.22/-0.03	0.01/-0.01
$0.0 < \eta_1^{jet} < 1.0$				
0.0 .. 0.5	1.59	0.31	0.25/-0.17	0.17/-0.20
0.5 .. 1.0	5.36	0.58	0.45/-0.36	0.42/-0.34
1.0 .. 1.5	7.90	0.70	0.21/-0.45	0.47/-0.48
1.5 .. 2.0	5.63	0.59	0.36/-0.24	0.41/-0.33
2.0 .. 2.4	3.94	0.59	0.56/-0.38	0.25/-0.23
$1.0 < \eta_1^{jet} < 2.4$				
-1.0 .. -0.5	0.05	0.06	0.03/-0.03	0.03/-0.01
-0.5 .. 0.0	0.46	0.15	0.16/-0.07	0.05/-0.06
0.0 .. 0.5	5.90	0.60	0.58/-0.27	0.43/-0.36
0.5 .. 1.0	10.72	0.83	0.34/-0.63	0.70/-0.64
1.0 .. 1.5	11.11	0.82	0.61/-0.60	0.77/-0.71
1.5 .. 2.0	7.09	0.67	0.55/-0.24	0.46/-0.45
2.0 .. 2.4	3.46	0.58	0.45/-0.24	0.19/-0.17

Table C.8: *Differential dijet cross section $d\sigma/d\eta_2^{jet}$ in the kinematic range $0.2 < y < 0.85$, $Q^2 < 1$ GeV^2 and $x_\gamma^{OBS} > 0.75$. Given in the table are the values for transverse energy of the leading jet between 35 and 90 GeV and an transverse energy for the second jet greater than 11 GeV in three different bins in the pseudo-rapidity of the leading jet.*

$d\sigma/d\lvert\cos\theta^*\rvert$				
$\lvert\cos\theta^*\rvert$	$d\sigma/d\lvert\cos\theta^*\rvert$ pb	Δ_{stat} pb	Δ_{syst}(+/-) pb	$\Delta_{E-scale}$ (+/-) pb
$0.0 < x_\gamma^{OBS} < 0.6$				
0.0 .. 0.1	22.76	2.86	0.63/-2.46	0.89/-0.83
0.1 .. 0.2	16.23	2.28	0.49/-2.24	0.68/-0.43
0.2 .. 0.3	25.79	3.02	0.16/-2.21	0.55/-0.91
0.3 .. 0.4	27.74	3.05	0.39/-1.68	0.97/-1.05
0.4 .. 0.5	39.32	3.72	1.14/-0.46	1.59/-1.20
0.5 .. 0.6	60.28	4.78	1.68/-1.47	1.07/-2.13
0.6 .. 0.7	104.15	6.88	2.15/-5.31	4.23/-3.32
0.7 .. 0.8	208.38	10.84	3.48/-9.69	6.00/-5.77
$0.6 < x_\gamma^{OBS} < 0.75$				
0.0 .. 0.1	21.41	2.60	1.01/-0.49	0.33/-0.57
0.1 .. 0.2	26.15	2.97	0.54/-2.54	0.65/-0.29
0.2 .. 0.3	24.85	2.81	2.28/-1.38	1.94/-0.38
0.3 .. 0.4	28.42	3.01	0.42/-1.91	0.46/-0.54
0.4 .. 0.5	47.70	4.06	0.25/-4.53	0.47/-1.06
0.5 .. 0.6	57.38	4.41	0.67/-1.18	1.10/-1.19
0.6 .. 0.7	109.46	6.44	2.29/-1.97	2.97/-2.40
0.7 .. 0.8	204.98	9.66	10.09/-6.27	2.99/-5.00

Table C.9: *Differential dijet cross section $d\sigma/d\lvert\cos\theta^*\rvert$ in the kinematic range $0.2 < y < 0.85$, $Q^2 < 1$ GeV^2. The transverse energy of the two leading jets have to be greater than 14 GeV and 11 GeV, respectively. The values are shown for four different bins in x_γ^{OBS}.*

$\mid\cos\theta^*\mid$	$d\sigma/d\mid\cos\theta^*\mid$ pb	Δ_{stat} pb	Δ_{syst}(+/-) pb	$\Delta_{E-scale}$ (+/-) pb
$0.75 < x_\gamma^{OBS} < 0.85$				
0.0 .. 0.1	18.77	2.33	0.68/-1.95	0.27/-0.23
0.1 .. 0.2	27.34	2.95	0.70/-3.34	0.41/-0.17
0.2 .. 0.3	28.06	2.98	1.13/-1.84	0.34/-0.40
0.3 .. 0.4	37.18	3.39	0.93/-1.07	0.54/-0.93
0.4 .. 0.5	48.61	3.91	0.72/-4.05	0.46/-0.75
0.5 .. 0.6	69.07	4.72	1.69/-3.42	0.92/-0.87
0.6 .. 0.7	121.32	6.55	0.30/-3.40	1.88/-1.66
0.7 .. 0.8	214.22	9.29	14.99/-2.87	2.49/-1.97
$0.85 < x_\gamma^{OBS} < 1.0$				
0.0 .. 0.1	120.90	6.97	1.84/-5.91	1.35/-1.25
0.1 .. 0.2	111.75	6.69	2.87/-6.87	1.26/-0.98
0.2 .. 0.3	123.10	6.93	3.34/-7.88	1.33/-1.28
0.3 .. 0.4	139.85	7.33	1.06/-6.56	1.30/-1.25
0.4 .. 0.5	177.75	8.29	1.60/-5.05	1.88/-1.26
0.5 .. 0.6	204.31	8.84	2.27/-7.05	2.06/-1.74
0.6 .. 0.7	298.04	10.91	7.15/-5.10	3.34/-2.36
0.7 .. 0.8	424.66	13.87	9.81/-8.03	2.21/-3.48

Table C.10: *Continued: Differential dijet cross section $d\sigma/d|\cos\theta^*|$ in the kinematic range $0.2 < y < 0.85$, $Q^2 < 1$ GeV^2.*

$E_T^{leading\ jet}$ GeV	$d\sigma/dE_T^{leading\ jet}$ pb/GeV	Δ_{stat} pb/GeV	Δ_{syst}(+/-) pb/GeV	$\Delta_{E-scale}$ (+/-) pb/GeV
$-1 < \eta_1^{jet} < 0$, $-1 < \eta_2^{jet} < 0$				
14.0 .. 17.0	0.51	0.08	0.06/-0.05	0.03/-0.04
17.0 .. 21.0	0.057	0.018	0.013/-0.008	0.005/-0.005
$0 < \eta_1^{jet} < 1$, $-1 < \eta_2^{jet} < 0$				
14.0 .. 17.0	8.63	0.31	0.83/-0.44	0.39/-0.33
17.0 .. 21.0	2.26	0.13	0.23/-0.33	0.11/-0.15
21.0 .. 25.0	0.29	0.04	0.04/-0.08	0.02/-0.02
25.0 .. 29.0	0.037	0.015	0.006/-0.008	0.008/-0.003
29.0 .. 35.0	0.0087	0.0051	0.0014/-0.0036	0.0020/-0.0012
$1 < \eta_1^{jet} < 2.4$, $-1 < \eta_2^{jet} < 0$				
14.0 .. 17.0	36.41	0.64	1.71/-4.37	1.51/-1.62
17.0 .. 21.0	14.50	0.33	0.63/-1.17	0.84/-0.79
21.0 .. 25.0	5.12	0.20	0.33/-0.61	0.29/-0.27
25.0 .. 29.0	1.22	0.93	0.17/-0.13	0.09/-0.06
29.0 .. 35.0	0.32	0.04	0.06/-0.04	0.03/-0.02
35.0 .. 41.0	0.030	0.012	0.010/-0.003	0.003/-0.002
41.0 .. 48.0	0.008	0.006	0.002/-0.001	0.001/-0.001

Table C.11: *Differential dijet cross section $d\sigma/dE_T^{leading\ jet}$ in the kinematic range $0.2 < y < 0.85$, $Q^2 < 1$ GeV^2 and $x_\gamma^{OBS} < 0.75$. The transverse energy of the two leading jets have to be greater than 14 GeV and 11 GeV, respectively. The values are shown for different ranges of pseudo-rapidity for the leading and second jet.*

$d\sigma/dE_T^{leading\ jet}$ for $x_\gamma^{OBS} < 0.75$				
$E_T^{leading\ jet}$ GeV	$d\sigma/dE_T^{leading\ jet}$ pb/GeV	Δ_{stat} pb/GeV	Δ_{syst}(+/-) pb/GeV	$\Delta_{E-scale}$ (+/-) pb/GeV
$0 < \eta_1^{jet} < 1$, $0 < \eta_2^{jet} < 1$				
14.0 .. 17.0	19.72	0.47	1.38/-1.22	0.97/-0.83
17.0 .. 21.0	6.24	0.21	0.85/-0.51	0.36/-0.34
21.0 .. 25.0	1.64	0.10	0.18/-0.05	0.10/-0.10
25.0 .. 29.0	0.41	0.05	0.03/-0.13	0.04/-0.03
29.0 .. 35.0	0.061	0.015	0.010/-0.013	0.011/-0.006
35.0 .. 41.0	0.0075	0.0054	0.0021/-0.0014	0.0019/-0.0010
41.0 .. 48.0	0.0047	0.0049	0.0009/-0.0011	0.0007/-0.0011
$1 < \eta_1^{jet} < 2.4$, $0 < \eta_2^{jet} < 1$				
14.0 .. 17.0	64.13	0.86	3.42/-4.10	3.37/-3.14
17.0 .. 21.0	28.66	0.45	0.92/-1.10	1.63/-1.55
21.0 .. 25.0	11.12	0.28	0.19/-0.51	0.62/-0.64
25.0 .. 29.0	3.87	0.16	0.31/-0.18	0.33/-0.25
29.0 .. 35.0	1.38	0.08	0.03/-0.09	0.11/-0.09
35.0 .. 41.0	0.38	0.04	0.03/-0.03	0.03/-0.02
41.0 .. 48.0	0.080	0.019	0.013/-0.006	0.006/-0.005
48.0 .. 55.0	0.023	0.010	0.002/-0.006	0.002/-0.002
$1 < \eta_1^{jet} < 2.4$, $1 < \eta_2^{jet} < 2.4$				
14.0 .. 17.0	79.24	1.01	5.23/-3.92	4.01/-4.22
17.0 .. 21.0	39.42	0.53	3.36/-1.68	2.34/-2.15
21.0 .. 25.0	16.08	0.33	1.56/-0.53	1.11/-0.89
25.0 .. 29.0	6.95	0.21	0.24/-0.23	0.43/-0.47
29.0 .. 35.0	2.59	0.10	0.20/-0.04	0.18/-0.16
35.0 .. 41.0	1.11	0.07	0.04/-0.06	0.07/-0.07
41.0 .. 48.0	0.36	0.04	0.02/-0.07	0.03/-0.03
48.0 .. 55.0	0.13	0.02	0.02/-0.01	0.01/-0.01
55.0 .. 65.0	0.050	0.013	0.006/-0.013	0.004/-0.005

Table C.12: *Continued: Differential dijet cross section $d\sigma/dE_T^{leading\ jet}$ in the kinematic range $0.2 < y < 0.85$, $Q^2 < 1$ GeV^2 and $x_\gamma^{OBS} < 0.75$.*

$d\sigma/dE_T^{leading\ jet}$ for $x_\gamma^{OBS} > 0.75$				
$E_T^{leading\ jet}$ GeV	$d\sigma/dE_T^{leading\ jet}$ pb/GeV	Δ_{stat} pb/GeV	Δ_{syst}(+/-) pb/GeV	$\Delta_{E-scale}$ (+/-) pb/GeV
$-1 < \eta_1^{jet} < 0$, $-1 < \eta_2^{jet} < 0$				
14.0 .. 17.0	11.19	0.39	0.37/-0.22	0.78/-0.97
17.0 .. 21.0	1.60	0.11	0.25/-0.04	0.14/-0.14
$0 < \eta_1^{jet} < 1$, $-1 < \eta_2^{jet} < 0$				
14.0 .. 17.0	34.98	0.71	0.88/-0.94	1.53/-1.46
17.0 .. 21.0	12.30	0.32	0.19/-0.30	0.62/-0.74
25.0 .. 29.0	3.17	0.16	0.08/-0.05	0.20/-0.23
29.0 .. 35.0	0.54	0.06	0.04/-0.06	0.11/-0.04
35.0 .. 41.0	0.022	0.008	0.008/-0.003	0.007/-0.003
$1 < \eta_1^{jet} < 2.4$, $-1 < \eta_2^{jet} < 0$				
14.0 .. 17.0	52.81	0.84	0.87/-6.23	2.21/-2.21
17.0 .. 21.0	24.62	0.46	0.61/-1.19	1.38/-1.16
21.0 .. 25.0	10.93	0.31	0.11/-0.72	0.62/-0.51
25.0 .. 29.0	4.99	0.20	0.41/-0.42	0.40/-0.24
29.0 .. 35.0	1.84	0.10	0.05/-0.23	0.17/-0.10
35.0 .. 41.0	0.47	0.05	0.04/-0.05	0.04/-0.03
41.0 .. 48.0	0.092	0.020	0.029/-0.015	0.008/-0.009

Table C.13: *Differential dijet cross section $d\sigma/dE_T^{leading\ jet}$ in the kinematic range $0.2 < y < 0.85$, $Q^2 < 1$ GeV^2 and $x_\gamma^{OBS} > 0.75$. The transverse energy of the two leading jets have to be greater than 14 GeV and 11 GeV, respectively. The values are shown for different ranges of pseudo-rapidity for the leading and second jet.*

$d\sigma/dE_T^{leading\ jet}$ for $x_\gamma^{OBS} > 0.75$				
$E_T^{leading\ jet}$ GeV	$d\sigma/dE_T^{leading\ jet}$ pb/GeV	Δ_{stat} pb/GeV	Δ_{syst}(+/-) pb/GeV	$\Delta_{E-scale}$ (+/-) pb/GeV
$0 < \eta_1^{jet} < 1,\ 0 < \eta_2^{jet} < 1$				
14.0 .. 17.0	28.91	0.63	1.81/-1.14	1.19/-1.11
17.0 .. 21.0	12.43	0.32	1.42/-0.07	0.71/-0.56
21.0 .. 25.0	4.78	0.20	0.40/-0.16	0.28/-0.24
25.0 .. 29.0	1.45	0.10	0.10/-0.08	0.12/-0.10
29.0 .. 35.0	0.32	0.04	0.02/-0.04	0.05/-0.03
35.0 .. 41.0	0.034	0.012	0.010/-0.003	0.005/-0.005
41.0 .. 48.0	0.0087	0.0067	0.0029/-0.0031	0.0010/-0.0025
$1 < \eta_1^{jet} < 2.4,\ 0 < \eta_2^{jet} < 1$				
14.0 .. 17.0	39.50	0.72	0.38/-2.69	1.73/-1.69
17.0 .. 21.0	22.23	0.42	0.43/-0.61	1.13/-0.97
21.0 .. 25.0	10.17	0.29	0.09/-0.08	0.49/-0.51
25.0 .. 29.0	4.78	0.19	0.17/-0.10	0.36/-0.27
29.0 .. 35.0	2.09	0.10	0.08/-0.09	0.14/-0.13
35.0 .. 41.0	0.82	0.07	0.05/-0.03	0.05/-0.05
41.0 .. 48.0	0.31	0.04	0.01/-0.03	0.02/-0.02
48.0 .. 55.0	0.11	0.02	0.01/-0.02	0.01/-0.01
$1 < \eta_1^{jet} < 2.4,\ 1 < \eta_2^{jet} < 2.4$				
14.0 .. 17.0	1.79	0.16	0.08/-0.32	0.20/-0.21
17.0 .. 21.0	4.07	0.18	0.07/-0.45	0.26/-0.25
21.0 .. 25.0	4.75	0.19	0.24/-0.12	0.31/-0.23
25.0 .. 29.0	3.28	0.15	0.24/-0.07	0.15/-0.19
29.0 .. 35.0	1.77	0.09	0.06/-0.14	0.11/-0.09
35.0 .. 41.0	0.92	0.07	0.05/-0.04	0.05/-0.05
41.0 .. 48.0	0.40	0.04	0.04/-0.06	0.03/-0.02
48.0 .. 55.0	0.20	0.03	0.05/-0.02	0.02/-0.02
55.0 .. 65.0	0.034	0.011	0.015/0.005	0.002/-0.003

Table C.14: *Continued: Differential dijet cross section $d\sigma/dE_T^{leading\ jet}$ in the kinematic range $0.2 < y < 0.85$, $Q^2 < 1$ GeV^2 and $x_\gamma^{OBS} > 0.75$.*

$d\sigma/dx_\gamma^{OBS}$				
x_γ^{OBS}	$d\sigma/dx_\gamma^{OBS}$ pb	Δ_{stat} pb	Δ_{syst}(+/-) pb	$\Delta_{E-scale}$ (+/-) pb
14 GeV $< E_T^{leading\ jet} <$ 17 GeV				
0.0 .. 0.1	37.24	5.41	4.42/-3.94	4.79/-3.48
0.1 .. 0.2	409.34	14.01	32.42/-20.02	32.38/-27.75
0.2 .. 0.3	609.96	16.32	41.72/-9.64	37.09/-40.62
0.3 .. 0.4	623.35	15.51	11.59/-21.94	33.54/-25.12
0.4 .. 0.5	634.57	15.32	15.61/-9.14	31.16/-30.90
0.5 .. 0.6	688.34	15.93	13.42/-10.12	37.93/-29.05
0.6 .. 0.7	748.23	16.29	6.06/-11.60	41.08/-35.91
0.7 .. 0.8	994.93	19.14	23.68/-70.84	33.93/-46.66
0.8 .. 1.0	1769.79	18.98	27.08/-57.52	79.29/-72.74
17 GeV $< E_T^{leading\ jet} <$ 25 GeV				
0.0 .. 0.1	12.73	3.13	1.14/-2.46	1.10/-2.15
0.1 .. 0.2	227.16	9.13	31.37/-5.79	14.18/-11.72
0.2 .. 0.3	397.78	10.76	41.37/-8.99	30.99/-25.82
0.3 .. 0.4	525.50	12.40	7.94/-11.04	33.53/-35.10
0.4 .. 0.5	543.92	12.27	2.07/-15.61	35.30/-33.67
0.5 .. 0.6	566.69	12.25	16.60/-5.61	29.98/-33.15
0.6 .. 0.7	645.28	13.29	12.97/-9.49	34.33/-36.78
0.7 .. 0.8	812.95	14.64	13.01/-16.42	52.35/-46.91
0.8 .. 1.0	1540.46	15.65	24.65/-14.79	79.18/-72.86

Table C.15: *Differential dijet cross section $d\sigma/dx_\gamma^{OBS}$ in the kinematic range $0.2 < y < 0.85$, $Q^2 < 1$ GeV^2. The transverse energy of the two leading jets have to be greater than 14 GeV and 11 GeV, respectively. The pseudo-rapidity of the two leading jets have to be in the range $-1 < \eta_{1,2}^{jet} < 2.4$. The values are shown for different ranges of transverse energy of the leading jet.*

$d\sigma/dx_\gamma^{OBS}$				
x_γ^{OBS}	$d\sigma/dx_\gamma^{OBS}$ pb	Δ_{stat} pb	Δ_{syst}(+/-) pb	$\Delta_{E-scale}$ (+/-) pb
25 GeV $< E_T^{leading\ jet} <$ 35 GeV				
0.1 .. 0.2	13.53	1.98	3.64/-1.68	1.17/-1.62
0.2 .. 0.3	42.40	3.20	2.61/-0.68	3.27/-2.89
0.3 .. 0.4	60.25	3.76	4.61/-1.28	4.04/-4.74
0.4 .. 0.5	76.22	4.24	2.38/-6.05	7.21/-4.50
0.5 .. 0.6	101.90	4.96	0.91/-5.36	7.32/-7.49
0.6 .. 0.7	100.45	4.81	2.99/-1.71	7.65/-6.16
0.7 .. 0.8	135.84	5.53	5.24/-1.83	9.70/-7.39
0.8 .. 1.0	304.30	6.75	4.56/-7.82	20.08/-17.13
35 GeV $< E_T^{leading\ jet} <$ 90 GeV				
0.2 .. 0.3	3.75	1.03	0.99/-0.81	0.41/-0.40
0.3 .. 0.4	7.26	1.33	0.64/-1.17	0.88/-0.55
0.4 .. 0.5	11.91	1.66	1.26/-1.04	0.84/-0.74
0.5 .. 0.6	13.14	1.79	0.80/-0.75	1.19/-0.98
0.6 .. 0.7	20.36	2.23	0.71/-0.98	1.63/-1.29
0.7 .. 0.8	26.55	2.48	2.18/-1.09	1.54/-1.59
0.8 .. 1.0	72.75	3.44	2.77/-2.94	4.77/-4.41

Table C.16: *Continued: Differential dijet cross section $d\sigma/dx_\gamma^{OBS}$ in the kinematic range $0.2 < y < 0.85$, $Q^2 < 1$ GeV^2.*

Glossary

AFG .... Aurenche, Fontannaz and Guillet, a photon density parametrisation named after their authors

ARIADNE .... A Monte Carlo simulation program for simulation of QCD cascades implementing the color dipole model

BCAL .... Barrel Calorimeter

C5 .... Collimator 5 Veto Counter

CTD .... Central Tracking Detector

CTEQ .... Coordinated Theoretical-Experimental Project on QCD

DGLAP .... Dokshitzer-Gribov-Lipatov-Altarelli-Parisi

DIS .... Deep Inelastic Scattering

EMC .... Electromagnetic Calorimeter

FCAL .... Forward Calorimeter

FLT .... First Level Trigger

GRV .... Glück, Reya and Vogt, a photon density parametrisation named after their authors

GS .... Gordon and Storrow, a photon density parametrisation named after their authors

HAC .... Hadronic Calorimeter

HERA .... Hadron Electron Ring Accelerator

HERWIG .... A Monte Carlo package for simulating Hadron Emission Reactions With Interfering Gluons

LEP .... Large Electron-Positron collider

LO .... Leading Order, first term in a series expansion for the calculation of a cross section

MC .... Monte Carlo

NC-DIS .... Neutral Current Deep Inelastic Scattering

NLO .... Next-Leading-Order, second term in a series expansion

PETRA .... Positronen-Elektronen Tandem Ring Anlage

PMT .... Photomultiplier Tube

PYTHIA .... A program for the generation of high-energy physics events, i.e. for the description of collisions at high energies between elementary particles

QCD .... Quantum Chromodynamics

QED .... Quantum Electrodynamics

RCAL .... Rear Calorimeter

SLAC .... Stanford Linear Accelerator

SLT .... Second Level Trigger

SRTD .... Small Angle Rear Tracking Detector

TLT .... Third Level Trigger

UNO .... Uranium Noise, steady signal from the radioactivity of the calorimeter cells

VDM .... Vector Meson Dominance Model

ZUFO .... Zeus Unidentified Flow Objects, reconstructed detector objects using tracking and calorimeter information

Bibliography

[1] J. Frank and G. Hertz, *Verh. Deutschen Phys. Ges.*, **16** 457 (1914)

[2] R. Hofstadter and R.W. McAllister, Phys. Rev., **102** 851 (1956)

[3] M. Gell-Mann, *Phys. Lett.***8**, 214 (1964)

[4] G. Zweig, CERN-TH 401 and CERN-TH 412 (1964)

[5] V.E. Barnes *et al.*, *Phys. Rev. Lett.* **12**, 204 (1964)

[6] H. Fritzsch,M. Gell-Mann and H. Leutwyler, *Phys. Lett.* B **47**, 365 (1973)

[7] R. Brandelik *et al.* Evidence for a spin one gluon in three jet events, *Phys. Lett.* B **97**, 453 (1980)

[8] R.P. Feynman, *Phys. Lett.* **23**,1415 (1969)

[9] J.D. Bjorken, *Phys. Rev.* **179**, 1547 (1969)

[10] G. Miller *et al.*, *Phys. Rev.* D **5**, 528 (1972)

[11] Particle Data Group, $http://pdg.lbl.gov/2000/hadronicrpp_page3.ps$

[12] G. Altarelli, G. Parisi, *Nucl. Phys.* B **126**, 298 (1977)

[13] ZEUS Collaboration, J.Breitweg et al. Measurement of the Proton Structure Function F_2 and $\sigma_{tot}^{\gamma^* p}$ at Low Q^2 and Very Low x at HERA, *Phys. Lett.* B **407**, 432 (1997)

[14] ZEUS Collaboration, M.Derrick et al. Measurement of the Proton Structure Function F_2 at low x and low Q^2 at HERA, *Z. Phys.* C **69**, 607 (1995)

[15] W-K. Tung et al. hep-ph 9609399

[16] R.G. Roberts et al. hep-ph 9696345

[17] J.J. Sakurai, *Phys. Rev. Lett* **22**, 981 (1969)

[18] J.J. Sakurai, D. Schildknecht, *Phys. Lett* B **40**, 121 (1972)

[19] E. Witten, *Nucl. Phys.* B **120**, 189 (1977)

[20] R. Nisius, *Phys. Rept.* **332**, 165 (2000)

[21] M. Krawczyk, Structure Functions for the Virtual and Real Photons, Photon 2000, Proceedings, Ambleside 2000

[22] OPAL Collaboration, G. Abbiendi *et al.*, Total Hadronic Cross-Section of Photon-Photon Interactions at LEP *Eur. Phys. J.* C **14**, 199 (2000)

[23] OPAL Collaboration, G. Abbiendi *et al.*, Di-Jet Production in Photon-Photon Collisions at $\sqrt{s}_{ee}$=161 and 172 GeV, *Eur. Phys. J.* C **10**, 547 (1999)

[24] H1 Collaboration, T. Ahmed *et al.*, Hard Scattering in gamma-p interactions, *Phys. Lett.* B **297**, 205 (1992)

[25] ZEUS Collaboration, M. Derrick *et al.*, Observation of Hard Scattering in Photoproduction at HERA, *Phys. Lett.* B **297**, 404 (1992)

[26] H1 Collaboration, I. Abt *et al.*, Measurement of Inclusive Jet Cross Sections in Photoproduction at HERA, *Phys. Lett.* B **314**, 436 (1993)

[27] ZEUS Collaboration, M.Derrick *et al.*, Observation of Direct Processes in Photoproduction at HERA, *Phys. Lett.* B **322**, 287 (1994)

[28] ZEUS Collaboration, M.Derrick *et al.*, Inclusive Jet Differential Cross Sections in Photoproduction at HERA, *Phys. Lett.* B **342**, 417 (1995)

[29] ZEUS Collaboration, M.Derrick *et al.*, Dijet Cross Sections in Photoproduction at HERA, *Phys. Lett.* B **348**, 665 (1995)

[30] ZEUS Collaboration, J.Breitweg *et al.*, Measurement of inclusive D*+- and associated dijet cross sections in photoproduction at HERA, *Eur. Phys. J.* C **6**, 67 (1999)

[31] M. Glück, E. Reya, and A. Vogt, Parton structure of the photon beyond the leading order, *Phys. Rev.* D **45**, 3986 (1992)

[32] M. Glück, E. Reya, and A. Vogt, Photonic partons distributions, *Phys. Rev.* D **46**, 1973 (1992)

[33] M. Glück, E. Reya, and A. Vogt, Pionic parton distributions, *Z. Phys.* C **53**, 651 (1992)

[34] C. Berger and W. Wagner, Photon photon reactions, *Phys. Rep* **146**, 1 (1987)

[35] JADE Collaboration, W. Bartel *et al.*, Experimental study of the photon structure function F_2 at Q^2 from 10 GeV^2 to 222 GeV^2, *Z. Phys.* C **24**, 231 (1984)

[36] PLUTO Collaboration, C. Berger *et al.*, Measurement of the photon structure function $F_2^\gamma\,(x, Q^2)$, Phys. Lett. B **142**, 111 (1984)

[37] PLUTO Collaboration, C. Berger *et al.*, Measurement and QCD analysis of the photon structure function $F_2^\gamma\,(x, Q^2)$, Nucl. Phys. B **281**, 365 (1987)

[38] PLUTO Collaboration, C. Berger *et al.*, Measurement of the total photon-photon cross-section for the production of hadrons at small Q^2, *Phys. Lett.* B **149**, 421 (1984)

[39] PLUTO Collaboration, C. Berger *et al.*, A measurement of the Q^2 and W dependence of the $\gamma\gamma$ total cross section for hadron production, *Z. Phys.* C **26**, 353 (1984)

[40] TASSO Collaboration, M. Althoff *et al.*, Measurement of the photon structure function F_2 at Q^2 from 7 to 70 (GeV/c)^2, *Z. Phys.* C **31**, 527 (1986)

[41] TPC/2γ Collaboration, H.Aihara *et al*, Measurements of the photon structure function $F_2^\gamma\,(x, Q^2)$ in the region $0.2 < Q^2 < 7$ GeV^2, *Z. Phys.* C **34**, 1 (1987)

[42] AMY Collaboration, T. Sasaki *et al.*, A measurement of the photon structure function F_2, *Phys. Lett.* B **252**, 491(1990)

[43] TPC/2γ Collaboration, D. Bintinger *et al.*, Measurement of the total hadronic cross section in virtual photon-photon interactions, *Phys. Rev. Lett.* **54** 763 (1985)

[44] TPC/2γ Collaboration, H. Aihara *et al.*, Observation of scaling of the photon structure F_2 at low Q^2, *Phys. Rev. Lett.* **58**, 97 (1987)

[45] TPC/2γ Collaboration, H. Aihara *et al.*, Measurement of the photon structure function $F_2^\gamma\,(x, Q^2)$ in the region $0.2 < Q^2 7$ GeV^2, *Z. Phys.* C **34**, 1 (1987)

[46] L.E. Gordon and J.K. Storrow, The parton distribution of the photon and the structure function $F_\gamma^2\,(x, Q^2)$, *Z. Phys.* C **56** 307 (1992)

[47] L.E. Gordon and J.K. Storrow, New parton distributions functions for the photon, *Nucl. Phys.* B **489**, 405 (1997)

[48] AMY Collaboration, S.K. Sahu *et al.*, A high-Q^2 measurement of the photon structure function F_2, *Phys. Lett.* B **346**,208 (1995)

[49] JADE Collaboration, W. Bartel *et al.*, Experimental study of the photon structure function F_2 in the high Q^2 region, *Phys. Lett.*. B **121**, 203 (1983)

[50] AMY Collaboration, B.J. Kim *et al.*, Measurement of the inclusive jet cross-section in photon-photon interactions at TRISTAN, *Phys. Lett.* B **325**, 248 (1994)

[51] CELLO Collaboration, H.J. Behrend *et al.*, Experimental study of the hadronic photon structure function, *Phys. Lett.* B **126**, 391 (1983)

[52] OPAL Collaboration, R. Akers *et al.*, Measurement of the photon structure function F_2^γ in the reaction $e^+e^- \to e^+e^- +$ hadrons at LEP, *Z. Phys.* C **61**, 199 (1994)

[53] TOPAZ Collaboration, H. Hayashii *et al.*, Measurement of the inclusive cross section of jets in $\gamma\gamma$ interactions at TRISTAN, *Phys. Lett.* B **314**, 149 (1993)

[54] TOPAZ Collaboration, K. Muramatsu *et al.*, Measurement of the photon structure function F_2 and jet production at TRISTAN, *Phys. Lett.* B **322**, 477 (1994)

[55] Aurenche, Fontannaz and Guillet, Parton distribution in the photon, *Z. Phys.* C **64**, 621 (1994)

[56] R.K. Ellis, W.J. Stirling and B.R. Webber, *QCD and Collider Physics* Cambridge Monographs on Particle Physics, Nuclear Physics and Cosmology

[57] M. H. Seymour Jet phenomenology, hep-ph/9707349

[58] S. Catani, Yu.L. Dokshitzer, M.H. Seymour and B.R. Webber, Longitudinally invariant k_T clustering Algorithms for Hadron-Hadron collisions, *Nucl. Phys.* B 406,187 (1993)

[59] S.D. Ellis and D.E. Soper, Successive combination jet algorithm for hadron collisions, *Phys. Rev.* D **48**,3160 (1993)

[60] R. Donaldson (ed.) and J.N. Marx (ed.), Physics of the superconducting supercollider, Proceedings, Snowmass, USA, June 23 - July 11, 1986

[61] M. Klasen, T. Kleinwort and G. Kramer, Inclusive jet production in γp and $\gamma\gamma$ processes: direct and resolved photon cross-sections in next-to-leading order QCD, *Eur. Phys. J.* C **1**,1 (1998)

[62] M. Klasen and G. Kramer, Inclusive two jet production at HERA: direct and resolved cross-sections in next-to-leading order QCD, *Z. Phys.* C **76**, 67 (1997)

[63] B.W. Harris and J.F. Owens, Photoproduction of jets at HERA in next-to-leading order QCD, *Phys. Rev.* D **56**, 4007 (1997)

[64] S. Frixione, A general approach to jet cross-sections in QCD, *Nucl. Phys.* B **507**, 295 (1997)

[65] P. Aurenche, J.P. Guillet, L. Bourhis and M. Fontannaz, Dijet cross-section in photoproduction at HERA, Proceedings for Workshop on Future Physics at HERA, Hamburg, Germany, 30-31 May 1996, vol. 1 570.

[66] B.W. Harris, M. Klasen and J. Vossebeld, Detailed comparison of next-to-leading order predictions for jet photoproduction at HERA, Proceedings for Workshop of Monte Carlo Generators for HERA Physics, 1998/99 http://www.desy.de/ heramc/proceedings/wg20 hep-ph/9905348

[67] ZEUS Collaboration, J. Breitweg *et al.*, Dijet Cross Sections in Photoproduction at HERA, *Eur. Phys. J.* C **1**, 109 (1998)

[68] ZEUS Collaboration, J.Breitweg *et al.* High-ET Inclusive Jet Cross Sections in Photoproduction at HERA, *Eur. Phys. J.* C**4**, 591 (1998)

[69] ZEUS Collaboration, J.Breitweg *et al.* Measurement of Three-jet Distributions in Photoproduction at HERA, *Phys. Lett.* B **443**, 394 (1998)

[70] W.T. Giele, E.W.N. Glover and David A. Kosower, The two jet differential cross-section at $\mathcal{O}(\alpha_s^3)$ in hadron collisions, *Phys. Rev. Lett.* **73**, 2019 (1994)

[71] J.H. Vossebeld, Dijet Photoproduction at High Transverse Energies, Ph.D. Thesis, University of Amsterdam (1999)

[72] B.W. Harris and J.F. Owens, Jet photoproduction and the structure of the photon, *Phys. Rev.* D **57**, 5555 (1998)

[73] The ZEUS Detector, Status Report, DESY 1993

[74] B. Foster *et al.*, *Nucl. Inst. Meth.*, **A338**, 254 (1994)

[75] M.Derrick *et al.*, *Nucl. Inst. Meth.*, **A309**, 77 (1991)

[76] Particle Data Group 2000 and more

[77] A. Andresen *et al.*, *Nucl. Inst. Meth.*, **A309**, 101 (1991)
A. Bernstein *et al.*, *Nucl. Inst. Meth.*, **A336**, 23 (1993)

[78] H. Bethe and W. Heitler, *Proc. Roy. Soc.*, A **146**,83 (1934)

[79] L.Suszycki, Luminosity Monitoring, Proc. of the HERA Workshop (1987), Vol.2 , 505

[80] G.F. Hartner, VCTRAK Briefing: Program and Math ZEUS-Note 98-058

[81] R. Brunner, "GEANT 3.13", CERN DD/EE/84-1;
R. Brun *et al.*, "GEANT 3", CERN DD/EE/11-1 (1989).

[82] ZGANA, ZEUS trigger simulation library, Els de Wolf (editor) *et al.*

[83] HERWIG 5.9; G. Marchesini,B.R. Webber,G. Abbiendi, I. G. Knowles,M.H. Seymour,L. Stanco, Computer Phys. Commun. **67**, 465 (1992)

[84] PYTHIA 5.7; H.-U. Bengtsson, T. Sjöstrand, Computer Phys. Commun. **46**, 43 (1987)

[85] ARIADNE 4.08; L. Lonnblad, A Program for Simulation of QCD Cascades implementing the color dipole model, *Comput.Phys.Commun.* **71**, 15 (1992)

[86] G. Ingelman, A.Edin, J. Rathsman, LEPTO 6.5 - A Monte Carlo Generator for Deep Inelastic Lepton-Nucleon Scattering, DESY 96-057

[87] H. Spiesberger, HERACLES - An Event Generator for ep Interactions at HERA Including Radiative Processes, Version 4.6, unpublished program manual, (1993)

[88] T. Sjöstrand, Comput. phys. Commun. **39**,347 (1986)

[89] S. Frixione, M.L. Mangano, P. Nason and G. Ridolfi, *Phys. Lett.*B **319**, 339 (1993)

[90] C.F. von Weizsäcker, *Z. Phys* **88**, 612 (1934),
E.J. Williams, *Phys. Rev.* **45**, 729 (1934)

[91] G. Gustafson, *Phys. Lett.* B **175**, 453 (1986)

[92] G. Gustafson, U. Petterson, *Nucl. Phys.* B **306**, 746 (1988)

[93] B. Andersson *et. al*, *Z. Phys* C **43**, 625 (1989)

[94] B. Andersson, G. Gustafson, L. Lönnblad, *Nucl. Phys.* B **339**, 393 (1990)

[95] B. Andersson, G. Gustafson, G. Ingelman, T. Sjöstrand, Phys. Rep. **97**, 33 (1983)

[96] J.M. Butterworth and R.J.Taylor, "A Global Study of Photon-Induced Jet Production", Proceedings Photon 1999, Freiburg, Germany

[97] ZEUS Collaboration, J. Breitweg *et al.*, Measurement of Dijet Photoproduction at High Transverse Energies at HERA, *Eur. Phys. J.* C **11**, 35 (1999)

[98] G. Schuler and T. Sjöstrand, Low and high mass components of the photon distribution functions, *Z. Phys.* C **68**, 607 (1995)

[99] G. Schuler and T. Sjöstrand, Parton distributions of the virtual photon, (1996) *Phys.Lett.* B **376**, 193 (1996)

[100] M. Glück, E. Reya and A. Vogt, Dynamical parton distributions of the proton and small x physics, *Z. Phys.* C **67**,433 (1995)

[101] H.L. Lai, J. Botts, J. Huston,J.G. Morfin, J.F. Owen, J.W. Qiu, W.K. Tung, H. Weerts, Global QCD Analysis and the CTEQ Parton Distributions, (1995) *Phys.Rev.* D **51**, 4763 (1995)

[102] M. Glück, E. Reya and A. Vogt, Photonic parton distributions, *Phys.Rev.* D **46**, 1973 (1992)

[103] A. Blondel and F. Jacquet, DESY 79-48 (1979)

[104] A. Savin, Study of the Calorimeter Noise in 1996 data, ZEUS-Note 98-007

[105] G. M. Briskin, Diffractive Dissociation in *ep* Deep Inelastic Scattering, Ph.D. Thesis, Tel Aviv University (1998), DESY-Thesis-1998-036.

[106] G. Briskin, A. Caldwell, Comparison of CAL Energy for Electrons with CTD momentum, ZEUS-Note 95-035

[107] J.H.Vossebeld,S. Schlenstedt and F.Pelucchi, Study of the Calorimeter Energy Scale in the ZEUS Monte Carlo, ZEUS-Note 96-104

[108] A. Caldwell, W. Liu and B. Straub, BCAL Electron Studies, Part I, MC and Test Beam Energy Studies, ZEUS-Note 98-02

[109] A. Caldwell, W. Liu, B. Mellado and B. Straub, BCAL Electron Studies, Part II, Energy Scale Calibration, ZEUS-Note 98-018

[110] B. Straub, BCAL Energy Scale, Nonuniformity Corrections and Resolution, Presentation given at ZEUS weekly meeting, 1. June 1998

[111] A.F. Zarnecki, *CAL Energy Scale for Hadrons*, Presentation given at the ZEUS Collaboration Meeting, June 1998

[112] J.H. Vossebeld, Determination of Hadronic Energy Corrections from a Fit to NC-DIS Data, ZEUS-Note 99-002

[113] M. Wing, Precise measurement of jet energies with the ZEUS Detector, To be published in the proceedings of 9th Conference on Calorimetry in High Energy Physics (CALOR 2000), Annecy, France, 9-14 Oct 2000, based on work performed by the author of this thesis. hep-ex/0011046

[114] S. Bentvelsen, J. Engelen and P. Kooijman, HERA,Physics at HERA Vol.1, Proceedings, Hamburg 1991.

[115] CERN Application Software Group, 'MINUIT: Function Minimisation and Error Analysis', CERN Program Library Long Writeup D506

[116] ZEUS Collaboration, J.Breitweg *et al.*, Measurement of Jet Shapes in Photoproduction at HERA, *Eur. Phys. J.* C **2**, 61 (1998)

[117] ZEUS Collaboration, S. Chekanov *et al.*, Dijet Photoproduction at HERA and the structure of the photon, *Eur. Phys. J.* C **23**, 4, 615-631 (2002)

[118] OPAL Collaboration, G. Abbiendi *et al.*, Measurement of the Hadronic Photon Structure Function F_2^γ at LEP2, Submitted to *Phys. Lett.* B, hep-ex/0202035

[119] H1 Collaboration, C. Adloff *et al.*, Measurement of Dijet Cross Sections in Photoproduction at HERA *Eur. Phys. J.* C **25**, 1, 13-23 (2002)

[120] J.J. Whitmore, QCD and Proton and Photon Structure Since DIS2001, *Acta Physica Polonica* B **33**, 2727-2748, October 2002